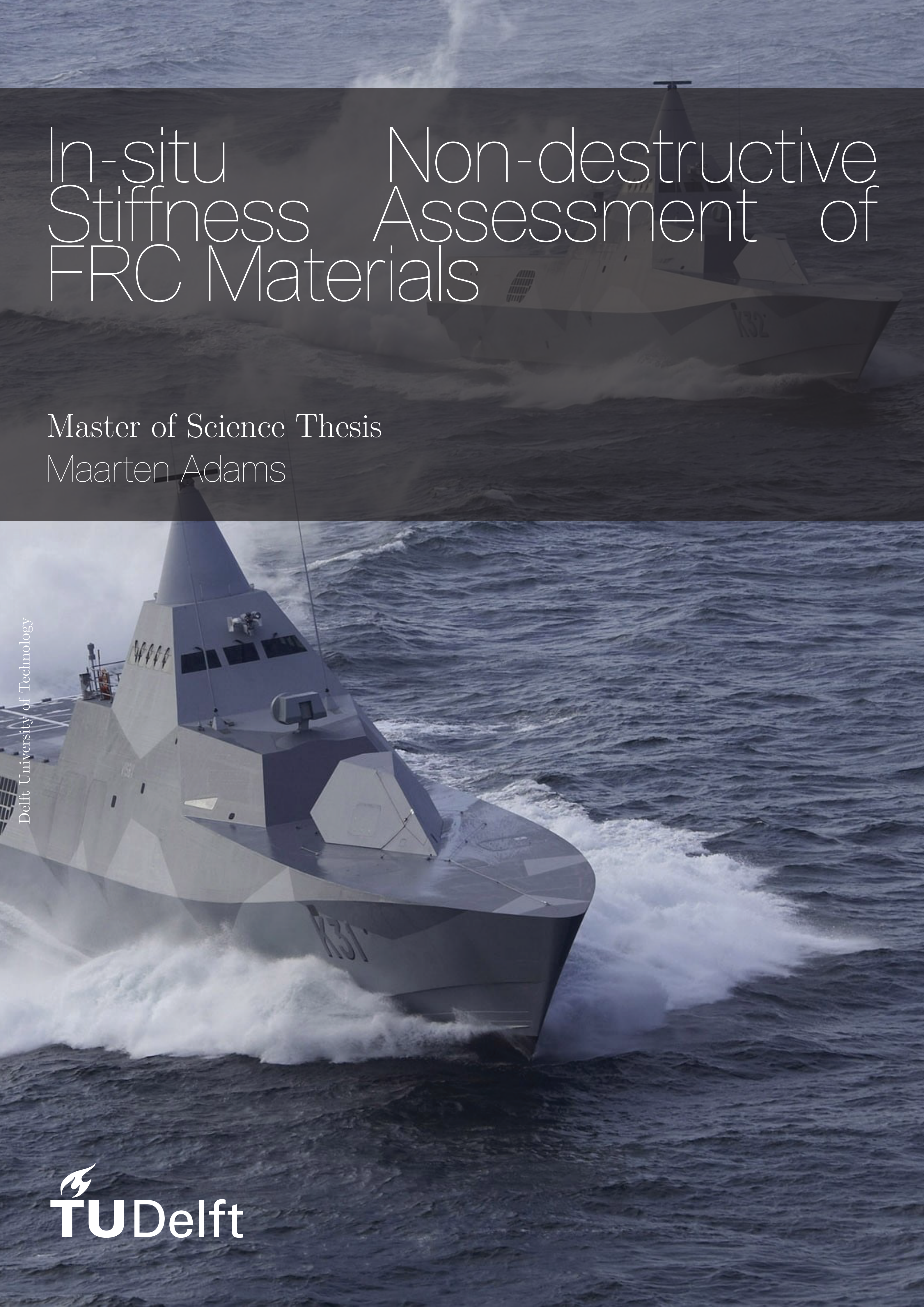

In-situ Non-destructive Stiffness Assessment of FRC Materials

Master of Science Thesis

Maarten Adams

Delft University of Technology

In-situ Non-destructive Stiffness Assessment of FRC Materials

by

M.G.A. (Maarten) Adams

to obtain the degree of Master of Science in Marine Technology
at Delft University of Technology,
to be defended publicly on Tuesday May 24, 2022 at 10:15 AM.

Document number:	MT.21/22.029.M	
Student number:	4469194	
Project duration:	May, 2021 - May, 2022	
Specialization:	Ship and Offshore Structures	
Thesis committee:	Dr. L. Pahlavan	TU Delft, supervisor, chair
	Prof. Dr. C. Kassapoglou	TU Delft, supervisor
	Ir. A.J. Huijer	TU Delft, daily supervisor
	Dr. C.L. Walters	TU Delft
	Ir. J.A.A. Vaders	DMO

The cover image shows two Visby class corvette vessels of the Royal Swedish Navy. These are the longest naval ships currently built from composite materials [1][2]

TU Delft

Abstract

Fiber Reinforced Composite (FRC) materials are gaining great popularity in marine structures because of their excellent strength-to-weight ratio, low density, and provided freedom in the design process. However, the use of FRC materials comes along with relatively large uncertainties in material properties and structural integrity after manufacturing and during its use. Therefore, reliable structural evaluation methods are highly desirable. As a result, research on structural evaluation methods, capable of an in-situ non-destructive stiffness assessment of various FRC materials has significant engineering importance.

In this research a new stiffness assessment methodology is proposed. This methodology is based on a coupling principle between the laminate structural stiffness properties and the ultrasonic guided wave characteristics of FRC materials. In the methodology, a range of possible stiffness properties is defined based on the structural information available for a plate of interest. The average relation between this range of interest and corresponding wave characteristics is described using a set of coupling coefficients which are determined using numerical simulations. For this, a batch of reference laminates is constructed that covers the entire range of interest. Input for the system are the group velocities of the zeroth-order symmetric and antisymmetric guided wave modes, measured on the plate of interest. The stiffness approximation is expected to converge when the possible stiffness range of the plate of interest is sufficiently described by the reference laminates included in the batch. The accuracy of the stiffness approximation is determined by (1) the inclusion of wave characteristics described in the system, (2) the accuracy of the coupling coefficients, and (3) the accuracy of the experimental data used as input to the system.

The potential of the proposed methodology and the effect of accuracy factors (1) and (2) are evaluated using a numerical feasibility study based on numerical simulations. In this study, three scenarios are considered that differ in the amount of structural information available on the plate of interest. It was concluded that the stiffness approximation converges to constant results when the number of reference laminates is sufficiently large. A maximum error of 4% is achieved when only the stiffness properties of the laminae are unknown and all other structural information is known. All extensional and the diagonal flexural stiffness components can be approximated within a 2% and 10% error, respectively, when only the stacking sequence is unknown. Off-diagonal flexural stiffness components are difficult to obtain for this situation. The diagonal extensional and diagonal flexural stiffness components can be approximated within a 3% error when both the stiffness properties of the laminae and the stacking sequence are unknown. The off-diagonal stiffness components cannot be approximated in this situation.

The in-situ application of the methodology and the effect of accuracy factor (3) have been tested in an experimental setup. For this, a sample plate was used for which the ply thickness, stacking sequence, and material density were assumed to be sufficiently known. Furthermore, the stiffness properties of the laminae were assumed to be known within a range of 80-120% compared to two references. The first reference was based on the properties provided by manufacturing. The second reference was based on previous research on the stiffness estimation of FRC materials. Good measurement and analysis times are achieved by using a compact measuring device that is capable of recording the wave signal in five directions simultaneously. The stiffness properties provided by the manufacturing were concluded to be unreliable. Compared to the properties estimated by previous research, differences in the range of 2-15% were obtained for the diagonal stiffness components. Differences in the range of 17-53% were obtained for the off-diagonal components. However, a reliable accuracy assessment of the in-situ application of the methodology is difficult to obtain since the exact stiffness properties of the material are unknown. Furthermore, it is concluded that, compared to the numerical feasibility study, the validity of the assumptions made comes with greater uncertainty for the in-situ application. Therefore, in the future, the range of stiffness properties included in the batch should be widened to better deal with deviations in material properties.

Preface

This thesis, ”In-situ Non-destructive Stiffness Assessment of FRC Materials”, is the result of my graduation project to obtain the master’s degree in Marine Technology with the specialization of Ship and Offshore Structures at the University of Technology Delft.

First of all, I would like to thank Pooria Pahlavan for the pleasant guidance throughout the project. I enjoyed our discussions and have been motivated throughout the project by your positive and supportive mindset.

Likewise, I would like to thank Arno Huijer for his daily supervision during my thesis. Thank you for your endless availability, critical view during discussions, and ever-present enthusiasm when I entered your office.

Another word of gratitude must be given to Christos Kassapoglou for his supervision. I have learned a lot from your critical feedback and questions during our meetings.

Furthermore, I would like to thank Carey Walters and André Vaders for being part of my graduation committee and for the support and feedback over the last months.

Lastly, I would like to thank my family, friends, fellow Froude board members, and roommates for their support, listening ear, and all non-academic distraction.

Maarten Adams
Rotterdam, May 2022

Contents

1

Introduction

1.1. Background and motivation

On 12 December 2015, the Paris Agreement was adopted by 196 parties at the Conference of the Parties (COP) 21. The goal of this agreement is to limit global warming to 2°, but preferably 1.5° Celsius, compared to pre-industrial levels [3]. In accordance with this agreement, the European Union (EU) established the European Green Deal, containing the goal of becoming the first climate neutral continent in the world in 2050 [4]. A first target of this agreement is to reduce greenhouse gas (GHG) emissions by 55% by 2030. The maritime sector can make a substantial contribution in achieving these goals. Globally, the GHG emission from the maritime sector is 940 million tons of CO_2 per year, which is approximately 2-3% of the global GHG emissions [5]. In 2015, the maritime sector represented 13% of the total EU GHG emissions of the transport sector [5]. These GHG emissions from maritime transport at EU level are expected to increase by 86% above pre-industrial levels by 2050 if the current trend continues. One of the reasons for this projected increase is the expected growth of the world economy and the associated demand for transport from world trade that comes with it [6]. The demand for more fuel-efficient vessels is therefore unquestionably one of the main challenges in today's maritime sector.

Multiple research fields can be distinguished that aim to reduce emissions in the marine sector. Examples of these fields include the transition to new fuels such as hydrogen and biofuels, wind-assisted propulsion, and increasing the fuel efficiency of marine vessels. In this last field, the weight of the vessels plays an important role. A reduction in overall structural weight is related to the payload carrying capacity and the hydrodynamic performance of a vessel. A reduction in structural weight allows for an increase in payload carrying capacity and therefore a reduction in fuel consumption per payload carrying capacity [7].

Fiber Reinforced Composite materials

For a long time, steel (since the 1880s) and aluminum (since the 1930s) have been the conventional materials used in shipbuilding. However, the use of fiber-reinforced composites is becoming a promising alternative considering their low density. For example, feasibility studies found that the structural weight of a marine patrol vessel made of glass reinforced plastic sandwich composite material should be ∼10% lighter than an aluminum vessel and ∼36% lighter than a steel vessel of similar size [1]. Other advantages of composites are good resistance to the marine environment [8], high strength-to-weight ratio [8], greater freedom in the design process [2][9], and specific advantages, such as good stealth characteristics [1][2].

Examples of the application of FRC material in marine structures are the 72-meter-long Visby Class Corvette vessels of the Swedish Navy, the 75-meter-long sailing yacht Mirabella V, and the 141-meter-long motor yacht Yas [10] see the cover page figure, figure 1.1a and figure 1.1b, respectively. The corvette vessels and Mirabella V are built using sandwich-structured composites, and the motor yacht Yas is rebuilt using glass and carbon fiber reinforced polymers. Another application of composites can be found in the production of propellers in, for example, the chemical tanker Taiko Maru [11], see figure 1.2. The use of lightweight composite propellers allows for larger blades, which increases the propulsive efficiency and consequently saves fuel.

(a) (b)

Figure 1.1: (a) 75-Meter sailing yacht Mirabella V constructed of aramid foam core / vinylester sandwich structures [12]. (b) 14-Meter motor yacht Yas rebuild using carbon fiber and glass fiber reinforced polymers [13].

(a) (b)

Figure 1.2: (a) The composite propeller installed on (b) the chemical tanker Taiko Mura [11].

The use of composite materials in commercial vessels is yet still limited due to class regulations, primarily based on fire resistance [1][14]. Furthermore, due to the early stage of composite use in marine applications, the knowledge of recyclability, repairability, and standardization of the production process is still in an initial stage [15][16]. FIBRESHIP and RAMSSES are two European consortia that aim to overcome these barriers [10]. They push for composites in shipbuilding through demonstration projects, including composite decks, rudders, hulls, modular cabins and superstructures, patch repairs to steel, and composite-to-steel welded joints. Additionally, new routes for certification (long- and short-term) and production methods, new joining technologies, and design tools are developed. However, this research will focus primarily on another disadvantage, namely the relatively large uncertainties in material properties and structural integrity of FRC materials after production and during their use [17][18].

An FRC structure is a mixture of two or more materials (constituents) that together provide the desired combination of material properties. The production of these structures can be done using several different techniques. In all of these techniques, the production process comes with some uncertainty; the exact material properties of the composite and the presence of possible irregularities in the final product are unknown. Process-induced defects, such as voids, fiber misalignment, and delamination are common problems encountered during composites manufacturing [19][20]. The formation of these irregularities can significantly affect the mechanical performance of the composite. Besides that, structural degradation can arise during service of the structure due to (cyclic) loading, the operating environment, or human errors. To fully exploit the advantages of FRC structures, it is important to have a high-quality knowledge of the properties of the produced structures [21].

Structural evaluation methods

The field of structural evaluation involves the analysis of structural properties and the identification and characterization of structural damage. Structural evaluation is concerned with techniques and measurements that provide data on the condition of materials and structures at the time of manufacturing and in-service [22]. The remaining lifetime prediction and maximization is strongly related to structural evaluation. Through structural evaluation techniques, high-quality products and a better prediction of the structural life expectancy can be guaranteed. In addition to that, schedule-based structural evaluation or continuous structural evaluation (structural health monitoring) can replace schedule-based maintenance with condition-based maintenance, saving the costs of unnecessary maintenance and preventing unscheduled maintenance that will affect the operability of a vessel [23].

Multiple structural evaluation techniques can be distinguished. In general, most of these techniques employ mechanical, chemical, or electromagnetic energies to introduce a disturbance into the structure and measure the response. Based on the assumption that an internal anomaly will affect a change in the returned signal, the returned signal provides information about the material properties or structural damages. Each of the techniques is specialized in or limited to specific aspects within the field of structural evaluation. Several techniques can determine the existence, location, type, and severity of damage. Others are limited to (combinations of) one of these characteristics. Next to that, a couple of techniques can accurately estimate the material stiffness. In general, the techniques can be distinguished as destructive or non-destructive and as being limited to (large) test setups or capable of being executed in-situ [2][24].

1.2. Research goal

For full utilization of the advantages of FRC materials instead of conventional materials, proper knowledge of its material properties and structural integrity after production and during service is required. Therefore, reliable structural evaluation methods are crucial. As a result, research on structural evaluation methods, capable of an in-situ non-destructive stiffness assessment of various FRC materials, has significant engineering importance.

Mechanical testing has been one of the first stiffness assessment techniques. Different mechanical testing methods have been developed over time. These methods are representative of procedures used in the material industry and are proven to be of high accuracy [25][26]. However, the destructive fashion of mechanical testing limits its in-situ applicability.

Non-Destructive Evaluation (NDE) techniques, such as visual and tap testing, radiographic testing, electromagnetic testing, shearography, acoustic emission testing, electromagnetic testing and vibration-based testing are other techniques used for the damage detection and / or stiffness determination. These methods do however have a limited applicability since they (1) are only capable of localized damage detection, (2) can only be applied to specific material types, or (3) cannot be executed in-situ, or combinations of these three limitation factors. Ultrasonic testing (UT) techniques use mechanical waves to evaluate the properties of test objects [27]. In these methods, a short pulse of an ultrasound wave is generated by a mechanical vibration from a transducer that converts an electrical signal into mechanical motion and vice versa [22][28]. Over the years, many variants of UT have been developed [29]. Typical ultrasound configurations used in these variants are: through-transmission, pulse-echo, pitch-catch, and guided waves, all schematically visualized in figure 1.3 [24]. Implementations of these methods for the stiffness derivation of FRC-materials were proven to be effective, but lack in in-situ applicability. Ultrasonic guided waves, on the other hand, can be implemented in-situ. Ultrasonic guided waves offer the unique combined capability of large monitoring ranges and high sensitivity to structural flaws because of the relatively small frequencies / long wavelengths employed. The multi-modal and dispersive character of guided wave propagation is sensitive to the material structure and has therefore been the basis of multiple studies on the elastic properties characterization of composite laminates. Combining these features with their non-destructive nature, shows the high potential of ultrasonic guided waves in the field of NDE techniques [30][31].

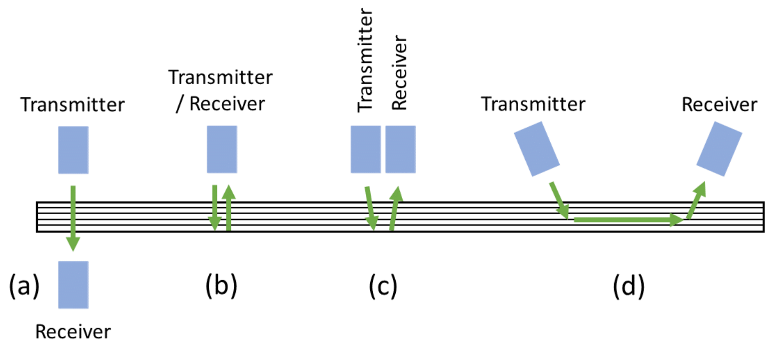

Figure 1.3: Ultrasonic testing configurations: (a) trough-transmission, (b) pulse-echo, (c) pitch-catch, and (d) guided waves.

Several studies have been conducted on the stiffness determination of FRC materials using ultrasonic guided wave methods. Most of these methods are based on an inverse procedure that determines the elastic properties by matching the results obtained using a (predictive) forward model and the results obtained using experiments [32]. The difference between both models is quantified by a fitness function, and using an optimization algorithm, this fitness function is minimized in an iterative manner by changing the input data of the forward model (model updating) until eventually the optimized input data is found. However, most of the inverse procedures used in these studies were limited to a matching principle that considered the elastic constants of individual plates as the only variable properties. Other structural properties that determine the laminate stiffness properties such as geometry and stacking were assumed to be known. This assumption is reasonable for the stiffness assessment of structures shortly after production. It is, however, less likely for in-situ structural evaluation since structures may have been in-service for a long period, leading to a potential loss of information. Therefore, more research is required to determine the laminate stiffness properties of FRC structures when less structural information is available. When this is done, the in-situ applicability of such a system needs to be taken into account. The goal of this thesis is formulated as follows:

The goal of this research is to develop a methodology that is (1) capable of a structural stiffness assessment, (2) on a wide range of FRC material types, (3) which can be applied in-situ.

1.3. Research questions

From the goal of this research, the main research question is defined as:

How can the structural laminate stiffness of Fiber Reinforced Composite materials be analyzed in-situ using ultrasonic guided waves?

To adequately answer this research question, the methodology that will be developed must comply with certain accuracy and practical standards. These design requirements are translated into three subquestions. Initially, the following subquestion has to be answered, resulting in a proposed methodology capable of meeting the design requirements.

(1) How can the stiffness matrix of a Fiber Reinforced Composite material be derived using ultrasonic guided waves?

The effectiveness of the method is partly determined by the dependency on prior structural information. Therefore, the second subquestion must be answered to validate this effectiveness and quantify the accuracy under different amounts of available information.

(2) How is the accuracy of the methodology dependent on the amount of prior structural information?

The operational field of the methodology will be partly in-situ. This means that the ideal system consists of a compact device and a reasonable measurement and analysis time, while still providing accurate results. The third subquestion aims at a balanced methodology that finds an optimal solution for these different system requirements.

(3) How can the methodology be applied in-situ while still providing an accurate stiffness assessment?

1.4. Outline

In Chapter 2, the theory and literature relevant for this research are discussed. Next, the proposed methodology is explained in Chapter 3. This methodology is examined using a numerical feasibility study in Chapter 4. Thereafter, the experiments that have been performed are explained in Chapter 5. The results of the proposed methodology, applied during the experiments, are presented in Chapter 6. Lastly, the conclusion of this research is formulated in Chapter 7 and several recommendations for future research are proposed in 8.

2

Literature Review

In this chapter, relevant literature to this thesis' topic is discussed. First, a review on the structural integrity of FRC materials is given in Section 2.1. Thereafter, a theoretical background on ultrasonic guided waves and its applications in the field of structural evaluation is given in Section 2.2. Lastly, in Section 2.3, a brief summary of this literature review is presented.

2.1. Structural integrity of FRC materials

FRC materials can be produced using multiple types of manufacturing processes, such as: hand lay-up, spray lay-up, resin transfer molding, vacuum assisted method, and autoclave processing [33]. The size and shape of an FRC structure and its usage, for example as a primary or secondary structure, determine the choice of manufacturing process [34]. Despite the difference in quality of the manufacturing processes, hardly any composite structure is defect-free produced [35]. Composite structures have a relatively high uncertainty in material properties and structural integrity after production compared to their metallic counterparts. Defects introduced during manufacture can considerably increase the probability of composite failure [36].

Manufacturing defects in FRC structures involve fiber defects such as: misalignment, wrinkling / waviness, and breakage, and matrix defects such as: voids, resin-rich and resin-poor areas [37][38]. In addition to manufacturing defects, manufacturing errors, such as lay-up errors and cure errors, can arise during manufacturing. These manufacturing errors can cause variations in the desired properties of the material. Potter [39] looked at the variability in mass/unit area of a set of 387 unidirectional prepregs, produced over 127 batches. A variation of ±2% was obtained, shown in figure 2.1. For the same set of prepregs, a maximum fiber misalignment of 3.8° was found.

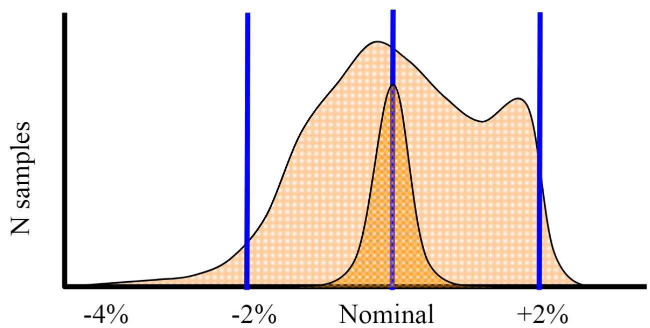

Figure 2.1: Mass/unit area distribution of 387 undirectional prepregs, produced over 127 batches [39].

2.1.1. Fiber defects

The most common manufacturing-induced fiber defects that result in decreased mechanical performance are wrinkling / waviness and misalignment [34][36]. A schematic of both phenomena is given in figure 2.2. The formation of fiber waviness is dependent on different composite manufacturing processes.

Two examples are: a trough-thickness temperature gradient due to varying thermal properties of the different constituents, and a compaction applied which increases inter-ply friction and creates out-of-plane waviness [35].

Zhao et al. [40] studied the effect of fiber waviness on the tensile properties of an unidirectional laminate. In that research a reduction of 57.7% in tenstile strength and 22.5% in tensile modulus of was reported. Similarly, Nair et al. [41] studied the effect of fiber waviness on the compressive properties of unidirectional laminates using finite element models and experimental measurements. A reduction up to 75% was observed at a wave severity of 0.075, where wave severity is defined as the wave amplitude divided by the wave length. Lastly, Khan et al. [42] observed a drop in flexural strength by 25% due to the presence of fiber waviness in woven CFRP laminates.

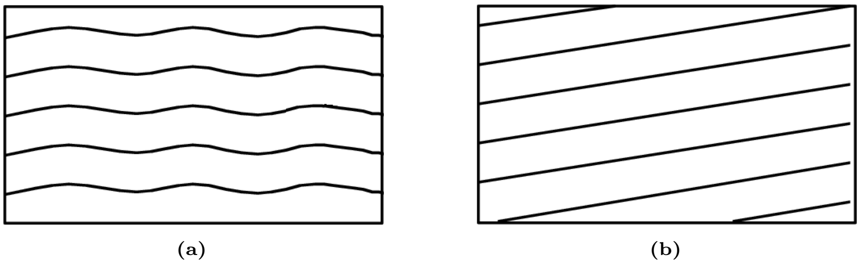

Figure 2.2: Schematic view of (a) fiber wrinkle / waviness and (b) fiber misalignment [43].

2.1.2. Matrix defects

The most common manufacturing-induced matrix defect are voids [37]. The presence of voids, which is also known as porosity, can be described as the phenomenon in which air bubbles are trapped in the matrix while the composite undergoes fabrication. This can be caused by several manufacturing factors, such as: curing pressure, cure temperature, resin system, and environmental conditions [36][44]. An example of a cross-section consisting of voids is given in figure 2.3.

The presence of voids in the structure can significantly degrade the material properties. In particular, flexural strength and modulus are extremely sensitive to void content [45]. Huang et al. [44] examined the effects of void microstructures on the elastic response of unidirectional FRC materials using FEM predictions. The results were compared to available experimental data. It was concluded that, due to the presence of voids, (a) the fiber direction moduli only reduce slightly, (b) the out-of-plane moduli degrade more than the in-plane moduli, and (c) the reduction in the principal Young's moduli show nearly linear change with the void content [44]. Rajak et al [38] and Mehdikhani et al. [46] reported that an increase of 1% of void content leads to a decrease in tensile strength of 10-20%, flexural strength of 10%, and interlaminar shear strength of 5-10%.

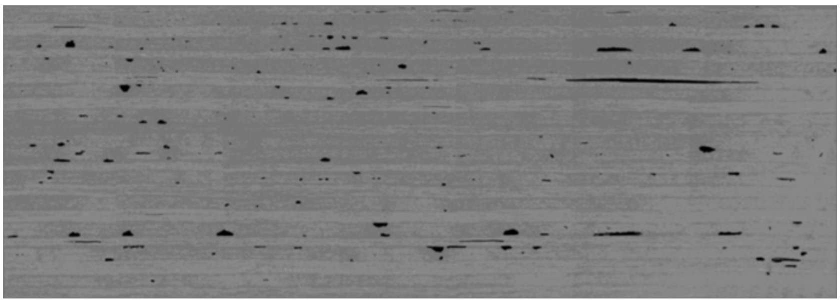

Figure 2.3: An example of a cross-section of a composite including voids colored as the black areas [47].

2.2. Ultrasonic Guided Waves

In this Section, the use of ultrasonic guided waves as structural evaluation method is discussed. First, a brief theoretical background on ultrasonic guided waves is given in Section 2.2.1. Thereafter, in Section 2.2.2, several applications of ultrasonic guided waves in the field of structural evaluation are discussed.

2.2.1. Theoretical background

When elastic waves propagate in isotropic plate-like structures, they would experience repeated reflections on the top and bottom surfaces alternately; this results in wave propagation from their mutual interference which is guided by the plate surfaces [48]. Multiple types of guided waves can be distinguished, including: Rayleigh, Love, Stoneley, Scholte, and Lamb waves [49][23]. Guided waves are made up of a superposition of longitudinal and shear wave modes [23]. Compared to bulk waves, guided waves have relatively small frequencies / long wavelengths. Since guided waves remain confined within the boundaries of the structure, they can travel over long distances, enabling the inspection of a large area with only limited use of sensors [48]. In addition, they can propagate underneath coatings, and installation of transducers for exciting and receiving of waves only requires the removal of a small part of the insulation [50]. This makes them in particular an attractive and cost-effective technique for pipeline inspection. For thin plate-like structures with free boundaries oriented parallel to each other, the utilization of Lamb waves is a prominent NDE tool [51][49].

Lamb waves propagate in two fundamental modes: symmetric (S) and antisymmetric waves (A) [52], formulated by equations 2.1 and 2.2 respectively [51]. In these equations h, k, c_l, c_T, c_p, and ω are the plate thickness, wavenumber, group velocities of the longitudinal and transverse modes, phase velocity, and wave frequency, respectively. Parameters p, q, and k are defined in equation 2.3. Additionally, a third type of guided wave, the shear horizontal (SH) wave, is often used in guided wave NDE [53]. These waves can occur in multiple orders; the zeroth-order modes of the three wave types are shown in figure 2.4.

$$\frac{\tan(qh)}{\tan(ph)} = -\frac{4k^2qp}{\left(k^2-q^2\right)^2} \qquad (2.1)$$

$$\frac{\tan(qh)}{\tan(ph)} = -\frac{\left(k^2-q^2\right)^2}{4k^2qp} \qquad (2.2)$$

$$p^2 = \frac{\omega^2}{c_L^2} - k^2, \quad q^2 = \frac{\omega^2}{c_T^2} - k^2 \quad \text{and} \quad k = \omega/c_p \qquad (2.3)$$

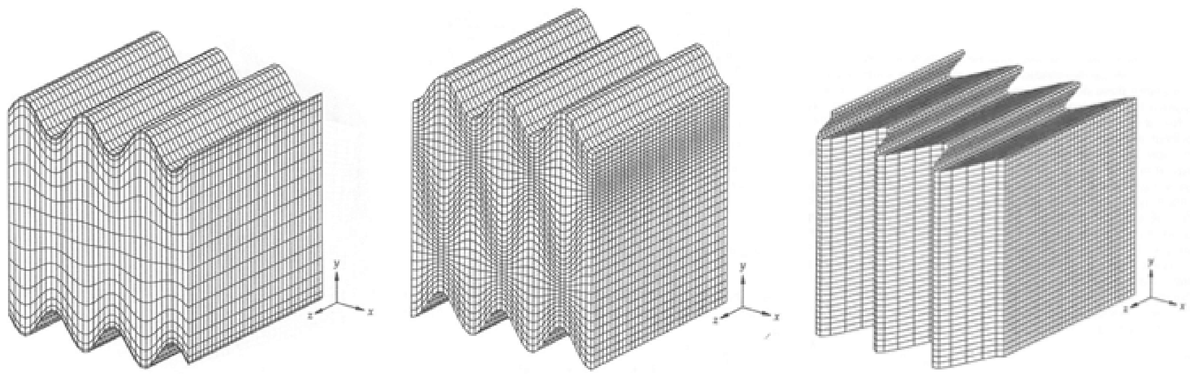

(a) **(b)** **(c)**

Figure 2.4: Examples of a zeroth-order (a) symmetric Lamb wave, (b) antisymmetric Lamb wave, and (c) shear horizontal wave.

Wave dispersion

In hardly any condition, a propagating wave consists of only one frequency. Instead, the observed motion is a superposition of multiple frequencies grouped around some center frequency ω_c. In figure 2.5, an example of such a wave packet consisting of two wave components of different frequencies is shown. The solid line of the total wave signal indicates the result of the superposition of the two wave components; this wave is called the carrier wave and has an average frequency and wavenumber of w^* and k^* respectively. The range of angular frequencies $\Delta\omega$ and wavenumbers Δk included in the carrier wave is formulated in equations 2.4 and 2.5, respectively. The dashed line in figure 2.5 represents the envelope of the combined wave. This wave is the group wave with a frequency and wavenumber of $\frac{1}{2}\Delta\omega$ and $\frac{1}{2}\Delta k$, respectively. A fixed point on this wave (with a constant phase) propagates at a group speed c_g, formulated as equation 2.6 [54].

$$\Delta\omega = \omega_{n+1} - \omega_n \qquad (2.4) \qquad \Delta k = k_{n+1} - k_n \qquad (2.5) \qquad c_g = \frac{\partial \omega}{\partial k} \qquad (2.6)$$

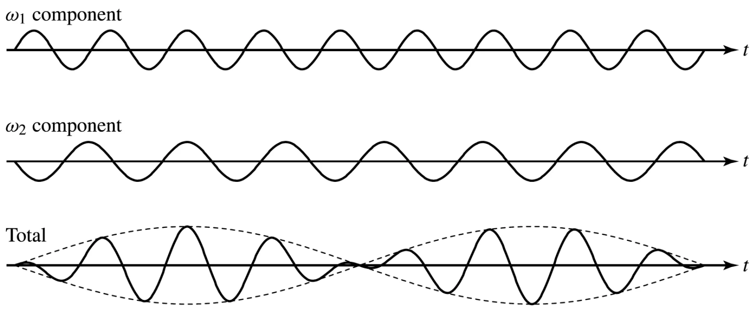

Figure 2.5: An example of a group wave consisting of two wave components [55].

The relation described above between wave velocities and frequency is called the dispersion relation. For any medium, the phase and group velocity can be derived as a function of the frequency, resulting in dispersion curves similar to those shown in figures 2.6a and 2.6b. When different components of the wave packets travel at the same phase speed, the superposed signal is non-dispersive and maintains its original shape, as visualized in figure 2.7a. However, in case the wave components propagate at different phase speeds, the shape of the superposed wave will change over time, resulting in a dispersive signal, shown in figure 2.7b. This dispersive relation of elastic waves is commonly used in both structural health monitoring systems and non-destructive inspection techniques.

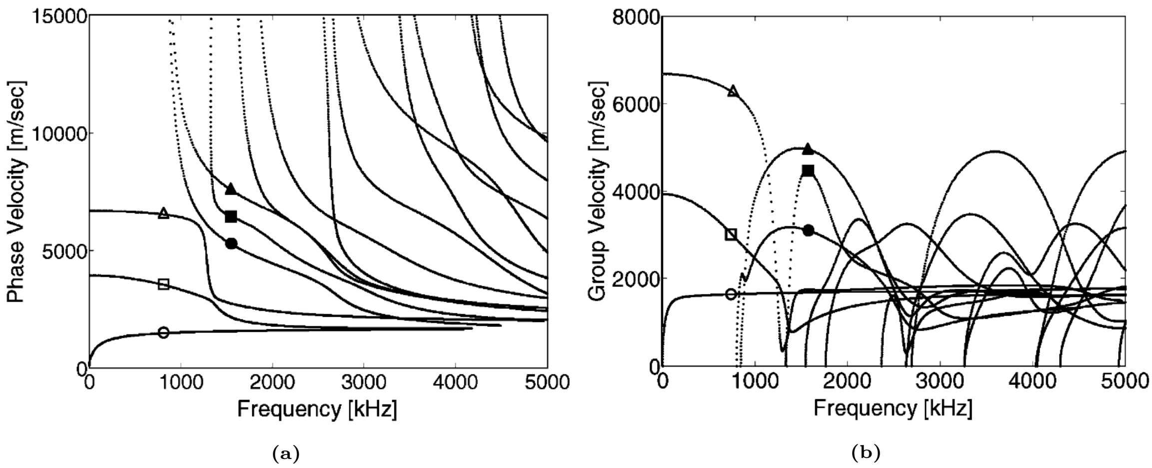

Figure 2.6: Examples of (a) phase velocity and (b) group velocity dispersion curves [56].

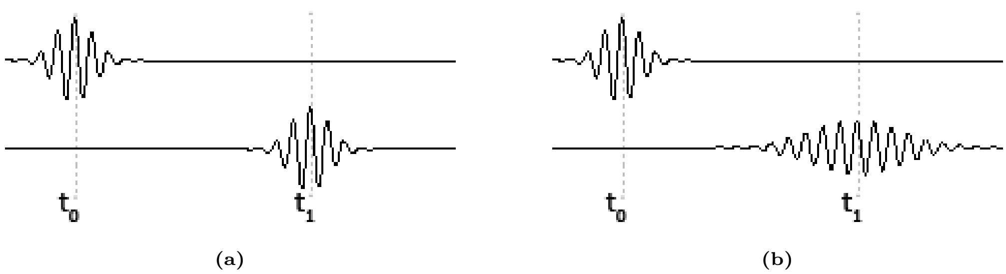

Figure 2.7: (a) Non-dispersive and (b) dispersive wave examples.

2.2.2. Applications in structural evaluation

The advantages of ultrasonic guided waves for NDE, such as large monitoring ranges and high sensitivity, can be fully exploited only once the complexities of guided wave propagation are understood and managed. The complexities of ultrasonic guided waves include the existence of multiple wave modes, the frequency-dependent velocities (dispersion), and the frequency-dependent attenuation.

Each combination of mode and frequency has an unique wave structure, which determines the sensitivity to the type and location of the damage [57][49]. For example, Rose et al. [58] concluded that the S_0 mode is more suitable for the detection of large cracks or cracks located in the middle of a plate, where the S_1 mode is more suitable for the detection of small cracks or cracks close to the free surface of the plate. The A_0 wave is highly effective in detecting delamination and transverse ply cracks [59]. In practice, the zeroth-order symmetric (S_0) and antisymmetric (A_0) modes are normally used [51][53].

In addition to the identification of damage, Lamb waves have good characteristics for the derivation of the stiffness properties of FRC materials. For anisotropic materials, the relation between elastic constants and propagation velocities is given by the Christoffel equation, which is well known to describe the propagation of an acoustic wave [60][61]. The equation is given in 2.7, where $\Gamma_{ij} = C_{ijkm} n_k n_m$ is called the Christoffel tensor, C_{ijkm} is the stiffness tensor, n_k and n_m are vector components describing the wave propagation direction, ρ is the mass density, V is the wave velocity, and δ_{ij} is the Kronecker delta [62]. Yilmaz et al. [63] used the Christoffel equation to determine the five independent elastic constants for thin anisotropic materials, being: C_{11}, C_{12}, C_{22}, C_{44}, and C_{66}, assuming the Cartesian coordinate system defined in figure 2.8, and the following transversely isotropic relations: $C_{12} = C_{13}$, $C_{33} = C_{22}$, and $C_{55} = C_{66}$. The relations between the zeroth-order symmetric Lamb wave mode and the stiffness components C_{11} and C_{22} are given by equations 2.8 and 2.9, respectively. In these equations $c_{g,S0}$ is the group velocity of the S_0 Lamb wave, which for C_{11} propagates in the x_1 and for C_{22} in the x_2-direction. The relation between the zero-order antisymmetric Lamb wave mode and the stiffness components C_{44} and C_{66} is given by equations 2.10 and 2.11, respectively, where $c_{g,A0}$ is the group velocity of the A_0 wave, which for C_{44} propagates in the x_1 direction and for C_{66} in the x_2-direction.

$$\left|\Gamma_{ij} - \delta_{ij}\rho V^2\right| \approx 0 \tag{2.7}$$

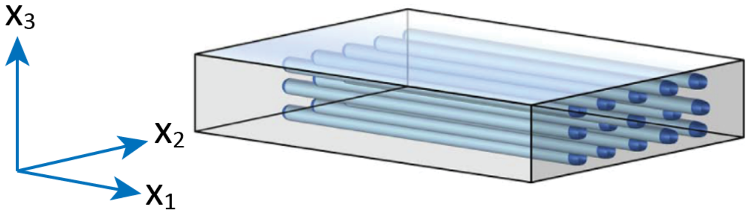

Figure 2.8: Schematic of the Cartesian coordinate system used by Yilmaz et al [63].

$$C_{11} = \rho c_{g,S0}^2 \tag{2.8}$$

$$C_{22} = \rho c_{g,S0}^2 \tag{2.9}$$

$$C_{44} = \rho c_{g,A0}^2 \tag{2.10}$$

$$C_{66} = \rho c_{g,A0}^2 \tag{2.11}$$

However, most methodologies that aim to determine structural stiffness using ultrasonic waves are based on an inverse procedure. Such a procedure matches the experimental dispersion curves and the predictions of a forward model, usually by means of optimization techniques [64]. Therefore, robust predictive models (forward models) of wave speeds are of great importance. Vishuvardhan et al. [65] used a single-transmitter-multiple-receiver (STMR) array, where one transmitter is encircled by multiple receivers at an interval of 10°. This method was used to identify the nine elastic constants of a 3.15 mm thick graphite-epoxy orthotropic plate using the Christoffel equation as the forward model. A genetic algorithm was used to reconstruct the elastic constants and minimize the fitness function between the

S_0 and A_0 velocities of the forward model and experimental data. It was observed that C_{44} and C_{55} are more sensitive to the A_0 mode velocity and the remaining seven elastic constants are more sensitive to the S_0 mode velocity. In this research, two different experiments were carried out. In the first experiment, a PZT based STMR array was used to record the diagnostic wave signal, while in the second experiment a laser vibrometer was used. The experimental velocities obtained in the second experiment turned out to be more accurate. The maximum error in the elastic moduli reconstructed using the PZT based STMR array was less than 8.5% and the maximum standard deviation was 5% from the theoretical elastic moduli. The maximum error and standard deviation for the laser based experiments were less than 7.5% and 4.75%.

Castaings et al. [66] measured the wave phase velocity of the S_0, S_1, A_0, A_1, SH_0, and SH_1 wave modes propagating in three planes that form $0°, 45°$, and $90°$ angles with the material fibers of an unidirectional glass-epoxy composite. The velocities were compared with a forward model based on the stiffness transfer matrix approach. This study did not contain a match between experimental and theoretical results, instead the elastic moduli used as input for the forward model were obtained using an immersion ultrasonic matching technique developed by Hosten [67]. Good agreement was obtained between the measured and predicted phase velocities. This demonstrates the performance of the numerical model to describe dispersion curves.

Multiple approaches and programs are developed for the derivation of dispersion curves in a forward model. Each approach has its own advantages and disadvantages, making it suitable for a specific end use and less suitable for others. Besides the Christoffel equation and the stiffness transfer matrix approach [68], some other approaches are the global matrix approach [69], the local interaction simulation approach [70], and the unified analytical method [71]. However, the Semi-Analytical Finite Element (SAFE) method is a particularly efficient tool for calculating phase or group velocity dispersion curves of multilayered composite laminates and is commonly used in NDE. The principle of the SAFE method is well described by Barazanchy and Giurgiutiu [71] and Bartoli et al. [56]. The SAFE method assumes plane strain behavior and uses a finite element discretization of the cross-section of the waveguide alone, which allows the modeling of any arbitrary cross-section. The displacement along the wave propagation direction is described in an analytical fashion as harmonic exponential functions. This makes it more efficient in terms of computational time and memory than a complete FEM [68]. Figure 2.9 shows a discretization of wave propagation in the x-direction used in the SAFE model, assuming an infinitely wide plate and three-node elements. At each node, the harmonic displacement, stress, and strain are formulated. The equation of motion in the cross-section is expressed by Hamilton's equation [72] and the SAFE solutions are obtained in a stable manner from an eigenvalue problem.

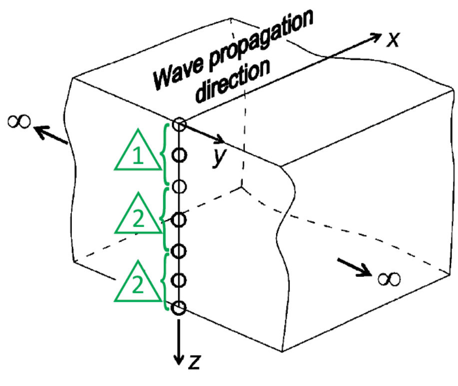

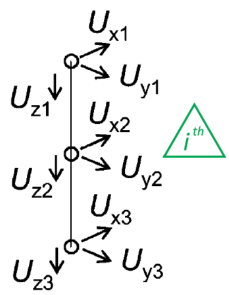

Figure 2.9: (a) Schematic SAFE model of wave propagation in x-direction. (b) Degrees of freedom of a three-node element [56].

Sale et al. [73] applied the SAFE method as a forward model to estimate the elastic properties of a 2.54-millimeter thick aluminum plate. The S_0 and A_0 dispersion curves obtained using the SAFE method were compared with numerical and experimental data. The numerical study was conducted using the commercial software ANSYS, the experimental dispersion curves were determined by adopting a hybrid laser ultrasonic / PZT set-up. Reconstruction of the elastic properties was achieved through an inversion scheme based on the simplex search method. Three reconstruction approaches were studied: (1) matching based only on the S_0 mode, (2) matching based only on the A_0 mode, and (3) matching based on both modes. The best results were found by monitoring both modes simultaneously.

Marzani et al. [74] used a similar approach using the SAFE method and genetic algorithm. In this study, the elastic moduli of isotropic aluminum, unidirectional and cross-ply graphite-epoxy plates were derived. For each experiment, in addition to the S_0 and A_0 modes, the matching principle was based on the SH_0 wave mode. Instead of real experimental data, pseudo-experimental data was used, therefore synthetically simulated waveforms were corrupted with different levels of superimposed white Gaussian noise, resulting in a signal-to-noise ratio (SNR) of 20, 10 or 5 dB. The elastic constants of each ply were assumed to be the same. For the isotropic plate the wave velocities were measured in one direction, the mean error for an SNR of 5 dB was 5% and 10% for C_{11} and C_{12}, respectively. The estimate of C_{66} was much more precise and almost insensitive to the noise level. For the unidirectional plate, wave velocities were measured in the 0° and 90° directions. Except for C_{12}, for which the mean identification error was 12.8%, the other moduli were well identified with a maximum mean error of 5.9% for C_{23}. Lastly, for the cross-ply plate, wave velocities were used in the directions $0°, 45°, 46°$, and 90°. At the same SNR level, the errors for C_{12} and C_{13} were 17.4% and 20.1%, respectively, where the other moduli had a maximum error of 8.0%.

Rui et al. [75] used a simulated annealing optimization instead of a genetic algorithm to derive the elastic moduli of an eight-ply unidirectional, sixteen-ply quasi-isotropic, and sixteen-ply anisotropic laminate. Similarly to Marzani, the matching was based on pseudo-experimental data using three wave modes. However, the velocities were measured in a single direction. Similar promising results were obtained. In addition to that, it was concluded that $E_{11}, E_{22}, E_{33}, v_{12}$, and v_{13} are most sensitive to, and therefore can be best obtained by, the S_0 and A_0 modes. Shear moduli G_{12} and G_{23} are more sensitive to SH_0. Furthermore, transverse rigidities K_x and K_y can be effectively identified by the modes S_0 and A_0 propagating along the x-direction (0° fiber direction) in all laminate cases.

2.3. Chapter summary

In the literature review, the relevance of structural integrity as a complication for FRC materials has been illustrated. Defects and errors introduced during manufacturing can considerably increase the probability of composite failure. This emphasizes the importance of reliable structural evaluation methods.

Furthermore, it is concluded that the characteristics of ultrasonic guided waves are strongly related to structural stiffness. In Section 2.2.2, it was concluded that the multimodal, direction-dependent, and dispersive characteristics of ultrasonic guided waves are features that can be utilized to derive the stiffness properties of a composite laminate. Also, it was observed that zeroth-order symmetric (S_0) and antisymmetric (A_0) wave modes are most often used in guided wave NDE techniques because of their high sensitivity to structural stiffness and because they are convenient to measure.

3

Methodology

In this thesis, a new methodology is proposed to characterize the stiffness properties of FRC materials. This methodology is based on a coupling principle between the structural stiffness properties of a laminate and the ultrasonic guided wave characteristics. First, the general idea of the methodology is discussed in Section 3.1. Thereafter, the detailed structure of the methodology and several considerations of the system are described in Section 3.2. Lastly, a hypothesis of the methodology is formulated in Section 3.3.

3.1. General idea

In this methodology, S_0 and A_0 waves are used. At low frequencies, the S_0 wave can be approximated using the equation of motion for elastic longitudinal waves. This equation of motion can be described in its simplest available model using the elementary rod theory [54], assuming a long and slender rod, only 1-D axial stress, and neglecting the lateral contraction (the Poisson's ratio effect). Taking into account the schematic in figure 3.1, this equation of motion is formulated as equation 3.1. In this equation E, A, η, and q are the Young's modulus, the transverse area per unit length, the damping coefficient, and the externally applied axial force per unit length, respectively. Using spectral analysis and under the assumption of uniform structural properties and an undamped system, the phase (c) and group velocity (c_g) are formulated as in 3.2 and 3.3, respectively. From these dispersion relations, it can be concluded that both velocities are independent of the wave frequency (ω) and are therefore non-dispersive at low frequencies.

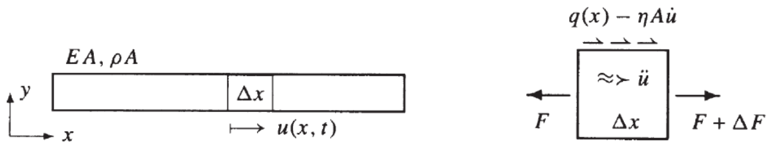

Figure 3.1: Segment of rod and a loaded element [54].

$$\frac{\partial}{\partial x}\left[EA\frac{\partial u}{\partial x}\right] + \rho A\frac{\partial^2 u}{\partial t^2} + \eta A\frac{\partial u}{\partial t} = q(x,t) \tag{3.1}$$

$$c = \frac{\omega}{k} = \sqrt{\frac{EA}{\rho A}} \tag{3.2}$$

$$c_g = \frac{d\omega}{dk} = \sqrt{\frac{EA}{\rho A}} \tag{3.3}$$

For low frequencies the A_0 wave mode can be approximated as elastic flexural waves. Flexural waves in beams can be described using the Bernoulli-Euler beam theory [54]. Here, the deflections of the centerline ($v(x,t)$) are assumed to be small, transverse, and constant through the thickness, see figure 3.2. The resulting equation of motion is formulated as in 3.4, where I is the second moment of area and EI is the flexural stiffness. Solving this equation using spectral analysis, under the same assumptions as for the longitudinal formulation, results in the formulation for the phase and group velocity given in equations 3.5 and 3.6, respectively. Unlike the S_0 dispersion relations, the A_0 relations depend on ω and, therefore, are dispersive at low frequencies.

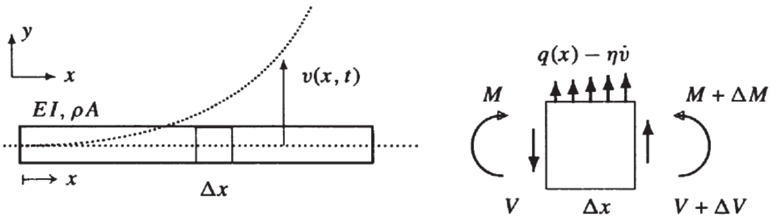

Figure 3.2: Segment of slender beam and a loaded element [54].

$$\frac{\partial^2}{\partial x^2}\left[EI\frac{\partial^2 v}{\partial x^2}\right] + \rho A\frac{\partial^2 v}{\partial t^2} + \eta A\frac{\partial v}{\partial t} = q(x,t) \tag{3.4}$$

$$c \equiv \frac{\omega}{k} = \sqrt{\omega}\left[\frac{EI}{\rho A}\right]^{1/4} \tag{3.5}$$ $$c_g \equiv \frac{d\omega}{dk} = 2\sqrt{\omega}\left[\frac{EI}{\rho A}\right]^{1/4} \tag{3.6}$$

When assuming constant structural properties ρ, A, and I and constant wave frequency (ω), equations 3.3 and 3.6 can be rewritten to proportional relations 3.7 and 3.8, respectively, indicating the relation between the material stiffness E and the group velocity (c_g).

$$c_{g,S_0}^2 \propto E \tag{3.7}$$ $$c_{g,A_0}^4 \propto E \tag{3.8}$$

The Classical Laminate Theory (CLT) is commonly used to describe the behavior of composite materials under different types of loading conditions. In this method, the stiffness properties are captured in the ABD-matrix, calculated using the formulations in 3.9. The diagonal stiffness components A_{ii}, B_{ii}, and D_{ii} are proportional to E_{ii}, the relations 3.7 and 3.8 can therefore be rewritten to the relations given in formulation 3.10 and 3.11, respectively. In these equations, I_0, I_1, and I_2 are the mass moment of inertia, defined as in equation 3.12 in which h is the thickness of the ply.

$$[A] = \sum_{k=1}^{N_{\text{plies}}} [\bar{Q}]^{(k)}\left(z_k - z_{k-1}\right) \quad [B] = \sum_{k=1}^{N_{\text{plies}}} \frac{1}{2}[\bar{Q}]^{(k)}\left(z_k^2 - z_{k-1}^2\right) \quad [D] = \sum_{k=1}^{N_{\text{plies}}} \frac{1}{3}[\bar{Q}]^{(k)}\left(z_k^3 - z_{k-1}^3\right) \tag{3.9}$$

$$c_{g,S_0}^2 \propto \frac{A_{ii}}{I_0} \qquad c_{g,S_0}^2 \propto \frac{B_{ii}}{I_1} \qquad c_{g,S_0}^2 \propto \frac{D_{ii}}{I_2} \tag{3.10}$$

$$c_{g,A_0}^4 \propto \frac{A_{ii}}{I_0} \qquad c_{g,A_0}^4 \propto \frac{B_{ii}}{I_1} \qquad c_{g,A_0}^4 \propto \frac{D_{ii}}{I_2} \tag{3.11}$$

$$\left\{\begin{array}{c} I_0 \\ I_1 \\ I_2 \end{array}\right\} = \int_{-\frac{h}{2}}^{\frac{h}{2}} \rho \left\{\begin{array}{c} 1 \\ z \\ z^2 \end{array}\right\} dz \tag{3.12}$$

The proposed methodology is based on the proportional relations in 3.10 and 3.11. It is assumed that it is possible to describe the squared velocity of the group wave as a linear function of the ABD-components using a set of coupling coefficients (c_i). The assumed mathematical formulation of this relation is given in 3.13. The quality of this assumption will be investigated and demonstrated in Chapter 4. It is assumed that this relation can be set up for the S_0 and A_0 wave mode, at any frequency and along any propagation direction, resulting in a system of linear equations as in equation 3.14. This system describes the propagation characteristics of ultrasonic guided waves within a composite laminate with certain stiffness properties. These stiffness properties are collected in the $\{\boldsymbol{ABD}\}$-vector of equation 3.15. Based on this system, it would be possible to approximate the $\{\boldsymbol{ABD}\}$-vector using an inverse procedure when the coefficient matrix $\boldsymbol{C}$ is known and the velocity vector $\{\boldsymbol{c_g}^2\}$ is experimentally derived.

$$c_1 A_{11} + c_2 A_{12} + c_3 A_{16} + \cdots + c_{27} D_{66} = c_g^2 \tag{3.13}$$

$$\boldsymbol{C}\{\boldsymbol{ABD}\}^{\mathrm{T}} = \{\boldsymbol{c_g^2}\} \tag{3.14}$$

$$\{\boldsymbol{ABD}\} = \{\begin{array}{ccccccccccccc} A_{11} & A_{12} & \cdots & A_{66} & | & B_{11} & B_{12} & \cdots & B_{66} & | & D_{11} & D_{12} & \cdots & D_{66} \end{array}\} \tag{3.15}$$

3.2. System considerations

The accuracy of the proposed stiffness approximation is determined by (1) the inclusion of wave characteristics described in the system, (2) the accuracy of the coupling coefficients, and (3) the accuracy of the experimental data used as input to the system. In the continuation of the report, the first two factors will be referred to as the numerical accuracy factors, where the third factor will be referred to as the experimental accuracy factor. These three factors will be explained in more detail in this section. This is done by assuming a complete random composite Plate of Interest (PoI) of which no axis of symmetry is known, meaning that the total number of independent ABD-components, and thus of the number of coupling coefficients in equation 3.13, is equal to 27.

3.2.1. Inclusion of wave characteristics

In this part, the first numerical factor that determines the accuracy of the $\{\boldsymbol{ABD}\}$ approximation is discussed.

The inclusion of wave characteristics is related to the extent to which the multimodal, direction-dependent, and dispersive character of guided waves is included in the system. Therefore, equation 3.14 is built up based on these three characters. In equation A.3 of Appendix A, the detailed structure of equation 3.14 is shown. The structure of equation A.3 is described in this section, starting with (a) the multimodal character, followed by (b) the direction-dependent character, and (c) the dispersive character.

(a) Multimodal character

The inclusion of wave characteristics described in the system depends on the number of wave modes described. In the literature, it was concluded that the S_0 and A_0 wave modes have a high sensitivity to structural stiffness. In addition, these modes are relatively easy to measure during experiments. For that reason, both modes are used in the system. Consequently, the coefficient matrix $\boldsymbol{C}$ is split into a $\boldsymbol{D_S}$ and a $\boldsymbol{D_A}$ part, both consisting of the coupling coefficients related to its corresponding wave modes, see equation 3.16. By doing this, a part of the multimodal features of guided waves is now taken into account in the system.

$$\boldsymbol{C} = \begin{bmatrix} \boldsymbol{D_S} & \boldsymbol{D_A} \end{bmatrix}^{\mathrm{T}} \tag{3.16}$$

(b) Direction-dependent character

Next, the directional dependence of wave modes is included in the system by splitting the mode-dependent coefficient matrices $\boldsymbol{D_A}$ and $\boldsymbol{D_S}$ into separate matrices for multiple propagation directions $i = (\theta_1, \theta_2, \cdots, \theta_d)$, where d is the total number of propagation directions included in the system. The split matrices $\boldsymbol{D_A}$ and $\boldsymbol{D_S}$ are defined in equation 3.17, where $\boldsymbol{d_{S_i}}$ and $\boldsymbol{d_{A_i}}$ indicate the coefficient matrices of wave modes S_0 and A_0, respectively, both propagating in direction i.

$$\begin{aligned} \boldsymbol{D_S} &= \begin{bmatrix} \boldsymbol{d_{S_1}} & \boldsymbol{d_{S_2}} & \boldsymbol{d_{S_i}} & \cdots & \boldsymbol{d_{S_d}} \end{bmatrix}^{\mathrm{T}} \\ \boldsymbol{D_A} &= \begin{bmatrix} \boldsymbol{d_{A_1}} & \boldsymbol{d_{A_2}} & \boldsymbol{d_{A_i}} & \cdots & \boldsymbol{d_{A_d}} \end{bmatrix}^{\mathrm{T}} \end{aligned} \quad \text{where } i = (\theta_1, \theta_2, \cdots, \theta_d) \tag{3.17}$$

(c) Dispersive character

To include the dispersive character of wave modes, the directional-dependent coefficient matrices $\boldsymbol{d_{S_i}}$ and $\boldsymbol{d_{A_i}}$ are split into separate matrices for multiple wave frequencies $j = (\omega_1, \omega_2, \cdots, \omega_f)$, where f is the total number of wave frequencies included in the system. The same splitting procedure is used as in the previous step, resulting in the split matrices $\boldsymbol{d_{S_i}}$ and $\boldsymbol{d_{A_i}}$ defined in equation 3.18. In this equation, $\{\boldsymbol{f_{S_{i,j}}}\}$ and $\{\boldsymbol{f_{A_{i,j}}}\}$ indicate the coefficient vectors of the wave mode S_0 and A_0 propagating in the direction i at wave frequency j.

$$\begin{aligned} \boldsymbol{d_{S_i}} &= \begin{bmatrix} \{\boldsymbol{f_{S_{i,1}}}\} & \{\boldsymbol{f_{S_{i,2}}}\} & \{\boldsymbol{f_{S_{i,j}}}\} & \cdots & \{\boldsymbol{f_{S_{i,f}}}\} \end{bmatrix}^{\mathrm{T}} \\ \boldsymbol{d_{A_i}} &= \begin{bmatrix} \{\boldsymbol{f_{A_{i,1}}}\} & \{\boldsymbol{f_{A_{i,2}}}\} & \{\boldsymbol{f_{A_{i,j}}}\} & \cdots & \{\boldsymbol{f_{A_{i,f}}}\} \end{bmatrix}^{\mathrm{T}} \end{aligned} \quad \text{where } j = (\omega_1, \omega_2, \cdots, \omega_f) \tag{3.18}$$

The final result of this breakdown of the coefficient matrix $\boldsymbol{C}$ are the directional and frequency dependent coefficient vectors $\{\boldsymbol{f_{S_{i,j}}}\}$ and $\{\boldsymbol{f_{A_{i,j}}}\}$ for the S_0 and A_0 wave mode, respectively. These vectors consist of a single coefficient for each ABD-component as shown in the equations of 3.19.

$$\begin{aligned} \{\boldsymbol{f_{S_{i,j}}}\} &= \{\; c_{S_0,i,j,A_{11}} \quad c_{S_0,i,j,A_{12}} \quad c_{S_0,i,j,A_{16}} \quad \cdots \quad c_{S_0,i,j,D_{66}} \;\} \\ \{\boldsymbol{f_{A_{i,j}}}\} &= \{\; c_{A_0,i,j,A_{11}} \quad c_{A_0,i,j,A_{12}} \quad c_{A_0,i,j,A_{16}} \quad \cdots \quad c_{A_0,i,j,D_{66}} \;\} \end{aligned} \tag{3.19}$$

The same systematic structure build-up is used for the velocity vector $\{\boldsymbol{c_g^2}\}$ of equation 3.14. First, this vector is split into a symmetric $\{\boldsymbol{c_{gS}^2}\}$ and an antisymmetric $\{\boldsymbol{c_{gA}^2}\}$ wave mode part, as shown in equation 3.20. Next, these matrices are split into the directional dependent matrices $\{\boldsymbol{c_{gS_i}^2}\}$ and $\{\boldsymbol{c_{gA_i}^2}\}$ in equation 3.21. Since the right side of equation 3.13 consists only of one element, in contrast to the breakdown of the coefficient matrix, this was the last step for the velocity vector. The final results are the directional and frequency-dependent velocity vectors $\{\boldsymbol{c_{gS_i}^2}\}$ and $\{\boldsymbol{c_{gA_i}^2}\}$ for wave modes S_0 and A_0, respectively, given in equation 3.22. These vectors consist of the group velocities for all combinations of the included wave propagation directions (θ) and frequencies (ω).

$$\{\boldsymbol{c_g}^2\} = \{\; \boldsymbol{c_{gS}^2} \quad \boldsymbol{c_{gA}^2} \;\} \tag{3.20}$$

$$\begin{aligned} \{\boldsymbol{c_{gS}^2}\} &= \{\; \boldsymbol{c_{gS_1}^2} \quad \boldsymbol{c_{gS_2}^2} \quad \boldsymbol{c_{gS_i}^2} \quad \cdots \quad \boldsymbol{c_{gS_d}^2} \;\}^{\mathrm{T}} \\ \{\boldsymbol{c_{gA}^2}\} &= \{\; \boldsymbol{c_{gA_1}^2} \quad \boldsymbol{c_{gA_2}^2} \quad \boldsymbol{c_{gA_i}^2} \quad \cdots \quad \boldsymbol{c_{gA_d}^2} \;\}^{\mathrm{T}} \end{aligned} \quad \text{where } i = (\theta_1, \theta_2, \cdots, \theta_d) \tag{3.21}$$

$$\begin{aligned} \{\boldsymbol{c_{gS_i}^2}\} &= \{\; c_{gS_0,i,1}^2 \quad c_{gS_0,i,2}^2 \quad c_{gS_0,i,j}^2 \quad \cdots \quad c_{gS_0,i,f}^2 \;\}^{\mathrm{T}} \\ \{\boldsymbol{c_{gA_i}}^2\} &= \{\; c_{gA_0,i,1}^2 \quad c_{gA_0,i,2}^2 \quad c_{gA_0,i,j}^2 \quad \cdots \quad c_{gA_0,i,f}^2 \;\}^{\mathrm{T}} \end{aligned} \quad \text{where } j = (\omega_1, \omega_2, \cdots, \omega_f) \tag{3.22}$$

The structure of coefficient matrix $\boldsymbol{C}$ and velocity vector $\{\boldsymbol{c_g^2}\}$ has been discussed. This structure determines the completeness of the wave propagation characteristics included in the system. The final structure of the matrices $\boldsymbol{C_S}$, $\boldsymbol{C_A}$, $\boldsymbol{C}$ and equation 3.14 can be found in Appendix A. Two wave modes are included in the system, mode S_0 and A_0. Increasing the number of propagation directions (θ) (increasing d), and increasing the number of wave frequencies (ω) at which the velocities of the group wave are measured (increasing f), results in a more complete description of the wave characteristics. Therefore, this is expected to result in a better $\{\boldsymbol{ABD}\}$-approximation. This will be investigated in Chapter 4. When the number of linear equations included in the system is greater than the number of DoF, the system is overdetermined. The solution for such systems can be approximated using the Least Squares Approach.

3.2.2. Determination of the coupling coefficients

This part will cover the second numerical factor that determines the accuracy of the $\{\boldsymbol{ABD}\}$-approximation. Here, the derivation of the coupling coefficients, captured in matrix $\boldsymbol{C}$ of equation 3.14 and described in equation 3.19, is described.

The coupling coefficients are determined on the basis of the composite plate of interest. The great freedom in the design process of composite laminates is provided by the wide variability in design properties, such as material type, stacking sequence, and plate / ply thickness. As a result, a wide range of possible stiffness properties can be obtained using composite laminates. On the basis of prior information of the plate of interest, this wide range of possible stiffness properties can be narrowed down to a reduced range of stiffness possibilities. In the proposed method, this range of interest is captured in the coupling coefficients. This is done by numerically determining the coefficients based on a batch of M reference laminates (p_n) whose stiffness properties cover the entire range of possible stiffness. Mathematically, this can be expressed by equation 3.23. Each set of coupling coefficients as described in equation 3.19 is determined separately using equation 3.23 and is represented as vector $\{\boldsymbol{c}\}$ in the same equation. The matrix $[\boldsymbol{ABD_{ref}}]$ consists of a set of ABD-components for each reference laminate (p_n). These sets of components are determined using the Classical Laminate Theory (CLT) and are each stored on a different row in $[\boldsymbol{ABD_{ref}}]$. Similarly, the vector $\{\boldsymbol{c_{g,ref}}^2\}$ is filled row-wise with the wave velocities of each reference laminate (p_n), where the wave velocity corresponds to the mode, direction, and frequency for which the coefficients are determined.

In the literature, the SAFE method has been described as a very suitable method to numerically describe the wave propagation characteristics of guided waves within an arbitrary cross-section [71][56]. Therefore, the SAFE method is used to fill the velocity vector $\{\boldsymbol{c^2_{g,ref}}\}$ with the squared wave velocities for each reference laminate. A detailed description of the SAFE method is given in Appendix B.

$$[\boldsymbol{ABD_{ref}}]\,\{\boldsymbol{c}\} = \{\boldsymbol{c^2_{g,ref}}\} \tag{3.23}$$

$$[\boldsymbol{ABD_{ref}}] = \begin{bmatrix} A_{11,p_1} & A_{12,p_1} & A_{16,p_1} & \cdots & D_{66,p_1} \\ A_{11,p_2} & A_{12,p_2} & A_{16,p_2} & \cdots & D_{66,p_2} \\ A_{11,p_n} & A_{12,p_n} & A_{16,p_n} & \cdots & D_{66,p_n} \\ \vdots & \vdots & \vdots & & \vdots \\ A_{11,p_M} & A_{12,p_M} & A_{16,p_M} & \cdots & D_{66,p_M} \end{bmatrix} \tag{3.24}$$

$$\{\boldsymbol{c}\} = \{\ c_1 \quad c_2 \quad \cdots c_{27}\ \}^{\mathrm{T}} \tag{3.25}$$

$$\{\boldsymbol{c^2_{g,ref}}\} = \{\ c^2_{g,p_1} \quad c^2_{g,p_2} \quad c^2_{g,p_n} \quad \cdots \quad c^2_{g,p_M}\ \}^{\mathrm{T}} \tag{3.26}$$

When the matrix $[\boldsymbol{ABD_{ref}}]$ and the vector $\{\boldsymbol{c_{g,ref}}^2\}$ are filled with the data of each reference laminate included in batch with size M, the system can be solved for coefficients $\{\boldsymbol{c}\}$. Similarly to equation 3.14, this solution has to be approximated using the Least Squares Approach. The resulting set of coupling coefficients $\{\boldsymbol{c}\}$ can be interpreted as the coefficients that best describe the linear relation between the ABD-components and squared wave velocities of all reference laminate (p_n) included in the batch of size M.

3.2.3. Measurement of the experimental data

The third factor, the experimental accuracy factor, of this methodology is the accuracy of the experimental data used as input to the system.

The velocity vector $\{\boldsymbol{c_g}^2\}$ of equation 3.14 is experimentally derived on the composite plate of interest. Based on this velocity vector and the predetermined coefficient matrix $\boldsymbol{C}$, the vector $\{\boldsymbol{ABD}\}$ of that plate is approximated. Therefore, it is of great importance to obtain accurate experimental data. In Chapter 5, the applied measuring procedure and processing method are discussed in detail.

3.3. Hypothesis

Based on the methodology described, a hypothesis is formulated consisting of the following three statements:

- The ABD-approximation will be unstable when the range of possible stiffness properties is not adequately covered by the reference laminates included in the batch. In that case, it can be said that the batch size is too small. However, it is expected that the approximation procedure will eventually converge at a certain batch size, in any case. In figure 3.3 this expected convergence is visualized, here the approximated value of a ABD-component is plotted as a function of batch size M.

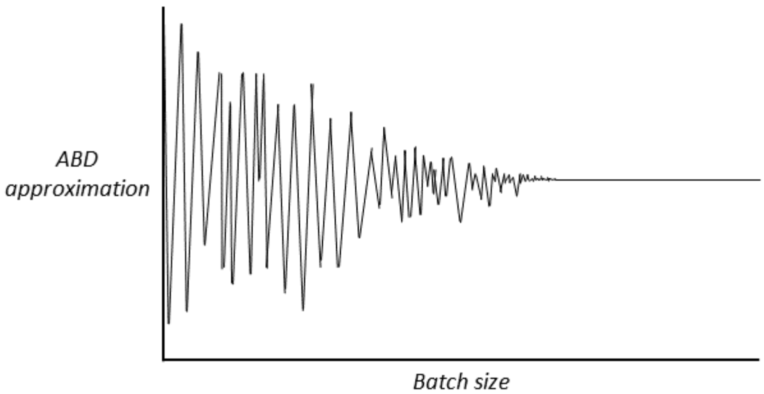

Figure 3.3: Expected convergence of the ABD-approximation as function of the batch size.

- Based on the amount of prior structural information available, the range of possible stiffness properties is determined. Therefore, the accuracy of the methodology is expected to be proportional to the available prior information of the plate of interest.
- Every structure has its own typical dispersion relations. Therefore, the accuracy of the proposed methodology is expected to be proportional to the number of wave characteristics included in the system.

4

Numerical Feasibility Study

In this chapter, a first feasibility study is carried out to evaluate the potential of the proposed methodology. First, the goal of this feasibility study is described in Section 4.1. Thereafter, in Section 4.2, the approach is described, including the different test scenarios and variants of the methodology. In Section 4.3, the results are given and in Section 4.4 the conclusion for this feasibility study is formulated.

4.1. Goal

In the previous chapter, it was stated that the accuracy at which the ABD-components of the composite plate of interest can be approximated is related to three factors: (1) the inclusion of wave characteristics described in the system, (2) the determination of the coupling coefficients, and (3) the accuracy of the experimental data used as input to the system. In Section 3.3, a hypothesis on the convergence of the methodology and the effect of the two numerical accuracy factors was formulated.

The goal of this numerical feasibility study is to judge this hypothesis and to derive a better understanding of the effect of the two numerical accuracy factors. To do this, several test scenarios will be considered, all of which have a different amount of available structural information. Furthermore, several variants of the methodology are examined. The entire feasibility study is based on numerical simulations. The goal of this feasibility study is to find answers to the following questions:

- At what batch size does the approximation converge for the different scenarios?
- What accuracy of the approximation can be achieved for the different scenarios?
- What is the effect of the included wave characteristics on the accuracy of the approximation?
- What variant of the methodology provides the best approximation?

This feasibility study is focused on the stiffness approximation of symmetric and balanced laminates, consisting only of transversely isotropic plies. The definitions of these three structural properties used in this study are defined as:

- Symmetric laminate: plies located symmetrically with respect to the midplane have exactly the same orientation, thickness, and material. Therefore, $B_{ij} = 0$ and there is no coupling stiffness [2].
- Balanced laminate: for every $+\theta$ ply, there is another $-\theta$ ply somewhere in the stacking sequence. Therefore, $A_{16} = A_{26} = 0$ and no stretching–shearing coupling occurs [76].
- Transversely isotropic plies: one of the materials principal planes is a plane of isotropy. Therefore, there are five independent material constants since: $C_{12} = C_{13}$, $C_{22} = C_{33}$, $C_{55} = C_{66}$, and $C_{44} = (C_{22} - C_{23})/2$ [2].

4.2. Approach

Three test scenarios are considered. These scenarios differ in the amount of structural information available on the plate of interest. However, the density of the material (ρ), the thickness of the ply

(t_{ply}), and the total number of plies are considered known for all cases. Test scenario **1** assumes unknown properties of the laminae and a known stacking sequence of the composite Plate of Interest (PoI). Here, the unknown properties of the laminae are Young's moduli E_1 and $E_2 = E_3$, shear moduli $G_{12} = G_{13}$ and G_{23}, and Poisson's ratios $\nu_{12} = \nu_{13}$ and ν_{23}. Scenario **2** assumes an unknown stacking sequence but known properties of the laminae. Scenario **3** is a combination of the first two scenarios and considers both the properties of the laminae and the stacking sequence to be unknown.

For each scenario, a batch of reference laminates is created, collected in the matrix $[\boldsymbol{ABD_{ref}}]$ and the vector $\{\boldsymbol{c^2_{g,ref}}\}$ of equation 3.23, using the SAFE method. From these batches, the coefficient matrix $\boldsymbol{C}$ is derived for each scenario. The batch of each scenario is created on the basis of the scenario-dependent PoI. As a starting point, the same composite PoI is used for each scenario. However, as stated above, the known and unknown properties vary for each scenario. The material properties of this plate are given in table 4.1. The properties of this laminate correspond to the properties of the plate used for the experiments, which will be discussed in more detail in Chapter 5.

Table 4.1: Material properties of composite laminate PoI used for the numerical feasibility study.

E_1 $[GPa]$	$E_2 = E_3$ $[GPa]$	$G_{12} = G_{13}$ $[GPa]$	G_{23} $[GPa]$	$\nu_{12} = \nu_{13}$ [-]	ν_{23} [-]	stacking sequence [-]	t_{ply} $[mm]$	ρ $[kg/m^3]$
46.2	13.1	4.1	5.1	0.29	0.28	[0/0/45/45/-45/-45/90/90]s	0.51	1872

Each reference laminate included in the scenario-dependent batch is generated at random. However, some boundaries are applied for the unknown properties; these are described below.

Unknown properties of the laminae

The properties of the laminae included in the batch of scenarios **1** and **3** are arbitrarily generated within 80% to 120% of the properties listed in table 4.1, which means that the exact properties of the laminae are unknown but are known to be somewhere within this range. Equation 4.1 describes this arbitrary process for E_1, variable E_{1,p_1} in this equation is the arbitrary chosen value E_1 for the reference laminate p_1, f_{rand} is a uniformly distributed random integer between 0.8 and 1.2, and $E_{1,PoI}$ is the value of E_1 of the PoI, given in table 4.1. The same equation is used for all unknown properties. Each property of the laminae (E_1, $E_2 = E_3$, $G_{12} = G_{13}$, G_{23}, $\nu_{12} =_{13}$, and ν_{23}) is randomly chosen, independently of each other.

$$E_{1,p_1} = f_{rand} \cdot E_{1,PoI} \qquad \text{where } 0.8 \leq f_{rand} \leq 1.2 \tag{4.1}$$

Unknown stacking sequence

The stacking sequences of the reference laminates included in the batch of scenarios **2** and **3** are arbitrarily chosen while taking into account the symmetric and balanced laminate criterion and the criterion of constant number of plies. The total number of plies is 16 as can be seen from the stacking sequence of the PoI in table 4.1. Regarding these criteria, this means that a total of four ply orientations (θ_i) is arbitrary chosen for each reference laminate, independent of each other and independent of other reference laminates. The possible orientations are limited to 0°, ±30°, ±45°, ±60°, and 90°.

The resulting compositions of the batches used for each scenario are shown in Section 4.2.1.

4.2.1. Scenarios

In this section, the composition of the reference laminate batch used for each scenario is discussed.

Scenario 1

Test scenario **1** assumes unknown properties of the laminae but a known stacking sequence of the PoI. The range of material properties included in the batch and the batch size are given in table 4.2. Note that the batch size in table 4.2 is not the converged batch size, but the total number of reference laminates used for this feasibility study. The spreads of the resulting ABD components included in the batch are visualized in figure 4.1.

Table 4.2: Range of properties included in the batch of scenario **1**. The stiffness properties of the laminae are calculated using a variation of equation 4.1.

E_1 $[GPa]$	$E_2 = E_3$ $[GPa]$	$G_{12} = G_{13}$ $[GPa]$	G_{23} $[GPa]$	$\nu_{12} = \nu_{13}$ [-]	ν_{23} [-]	Stacking sequence [°]	Batch size $[laminates]$
37.0 - 55.4	10.5 - 15.7	3.28 - 4.92	4.08 - 6.12	0.23 - 0.35	0.22 - 0.34	[0/0/45/45/-45/-45/90/90]s	3500

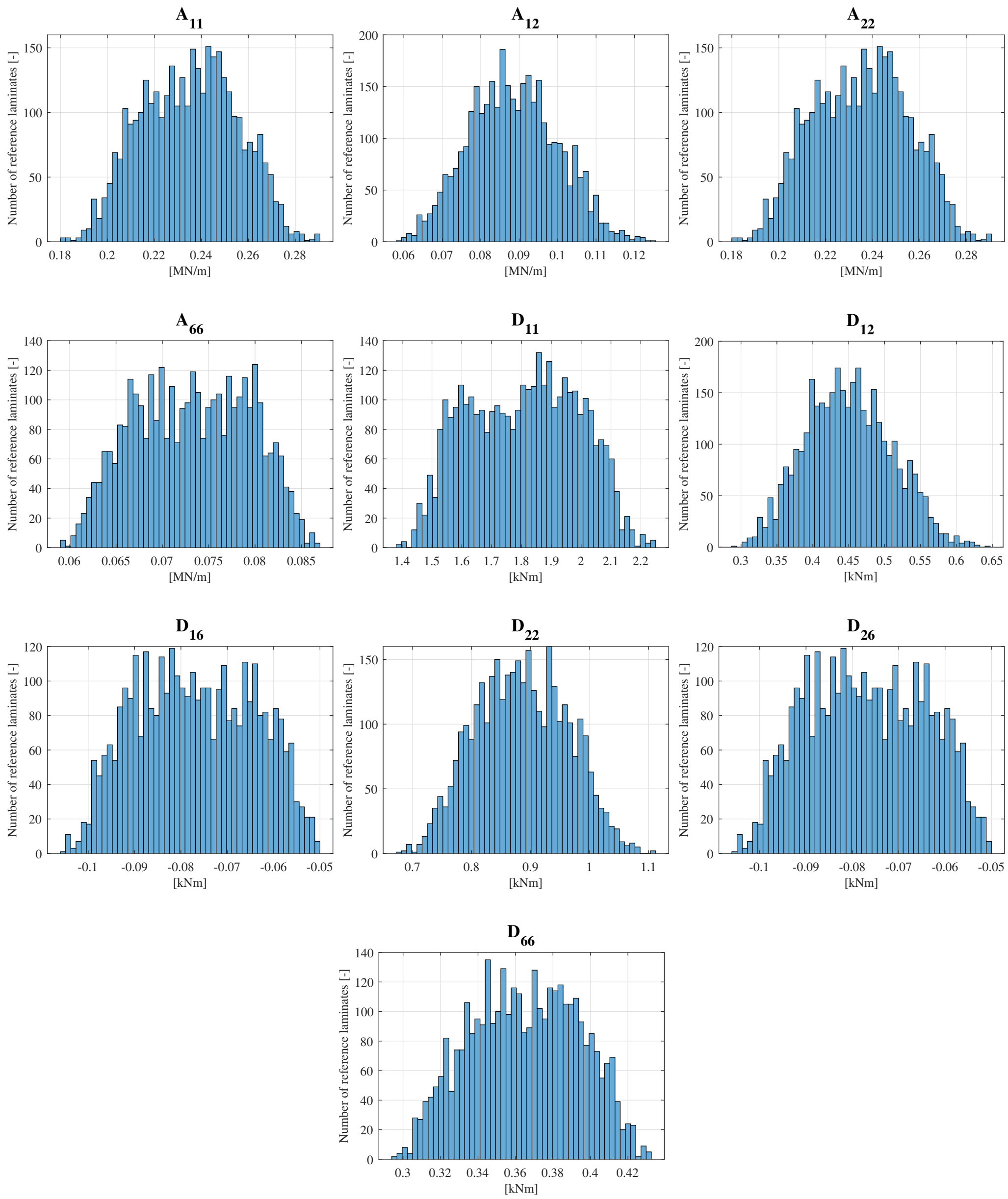

Figure 4.1: Spread of the ABD-components included in the batch of scenario **1**.

Scenario 2

Test scenario **2** assumes an unknown stacking sequence, but known laminae properties of the laminate of interest. The range of material properties included in the batch and the batch size are given in table 4.3. The spreads of the resulting *ABD*-components included in the batch are visualized in figure 4.2

Table 4.3: Range of properties included in the batch of scenario **2**. The stiffness properties of the laminae are calculated using a variation of equation 4.1.

E_1 $[GPa]$	$E_2 = E_3$ $[GPa]$	$G_{12} = G_{13}$ $[GPa]$	G_{23} $[GPa]$	$\nu_{12} = \nu_{13}$ [-]	ν_{23} [-]	Stacking sequence [°]	Batch size [laminates]
46.2	13.1	4.1	5.1	0.29	0.28	$0, \pm30, \pm45, \pm60, \text{or } 90$	2000

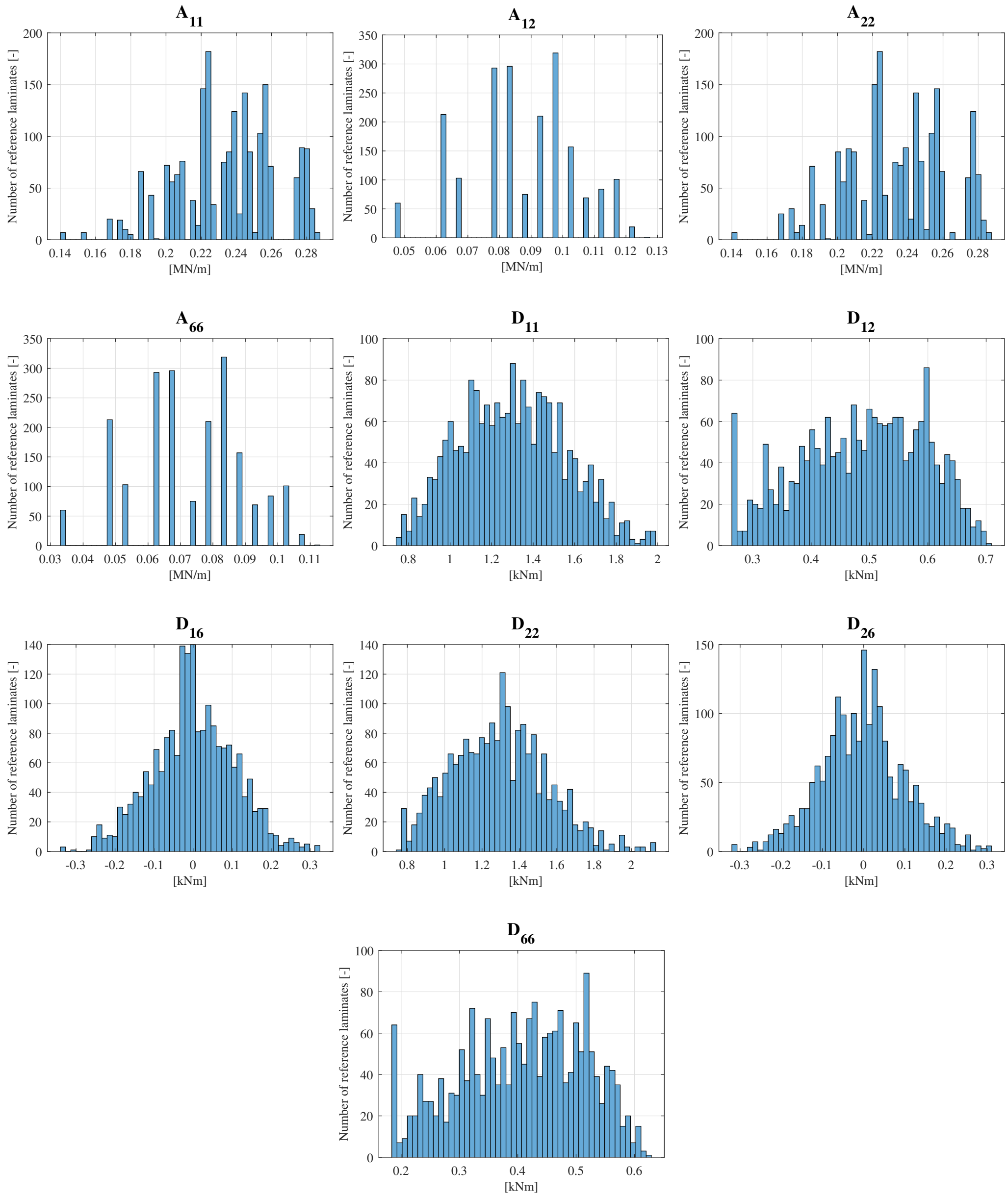

Figure 4.2: Spread of the *ABD*-components included in the batch of scenario **2**.

Scenario 3

Test scenario **3** assumes that both the properties of the laminae and the stacking sequence are unknown. The range of material properties included in the batch and the batch size are given in table 4.4. The spreads of the resulting *ABD*-components included in the batch are visualized in figure 4.3.

Table 4.4: Range of properties included in the batch of scenario **3**. The stiffness properties of the laminae are calculated using a variation of equation 4.1.

E_1 $[GPa]$	$E_2 = E_3$ $[GPa]$	$G_{12} = G_{13}$ $[GPa]$	G_{23} $[GPa]$	$\nu_{12} = \nu_{13}$ [-]	ν_{23} [-]	Stacking sequence [°]	Batch size [laminates]
37.0 - 55.4	10.5 - 15.7	3.28 - 4.92	4.08 - 6.12	0.23 - 0.35	0.22 - 0.34	0, ±30, ±45, ±60, or 90	3500

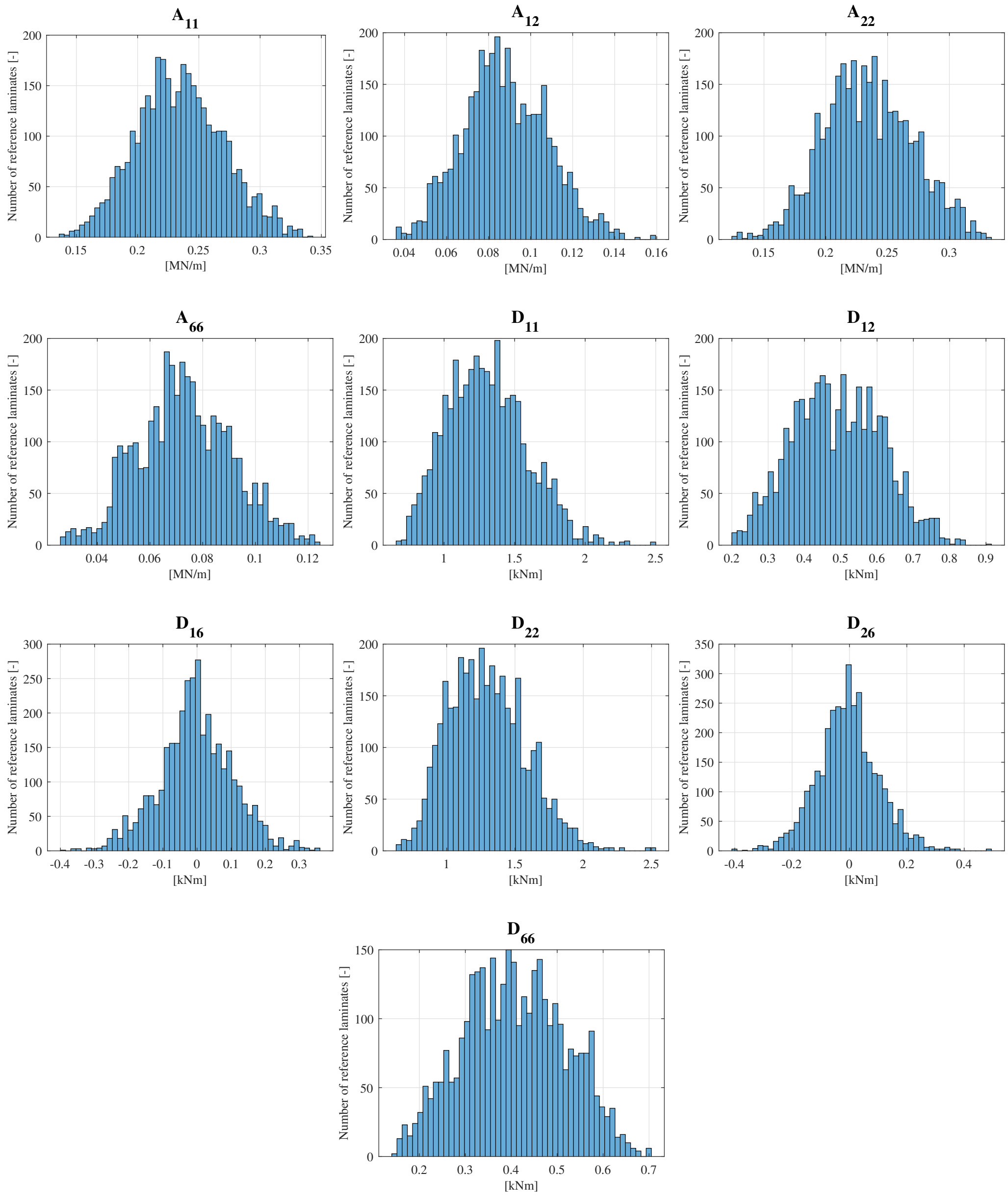

Figure 4.3: Spread of the *ABD*-components included in the batch of scenario **3**.

4.2.2. Methodology variants

Several variants of the methodology are developed. All variants are applied to the different test scenarios to obtain the highest accuracy. The variants are based on two concepts:

1. Grouping of the ABD-components.
2. Normalizing of the coupling coefficients.

Both concepts are discussed below.

Grouped $\boldsymbol{ABD}$-components

In the methodology described in Chapter 3 it was assumed that it is possible to describe the squared velocity of the group wave as a linear function of the ABD-components, formulated as equation 3.13. However, this feasibility study is limited to symmetric and balanced laminates, which means that $A_{16} = A_{26} = 0$ and $B_{ij} = 0$. Therefore, the original equation 3.13 can be simplified to equation 4.2.

$$c_1 A_{11} + c_2 A_{12} + c_3 A_{16} + \cdots + c_{27} D_{66} = c_g^2 \tag{Ref 3.13}$$

$$c_1 A_{11} + c_2 A_{12} + \cdots + c_9 A_{66} + c_{19} D_{11} + c_{20} D_{12} + \cdots + c_{27} D_{66} = c_g^2 \tag{4.2}$$

In figure 4.4 the ABD-components of scenario **1** are plotted as a function of the squared group velocity of the S_0 wave, in direction 0°, with a frequency of 40 kHz. From this figure it can be observed that there is a similar direct proportional correlation between the diagonal components A_{11}, A_{22}, A_{66}, D_{11}, D_{22}, and D_{66} and the group velocity. Other correlations can be observed between off-diagonal components A_{12}, D_{16}, and D_{26} and the group velocity; however, these correlations are less clear and / or are inversely proportional. Based on these observations, a variation on equation 4.2 is made by combining just the diagonal ABD-components into equation 4.3 and calculating the coupling coefficients, and thereafter the ABD-approximation for just these components.

$$c_1 A_{11} + c_5 A_{22} + c_9 A_{66} + c_{19} D_{11} + c_{23} D_{22} + c_{27} D_{66} = c_g^2 \tag{4.3}$$

In addition, another variation is considered that separates the approximation of the A-components and the D-components by assuming equations 4.4 and 4.5.

$$c_1 A_{11} + c_2 A_{12} + c_5 A_{22} + c_9 A_{66} = c_g^2 \tag{4.4}$$

$$c_{19} D_{11} + c_{20} D_{12} + c_{21} D_{16} + c_{23} D_{22} + c_{24} D_{26} + c_{27} D_{66} = c_g^2 \tag{4.5}$$

Both equations are variations on the original methodology; both variations can, however, also be combined, resulting in equations 4.6 and 4.7.

$$c_1 A_{11} + c_5 A_{22} + c_9 A_{66} = c_g^2 \tag{4.6}$$

$$c_{19} D_{11} + c_{23} D_{22} + c_{27} D_{66} = c_g^2 \tag{4.7}$$

Normalized coupling coefficients

There is a significant difference in magnitude of the extensional stiffness components A_{ij} and the bending stiffness components D_{ij}, this can also be observed in figure 4.4. To eliminate this difference and therefore equalize the contribution of each ABD-component, matrix $[\boldsymbol{ABD_{ref}}]$ is normalized by dividing each component by the absolute maximum component included in its column. This gives equation 4.8 in which the circled dot operator $\odot$ indicates the element-wise multiplication between the original $[\boldsymbol{ABD_{ref}}]$ matrix and the array $\{\boldsymbol{1/ABD_{max}}\}$ consisting of the absolute maximum components included in the matrix. Consequently, equation 3.14 must be adapted to equation 4.9.

$$[\boldsymbol{ABD_{ref,norm}}] = \begin{bmatrix} A_{11,p_1} & A_{12,p_1} & A_{16,p_1} & \cdots & D_{66,p_1} \\ A_{11,p_2} & A_{12,p_2} & A_{16,p_2} & \cdots & D_{66,p_2} \\ A_{11,p_n} & A_{12,p_n} & A_{16,p_n} & \cdots & D_{66,p_n} \\ \vdots & \vdots & \vdots & & \vdots \\ A_{11,p_M} & A_{12,p_M} & A_{16,p_M} & \cdots & D_{66,p_M} \end{bmatrix} \odot \begin{Bmatrix} 1/|A_{11,max}| \\ 1/|A_{12,max}| \\ 1/|A_{16,max}| \\ \vdots \\ 1/|D_{66,max}| \end{Bmatrix} \tag{4.8}$$

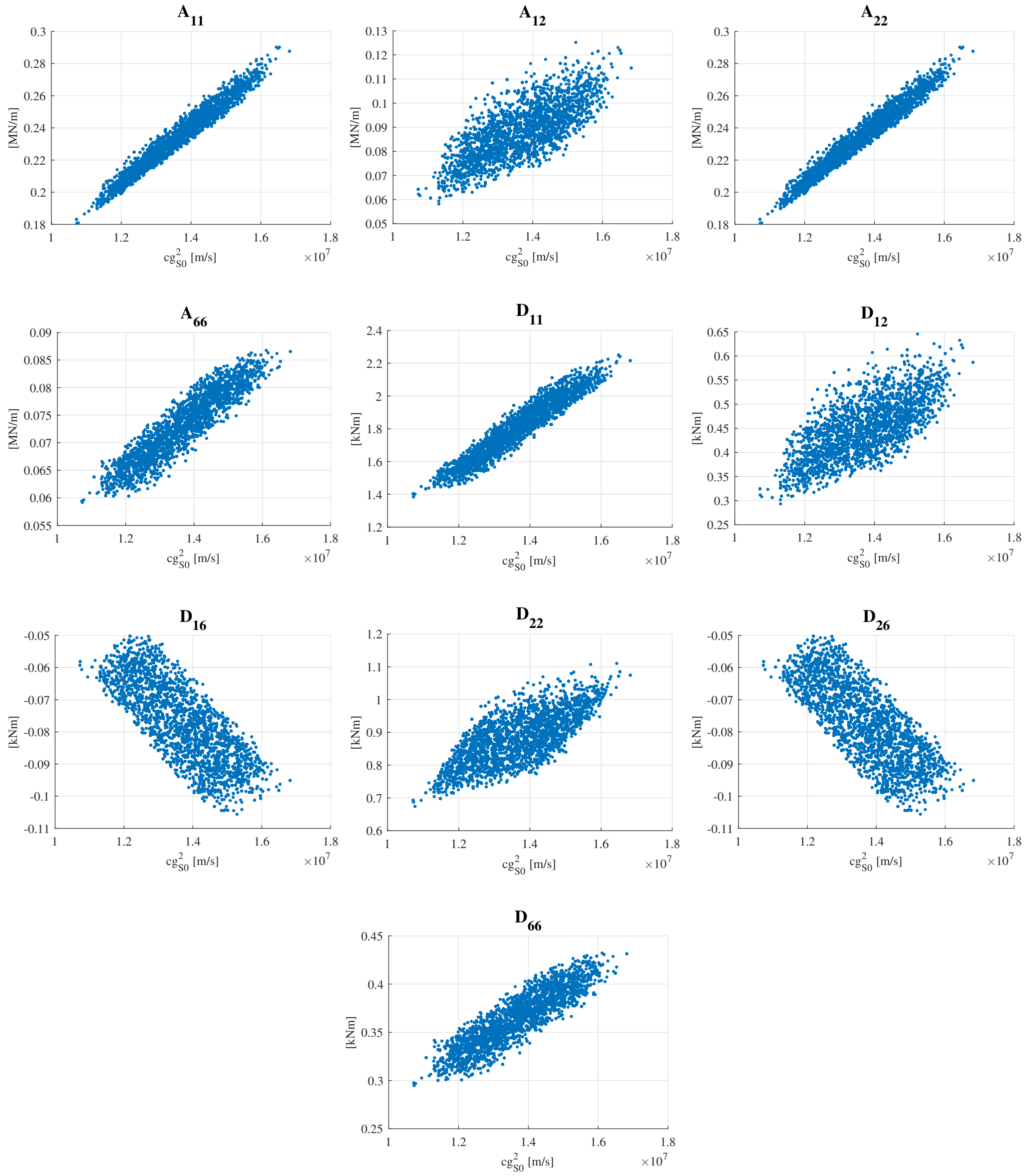

Figure 4.4: Correlation between the ABD-components and the squared S_0 group velocities included in the batch. The velocities correspond to S_0 waves propagating in the $0°$ direction at a frequency of 40 kHz.

$$\boldsymbol{C}\{\boldsymbol{ABD}\}^{\mathrm{T}} = \{\boldsymbol{c_g^2}\} \quad \text{(Ref. 3.14)}$$

$$\boldsymbol{C}\left(\{\boldsymbol{ABD}\} \odot \{\boldsymbol{1/ABD_{max}}\}\right)^{\mathrm{T}} = \{\boldsymbol{c_g^2}\} \quad (4.9)$$

Combining all these variations results in a total of 12 variants on the original methodology. These variants are summarized in table 4.5, in which the last two columns give the equation used to describe the relation between the ABD-components and the wave velocity, and the equation used to calculate the coupling coefficients.

Table 4.5: Variants on the methodology.

Variant	Group	Normalized	ABD	Eq.	Variant	Group	Normalized	ABD	Eq.
1	All	No	A	4.4 & 3.14	7	All	Yes	D	4.5 & 4.9
2	Diagonal	No	A	4.6 & 3.14	8	Diagonal	Yes	D	4.7 & 4.9
3	All	Yes	A	4.4 & 4.9	9	All	No	AD	4.2 & 3.14
4	Diagonal	Yes	A	4.6 & 4.9	10	Diagonal	No	AD	4.3 & 3.14
5	All	No	D	4.5 & 3.14	11	All	Yes	AD	4.2 & 4.9
6	Diagonal	No	D	4.7 & 3.14	12	Diagonal	Yes	AD	4.3 & 4.9

4.2.3. Procedure

In order to answer the defined questions of Section 4.1, a general procedure is applied to each part of the numerical feasibility study. For each scenario a total of 50 test cases is performed. The sample plate for each test case is arbitrarily chosen within the range of possible stiffness properties corresponding to the scenario. Velocity vector $\{\boldsymbol{c_g}^2\}$ is simulated using the SAFE method and used as input for the methodology, see equation 3.14. Eventually, to judge the accuracy of the methodology, the approximated ABD-components ($\boldsymbol{ABD_{cc_n}}$) are compared with the results according to the CLT method ($\boldsymbol{ABD_{CLT_n}}$). Here, the average error of the 50 test cases is used, calculated using equation 4.10. This procedure is schematically described in figure 4.5.

$$\text{Error} = \frac{\sum_{n=1}^{50} \frac{\boldsymbol{ABD_{cc_n}}}{\boldsymbol{ABD_{CLT_n}}} \cdot 100\%}{50} \tag{4.10}$$

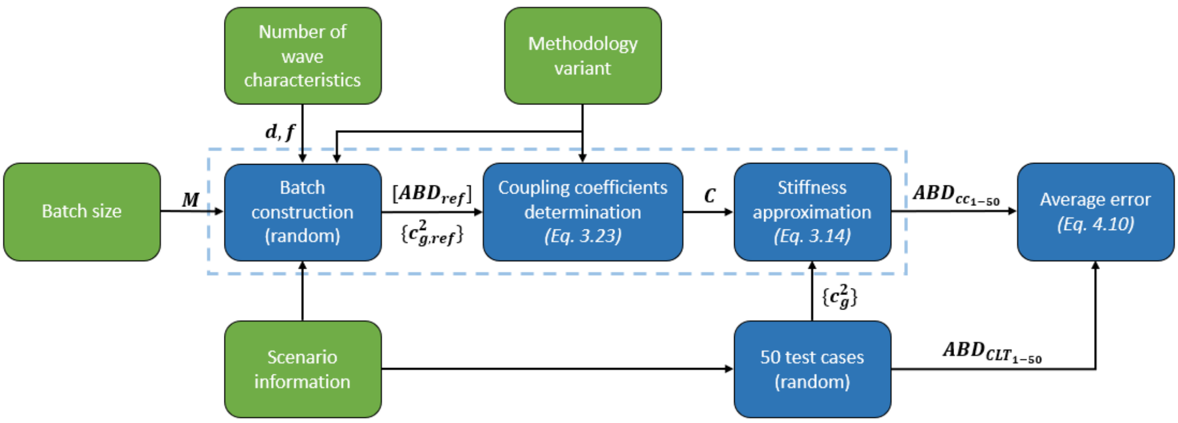

Figure 4.5: Schematic of the procedure used to determine the accuracy of the stiffness approximation by the developed methodology. The different parts of the developed methodology are captured in the blue dashed box. The system configurations are colored green.

4.3. Results

In this section, the results of the numerical feasibility study are presented. The results consist of three parts. First, the results of the convergence study with respect to the batch size for each scenario are discussed. Thereafter, the effect of the inclusion of the wave characteristics on the accuracy is shown. Lastly, the different variants on the methodology and the accuracy each variant can obtain is examined. For the sake of understanding, for the first two parts, the equations of variants 1 and 5 are applied to calculate the A-components and the D-components, respectively. Additionally, for the first and third parts, the wave propagation velocity at three frequencies ($\omega_j = 40$, 50, and 60 kHz), along five directions ($\theta_i = 0°$, 30°, 45°, 60°, and 90°), is used as the default input for the methodology.

4.3.1. Part 1: Convergence study on the batch size

For each scenario, a convergence study is performed with respect to the batch size. The goal is to verify whether the system converges and at what batch size this convergence occurs. It should be noted that for this first part the error (percentage difference from the CLT results, calculated using equation 4.10) at which the system converges is not of importance. A schematic of the applied procedure is given in figure 4.6. In this figure, the different parts of the developed methodology are captured in the blue dashed box. The system configurations are colored green.

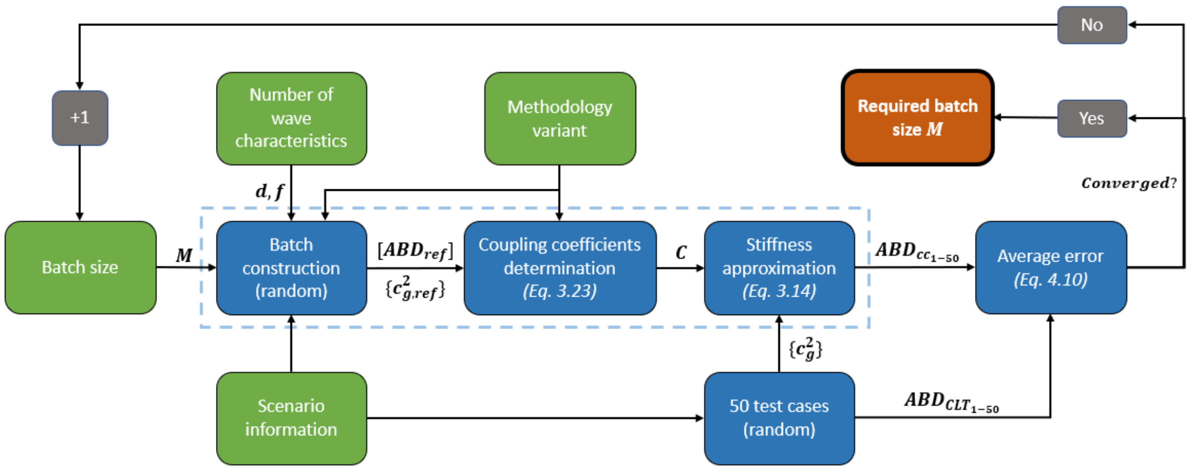

Figure 4.6: Schematic of the procedure used in the convergence study on the batch size. The different parts of the developed methodology are captured in the blue dashed box. The system configurations are colored green. The system is considered converged when the average error of the 50 test cases is constant with respect to the batch size.

Scenario 1

In figure 4.7 the results for scenario **1** are shown. In this figure, the A-components are indicated with a solid line and the D-components with a dashed line. The components A_{11} and D_{16} overlap exactly with A_{22} and D_{26}, respectively, and are therefore not visible.

It can be observed that the error (and thus the approximation) of all D-components converges quite fast and can be considered constant from a batch size of 200 reference laminates on. The components A_{11} and A_{22} also converge; however, this requires a larger batch size of approximately 1400 reference laminates. Lastly, an aggressive fluctuation pattern is observed for the components A_{12} and A_{66}. Eventually, around a batch size of 3500 reference laminates, the approximation of these components is also considered to be converged.

It can be concluded that for scenario **1** a batch size of 3500 reference laminates is sufficient to obtain converged results for all ABD-components.

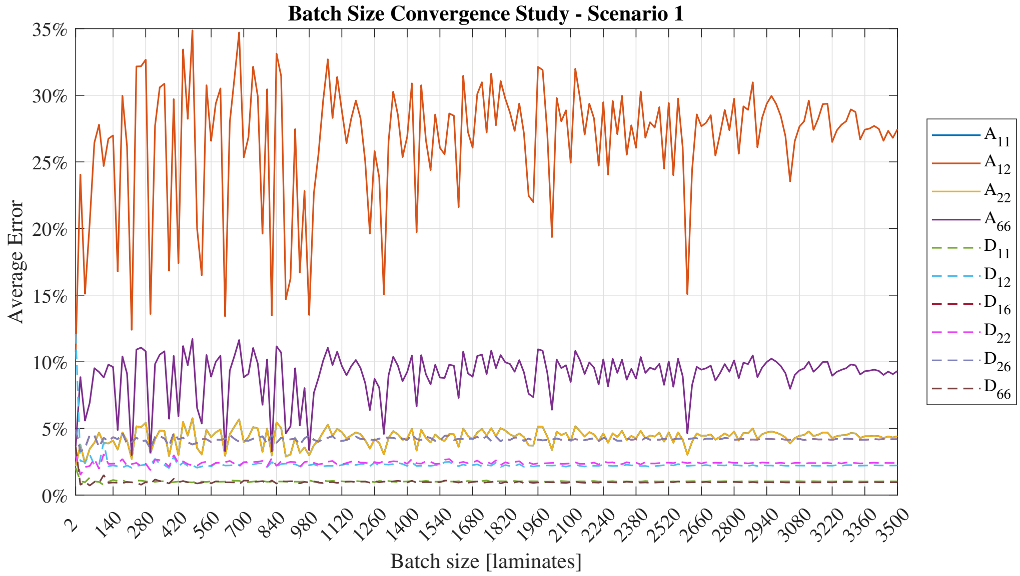

Figure 4.7: Convergence study with respect to the batch size for scenario **1**. The average error of 50 test cases compared to CLT is calculated using equation 4.10. Note that he components A_{11} and D_{16} overlap exactly with A_{22} and D_{26}, respectively, and are therefore not visible.

Scenario 2

The results of scenario **2** are plotted in figure 4.8. Stiffness components D_{16} and D_{26} are missing in the figure. This is because both components could not be approximated for several test case laminates, in part 3 an explanation for this lacking approximation will be given.

In contrast to scenario **1**, the results for the A-components converge fast and can be considered constant at a batch size of 80 reference laminates. The components D_{11} and D_{66} on the other hand show a fluctuating pattern and converge around a batch size of 1880 reference laminates. The D_{12}-component converges faster and is constant around 1220 reference laminates.

Similarly to scenario **1**, it can be concluded that the approximation of all stiffness components, except for D_{16} and D_{26}, converges and a batch size of 2000 reference laminates is sufficient.

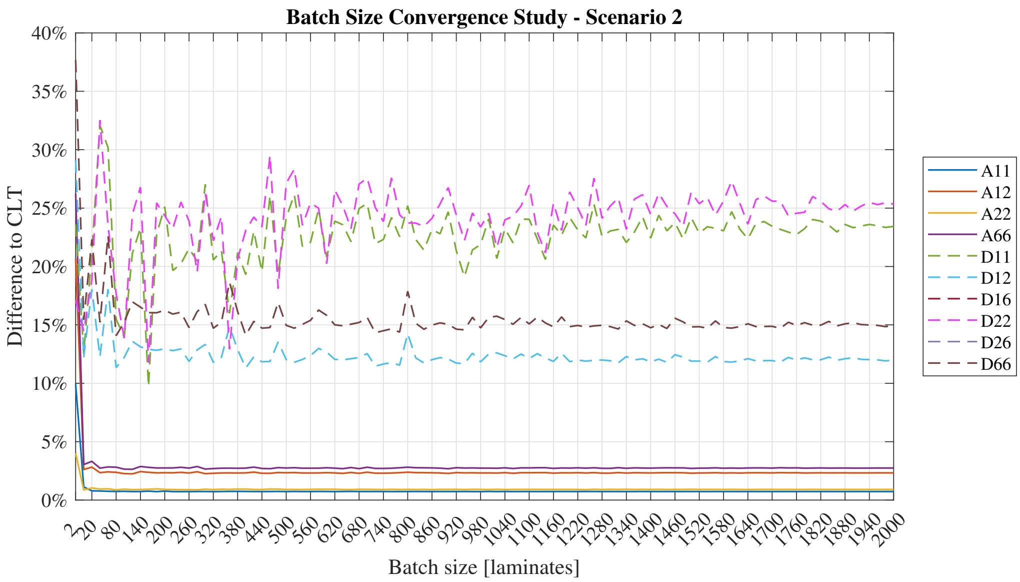

Figure 4.8: Convergence study with respect to the batch size for scenario **2**. The average error of 50 test cases compared to CLT is calculated using equation 4.10. Note that stiffness components D_{16} and D_{26} are missing in the figure.

Scenario 3

The results of scenario **3** are plotted in figure 4.9. Again, the stiffness components D_{16} and D_{26} are missing in the figure, for which an explanation is given in part 3.

The other components show a fluctuating pattern at low batch sizes, but are converging at increasing batch size. A batch size of 3500 reference laminates is considered sufficient to obtain converged results for all ABD-components for scenario **3**, with the exception of components D_{16} and D_{26}.

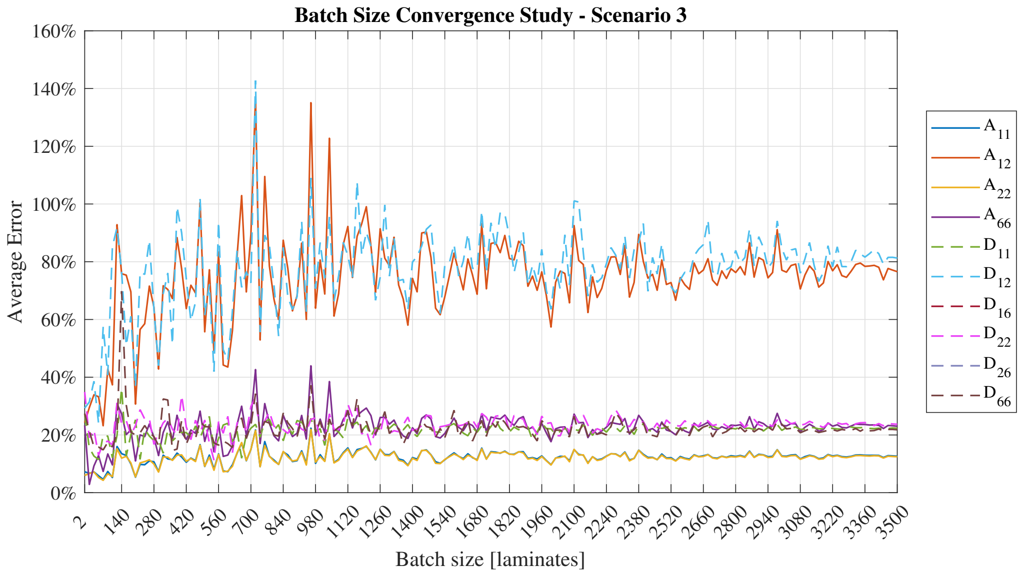

Figure 4.9: Convergence study with respect to the batch size for scenario **3**. The average error of 50 test cases compared to CLT is calculated using equation 4.10. Note that stiffness components D_{16} and D_{26} are missing in the figure.

4.3.2. Part 2: Convergence study on the inclusion of wave characteristics

In part 1, it was shown that for each scenario, the ABD-approximation converges when the batch, consisting of the reference laminates, is sufficiently large. In this second part, we examine the effect of the included wave characteristics on the accuracy of the methodology. In Chapter 3 it was stated that both the number of wave propagation directions (direction-dependent character) and the number of wave frequencies (dispersive character) define the inclusion of wave characteristics in the system. For this second part, the number of wave propagation directions (d) is taken constant, and only the effect of the included number of frequencies in the system is examined. The constant directions (θ_i) used are $0°$, $30°$, $45°$, $60°$, and $90°$.

Using the SAFE method the dispersion curves for the plate of interest (table 4.1) have been established, resulting in figure 4.10. The dispersion curves in the other directions are similar to those in the $0°$ directions. In the proposed methodology, the wave velocities of the S_0 and A_0 wave modes, at multiple frequencies and along multiple propagation directions are used. The range of usable frequencies is limited by two factors that are related to the experimental part. To make this feasibility study as realistic as possible, it is decided to take these limiting factors into account in this study as well. The limiting factors are formulated as:

1. The upper limit of usable frequencies is determined by the presence of higher-order wave modes, which, for this study, is considered undesirable for accurate velocity measurements of the two wave modes.
2. The lower limit is determined by the type of transducer used during the experiments; specifications of these transducers will be discussed in Chapter 5.

Furthermore, the level of attenuation of low-frequency waves is a limiting factor. To conclude, with regard to figure 4.10 and the transducer specifications, the usable frequency range is 20-80 kHz. For the current convergence study, the number of frequencies ranges from one to seven. The frequencies used for each step are listed in table 4.6. The frequencies are chosen in order to cover the frequency range of 20-80 kHz as equally as possible for each number of frequencies.

For each scenario, the effect of the included wave characteristics is discussed. Again, it should be remarked that, for this part, the error at which the system converges is not of importance. For this convergence study, the convergence based on the batch size is taken into account, and the results shown correspond to the approximation using the complete batch size. A schematic of the applied procedure for this second part is given in figure 4.11.

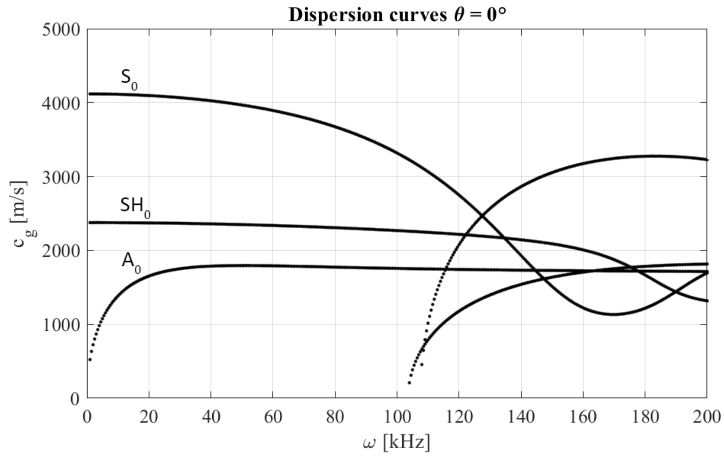

Figure 4.10: The simulated dispersion curves along the 0° direction corresponding to the plate of interest used in the feasibility study

Table 4.6: Overview of the frequencies used for each number of frequencies.

Total number of frequencies	ω_i [kHz]	Total number of frequencies	ω_i [kHz]
1	40	5	20 30 50 70 80
2	30 60	6	20 30 40 50 70 80
3	30 50 70	7	20 30 40 50 60 70 80
4	20 40 60 80		

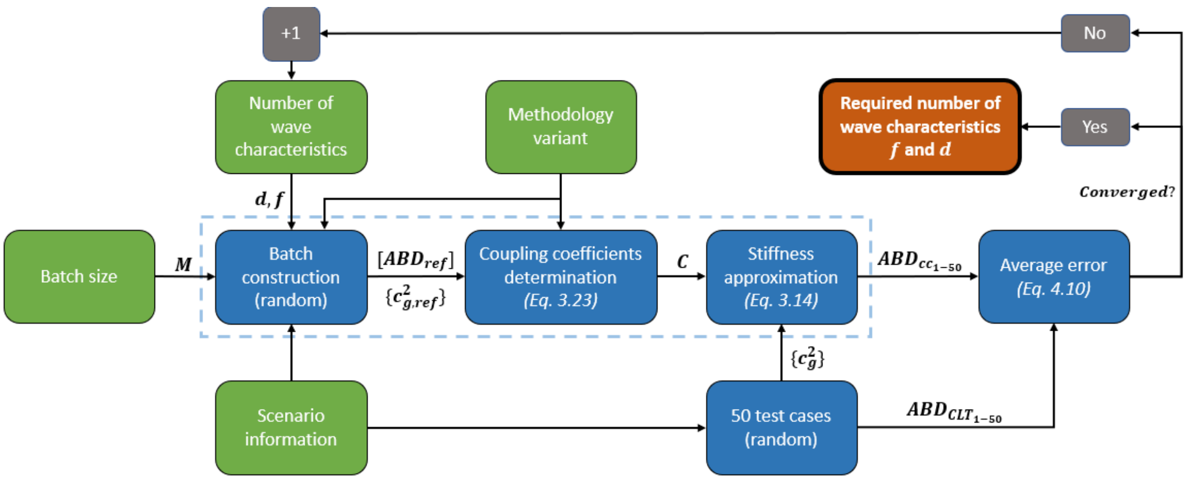

Figure 4.11: Schematic of the procedure used in the convergence study on the inclusion of wave characteristics. The different parts of the developed methodology are captured in the blue dashed box. The system configurations are colored green. The system is considered converged when the average error of the 50 test cases is constant with respect to the batch size.

Scenario 1

The result of the convergence study for scenario **1** is plotted in figure 4.12. Similarly to scenario **1** in part 1, the stiffness components A_{11} and D_{16} overlap exactly with A_{22} and D_{26}, respectively. Furthermore, the component D_{11} is hardly visible, since it is approximately equal to D_{66}.

It can be concluded that a minimal amount of two frequencies is required to obtain a converged approximation. Regarding components A_{12} and A_{66}, a total of three frequencies would even be more convenient.

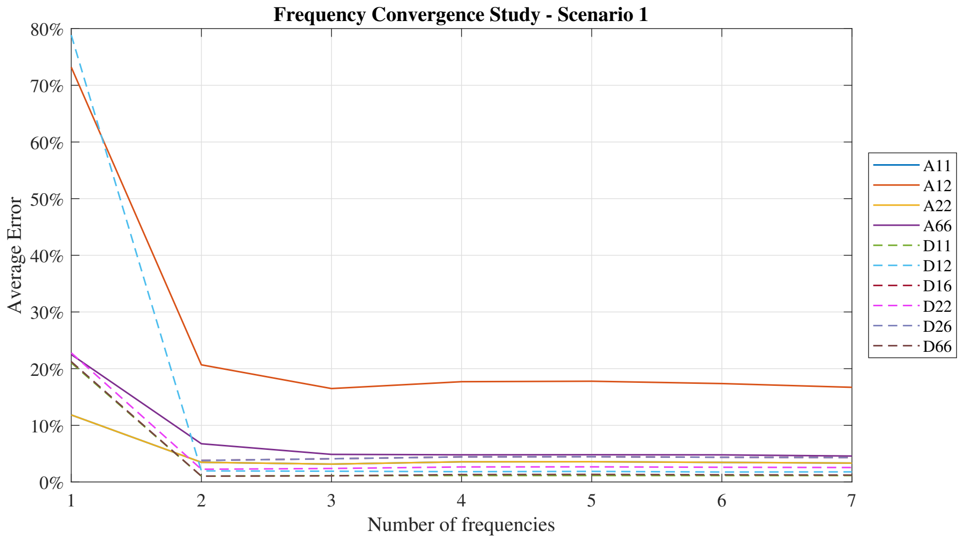

Figure 4.12: Convergence study on the inclusion of wave characteristics for scenario **1**. The difference compared to CLT is calculated using equation 4.10. Note that stiffness components A_{11} and D_{16} overlap exactly with A_{22} and D_{26}, respectively, and are therefore not visible.

Scenario 2

Figure 4.13 shows the results for scenario **2**. Again, stiffness components D_{16} and D_{26} are missing in the figure.

It can be concluded that there is hardly any change in error for the components A_{12}, A_{66}, D_{12}, and D_{66}. The results for the other components are considered to have converged at a total of three frequencies.

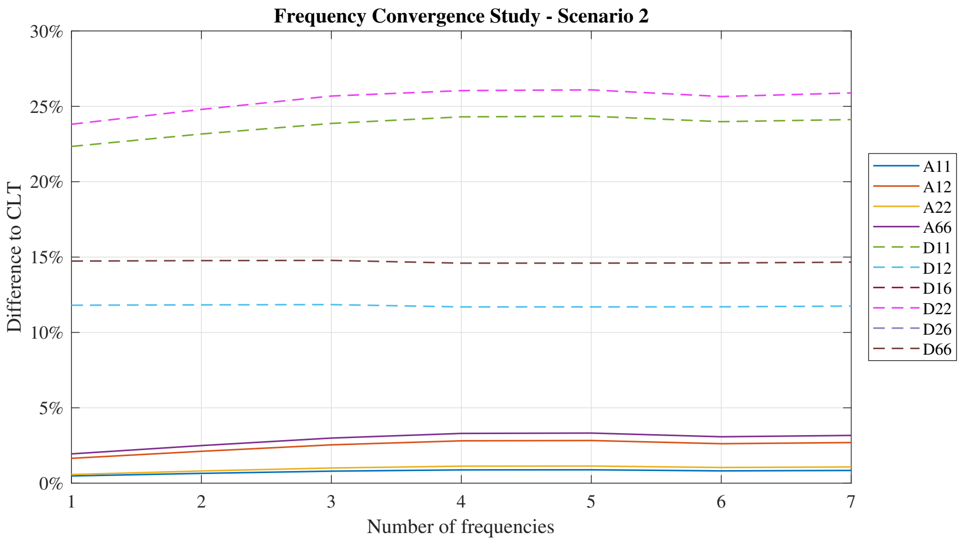

Figure 4.13: Convergence study on the inclusion of wave characteristics for scenario **2**. The difference compared to CLT is calculated using equation 4.10. Note that stiffness components D_{16} and D_{26} are missing in the figure.

Scenario 3

The results of the last scenario are plotted in figure 4.14, in which D_{16} and D_{26} are missing. The diagonal D-components are hardly influenced by the number of frequencies. The other components are more dependent on the number of frequencies and converge at a total of four frequencies.

Therefore, it is concluded that a total of four frequencies is required for the third scenario.

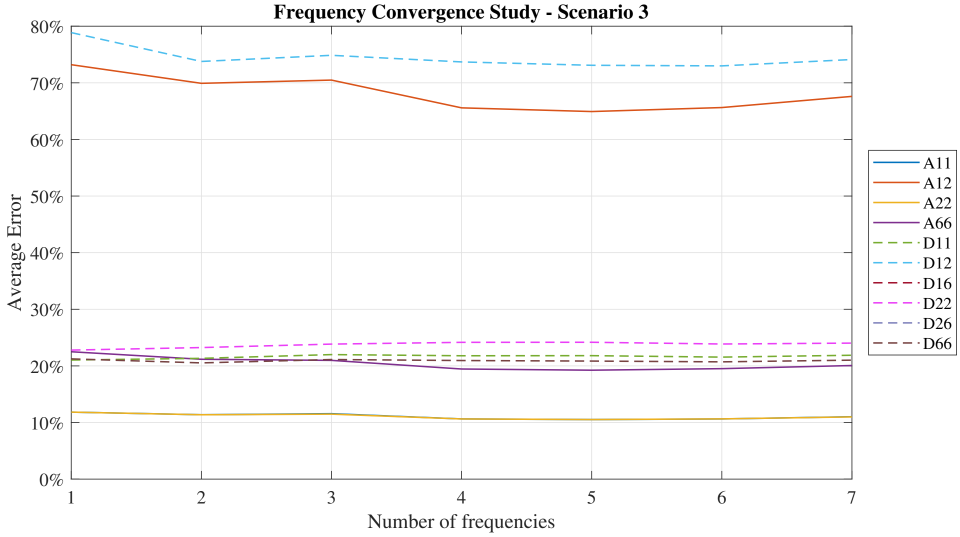

Figure 4.14: Convergence study on the inclusion of wave characteristics for scenario **3**. The difference compared to CLT is calculated using equation 4.10. Note that stiffness components D_{16} and D_{26} are missing in the figure.

Based on the convergence studies on the inclusion of wave characteristics, performed for each scenario, it is concluded that a total of three frequencies is convenient. Minor improvements on the error are observed when the total number of frequencies increases. However, it should be taken into account that a larger number of frequencies causes the calculation time to increase to (1) create the batch (matrix $[\boldsymbol{ABD_{ref}}]$ and vector $\{\boldsymbol{c_{g,ref}}^2\}$) and (2) approximate the ABD-components. For the sake of in-situ applicability, these long calculation times are undesirable.

4.3.3. Part 3: Accuracy of the variants on the methodology

In the previous two parts, the convergence of the methodology has been established as a function of the batch size and the included wave characteristics. With this information, the developed variants on the methodology, discussed in Section 4.2.2 and summarized in table 4.5, are examined.

For each scenario, the ABD-components are approximated using all 12 variants. The complete scenario-dependent batch of reference laminates is used for each approximation. Furthermore, three wave frequencies ω_f are used; 40, 50, and 60 kHz. A schematic of the procedure applied for this third part is given in figure 4.5. Here, the batch size (M) and the number of wave characteristics (d) and (f) correspond to the results obtained from parts 1 and 2, respectively.

Scenario 1

The results of scenario **1** are shown in table 4.7. The results of variants 1-4 show no differences and, except for A_{12}, all results are good. Variants 5-6 show small differences, but can also all be considered good. Variants 9 and 12 cannot approximate the D-components. The errors obtained are greater than $1 \cdot 10^9\%$ and are indicated by $\gg 100$ in the table. The best results are obtained by variant 11 which approximates the ABD-components using the original formulated relation for symmetric laminates (equation 4.2) in combination with the normalized coupling coefficients (equation 4.9).

It can be concluded that the methodology is very well able to approximate the ABD-components for the first scenario. Furthermore, it can be concluded that normalization of the coupling coefficients has a great impact on the results for variants 9 and 11.

Table 4.7: Accuracy of the ABD-approximations using the 12 variants on the methodology for scenario **1**. The accuracy is expressed as the average error compared to the CLT results, calculated using equation 4.10.

Variation	Group	Normalized	ABD	A_{11} [%]	A_{12} [%]	A_{22} [%]	A_{66} [%]	D_{11} [%]	D_{12} [%]	D_{16} [%]	D_{22} [%]	D_{26} [%]	D_{66} [%]
1	All	No	A	3.88	24.67	3.88	8.35						
2	Diagonal	No	A	3.88		3.88	8.35						
3	All	Yes	A	3.88	24.66	3.88	8.35						
4	Diagonal	Yes	A	3.88		3.88	8.35						
5	All	No	D					0.97	2.66	3.56	2.13	3.56	0.95
6	Diagonal	No	D					0.95			5.03		2.83
7	All	Yes	D					0.97	2.66	3.56	2.13	3.56	0.95
8	Diagonal	Yes	D					0.95			5.03		2.83
9	All	No	AD	2.64	13.00	2.64	4.42	$\gg 100$	$\gg 100$	$\gg 100$	$\gg 100$	$\gg 100$	$\gg 100$
10	Diagonal	No	AD	0.47		0.47	0.86	0.97			2.13		0.95
11	All	Yes	AD	0.47	2.33	0.47	0.87	0.97	2.66	3.56	2.13	3.56	0.95
12	Diagonal	Yes	AD	2.62		2.62	3.73	$\gg 100$			$\gg 100$		$\gg 100$

Scenario 2

Table 4.8 shows the results for the second test scenario. Similarly to the first scenario, there are minimal differences between variants 1-4 and between variants 5-8. The A-components can be approximated with good accuracy, but the results of the D-components are not reliable. According to the results, the difference between the components D_{16} and D_{26} compared to the CLT results is infinite. However, it should be taken into account that this infinite difference is the average accuracy of 50 test cases. Two of these randomly selected test cases turned out to be cross-ply laminates for which D_{16} and D_{26} are known to be zero [2]. This means that $\boldsymbol{ABD_{cc_n}}$ in equation 4.10 is divided by zero. The approximated stiffness values $\boldsymbol{ABD_{cc_n}}$ are not exactly zero and therefore cause an infinite difference. When both cross-ply test cases are excluded from the averaged result, there is still an error of ±150% for both D_{16} and D_{26}.

It can be concluded that variant 11 provides the best results for the second scenario; however, these are worse than for scenario **1**. The A-components can be approximated very well, D_{11}, $D12$, D_{22}, and D_{66} are reasonably approximated, and D_{16} and D_{26} cannot be approximated using the methodology.

Table 4.8: Accuracy of the ABD-approximation using the 12 variants on the methodology for scenario **2**. The accuracy is expressed as the average error compared to the CLT results, calculated using equation 4.10.

Variation	Group	Normalized	ABD	A_{11} [%]	A_{12} [%]	A_{22} [%]	A_{66} [%]	D_{11} [%]	D_{12} [%]	D_{16} [%]	D_{22} [%]	D_{26} [%]	D_{66} [%]
1	All	No	A	0.73	2.33	0.91	2.75						
2	Diagonal	No	A	0.73		0.91	2.75						
3	All	Yes	A	0.73	2.33	0.91	2.75						
4	Diagonal	Yes	A	0.73		0.91	2.75						
5	All	No	D					23.44	12.00	∞	25.35	∞	14.95
6	Diagonal	No	D					22.18			25.20		16.34
7	All	Yes	D					23.44	12.00	∞	25.35	∞	14.95
8	Diagonal	Yes	D					22.18			25.20		16.34
9	All	No	AD	0.83	2.33	0.91	2.75	11.22	13.17	∞	11.43	∞	16.67
10	Diagonal	No	AD	0.73		0.91	2.75	11.40			11.88		19.39
11	All	Yes	AD	0.94	1.44	0.66	1.66	9.31	13.12	∞	9.99	∞	16.60
12	Diagonal	Yes	AD	0.93		0.90	1.72	16.25			11.30		31.70

Scenario 3

Lastly, for scenario **3** the results of the different variants are shown in table 4.9. Unlike the first two scenarios, greater errors are observed between variants 1-4. Variants 2 and 4 show good results for the diagonal A-components. The results obtained using variants 4-8 are inaccurate. Similarly to the second scenario, none of the variants is able to obtain a logical approximation for D_{16} and D_{26}, again this can be explained by the presence of two cross-ply laminate test cases. Excluding these test cases still results in an average error of ±180%.

Overall, it can be concluded that for the third scenario, it is only possible to approximate the diagonal stiffness components with a reasonable to good accuracy. The best results are obtained by variant 12 which approximates the ABD-components using the diagonal formulated relation (equation 4.3) in combination with the normalized coupling coefficients (equation 4.8). The off-diagonal components cannot be approximated for this scenario.

Table 4.9: Accuracy of the ABD-approximation using the 12 variants on the methodology for scenario **3**. The accuracy is expressed as the average error compared to the CLT results, calculated using equation 4.10.

Variation	Group	Normalized	ABD	A_{11} [%]	A_{12} [%]	A_{22} [%]	A_{66} [%]	D_{11} [%]	D_{12} [%]	D_{16} [%]	D_{22} [%]	D_{26} [%]	D_{66} [%]
1	All	No	A	12.65	76.57	12.45	23.01						
2	Diagonal	No	A	1.69		1.81	2.90						
3	All	Yes	A	12.65	76.57	12.45	23.01						
4	Diagonal	Yes	A	1.69		1.81	2.90						
5	All	No	D					22.30	81.28	∞	23.71	∞	21.79
6	Diagonal	No	D					20.11			20.90		15.32
7	All	Yes	D					22.30	81.28	∞	23.71	∞	21.79
8	Diagonal	Yes	D					20.12			20.90		15.32
9	All	No	AD	11.27	69.09	11.20	21.58	$\gg 100$	$\gg 100$	∞	$\gg 100$	∞	$\gg 100$
10	Diagonal	No	AD	2.14		2.07	5.02	25.56			24.04		87.02
11	All	Yes	AD	8.89	60.56	9.34	18.22	12.38	83.64	∞	14.05	∞	37.77
12	Diagonal	Yes	AD	1.69		1.81	2.90	12.56			13.76		15.74

4.4. Conclusion

In this chapter the potential of the developed methodology is examined using a numerical feasibility study. This feasibility study is carried out by assuming three test scenarios that all have a different amount and type of available structural information. Furthermore, several variants on the original methodology, discussed in Chapter 3, are developed and examined. The results of the feasibility study consisted of three parts; (1) a convergence study on the batch size, (2) a convergence study on the inclusion of wave characteristics, and (3) a comparison of the approximation accuracy obtained by each variant of the methodology.

The following conclusions can be drawn regarding the numerical feasibility study:

All scenarios

- A total of 30 wave characteristics included in the system is sufficient to obtain converged approximations, while still allowing the possibility of in-situ applicability for the sake of reasonable calculation times. These characteristics consist of wave velocities of the S_0 and A_0 wave modes measured along five propagation directions at three wave frequencies.

Scenario 1

In the situation of unknown exact properties of the laminae, which are known to be within a certain range of 80-120%:

- A batch size of 3500 reference laminates is sufficient to obtain converged approximations for all the ABD-components.
- The best results are obtained using the original relation between all the stiffness components and wave velocities in combination with the normalized coupling coefficients. The accuracies, expressed as error compared to CLT, averaged over 50 test cases, are given in table 4.10.

Table 4.10: The average errors compared to CLT, obtained for scenario **1**. The stiffness is approximated using equations 4.2 and 4.9. The accuracy is expressed as the average error compared to the CLT results, calculated using equation 4.10.

	A_{11}	A_{12}	A_{22}	A_{66}	D_{11}	D_{12}	D_{16}	D_{22}	D_{26}	D_{66}
Error [%]	0.47	2.33	0.47	0.87	0.97	2.66	3.56	2.13	3.56	0.95

.

Scenario 2
In the situation of an unknown stacking sequence, which is known to consist of just 0°, ±30°, ±45°, ±60°, and / or 90° plies:

- A batch size of 2000 reference laminates is sufficient to obtain converged approximations for all the ABD-components, with the exception of the components D_{16} and D_{26}.
- The best results are obtained using the original relation between all the stiffness components and the wave velocity in combination with the normalized coupling coefficients. The accuracies, expressed as error compared to CLT, averaged over 50 test cases, are given in table 4.11.

Table 4.11: The average errors compared to CLT, obtained for scenario **2**. The stiffness ia approximated using equations 4.2 and 4.9. The accuracy is expressed as the average error compared to the CLT results, calculated using equation 4.10.

	A_{11}	A_{12}	A_{22}	A_{66}	D_{11}	D_{12}	D_{16}	D_{22}	D_{26}	D_{66}
Error [%]	0.94	1.44	0.66	1.66	9.31	13.12	∞	9.99	∞	16.60

Scenario 3
In the situation of unknown properties of the laminae, which are known to be within a certain range of 80-120%, and an unknown stacking sequence, which is known to consist of just 0°, ±30°, ±45°, ±60°, and / or 90° plies:

- A batch size of 3500 reference laminates is sufficient to obtain converged approximations for all the ABD-components, with the exception of the components D_{16} and D_{26}.
- The best results are obtained using the relation between the diagonal stiffness components and the wave velocity in combination with the normalized coupling coefficients. The off-diagonal stiffness components cannot be approximated with reasonable accuracy. The accuracies, expressed as error compared to CLT, averaged over 50 test cases, are given in table 4.12.

Table 4.12: The average errors compared to CLT, obtained for scenario **3**. The stiffness is approximated using equations 4.3 and 4.9. The accuracy is expressed as the average error compared to the CLT results, calculated using equation 4.10.

	A_{11}	A_{12}	A_{22}	A_{66}	D_{11}	D_{12}	D_{16}	D_{22}	D_{26}	D_{66}
Error [%]	1.69	60.56	1.81	2.90	12.56	83.64	∞	13.76	∞	15.74

5
Experiments

In the previous chapter, a numerical feasibility study was carried out. In that study, a better understanding of the two numerical accuracy factors, the inclusion of wave characteristics and the determination of the coupling coefficients, was derived. The third factor related to the accuracy of the methodology was described in Chapter 3 and is the accuracy of the experimental data used as input to the system. In order to conclude about this third accuracy factor, the methodology developed is applied in an experimental setting to assess the stiffness properties of a sample FRC plate. This chapter discusses the applied experimental procedure used to collect accurate experimental data.

In Section 5.1 the specifications of the sample plate used for the experiments are described. Thereafter, the experimental setup and the diagnostic wave signal specifications are described in Section 5.2. Lastly, in Section 5.3, the applied signal processing procedure and calculation of the wave velocities is described.

5.1. Plate specifications

In previous research bij Zaal [77], a balanced and symmetric glass-fiber reinforced composite plate was produced. The composite manufacturing process used during production was vacuum infusion. The specifications of the components used are given in table 5.1. The general properties of the plate are given in table 5.2. Specifications on the stacking sequence are provided in table 5.3. In table 5.4, the stiffness properties of the laminae are given. These properties are also the properties that are used for the numerical feasibility study, given in table 4.1. Note that the properties in table 5.4 are provided by the manufacturer and cannot be assumed to be the exact stiffness properties.

Table 5.1: Material components used.

Component	Name	V_f/V_m
Fiber	Seartex U-E-640g/m^2	48%
Resin	Altec E-Nova MA 6215	52%
Hardener	Curox CM-75	-

Table 5.2: General plate properties.

Width $[mm]$	Length $[mm]$	ρ_{resin} $[kg/m^2]$	ρ_{fiber} $[kg/m^2]$	ρ_{overall} $[kg/m^2]$	Fiber type [-]	t_{total} $[mm]$
600	600	1200	2600	1872	UD 600	8.16

Table 5.3: Stacking sequence properties.

Number of plies [-]	lay-up [°]	t_{ply} $[mm]$	Specifications [-]
16	$[0_2/45_2/-45_2/90_2]S$	0.51	symmetric balanced

Table 5.4: Stiffness properties of the laminae, provided by manufacturing.

E_1 $[GPa]$	$E_2 = E_3$ $[GPa]$	$G_{12} = G_{13}$ $[GPa]$	G_{23} $[GPa]$	$\nu_{12} = \nu_{13}$ [-]	ν_{23} [-]
46.2	13.1	4.1	5.1	0.29	0.28

5.2. Experimental setup

An overview of the experimental setup is provided in figure 5.1. Each component of the setup has been given a number in the direction equal to the path taken by the signal. A schematic of the setup with the corresponding numbering is given in figure 5.2. For further explanation, the setup is divided to two parts; (1) the signal transmitting part, consisting of components 1-3, and (2) the signal recording part, consisting of components 4-7. For each part, further elaboration is given below.

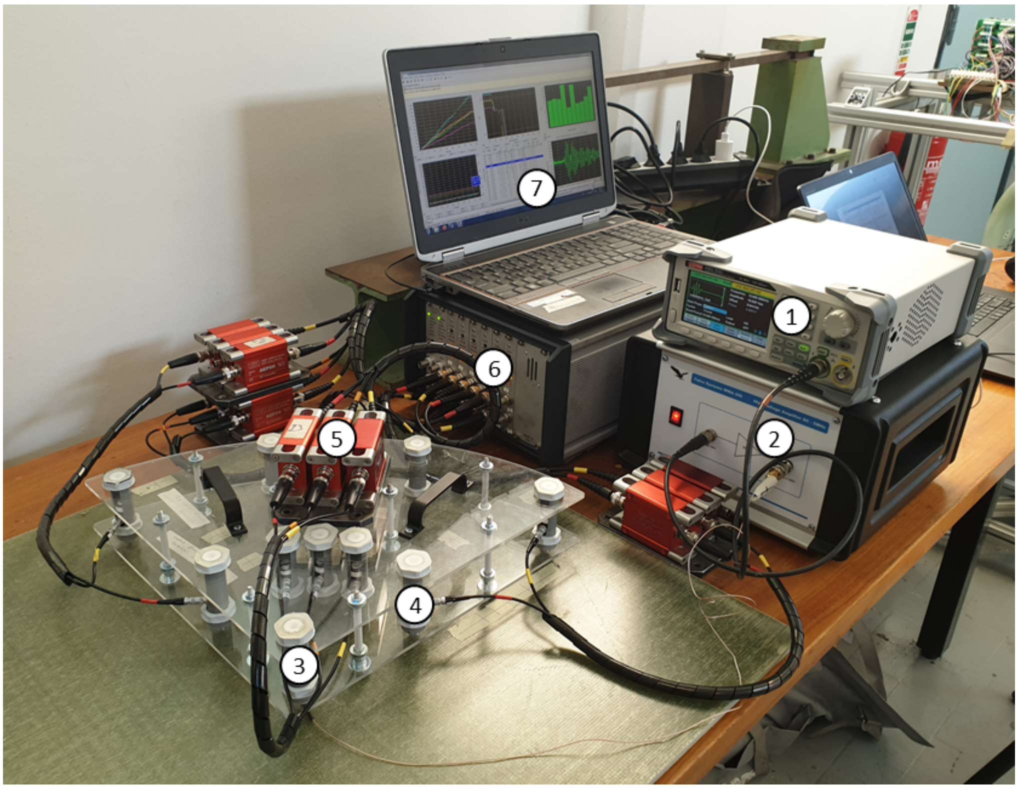

Figure 5.1: Overview of the experimental setup including the (1) wave generator, (2) high voltage amplifier, (3) actuator, (4) Dry Point Contact (DPC) transducer, (5) pre-amplifier, (6) data acquisition system, and (7) acquisition software.

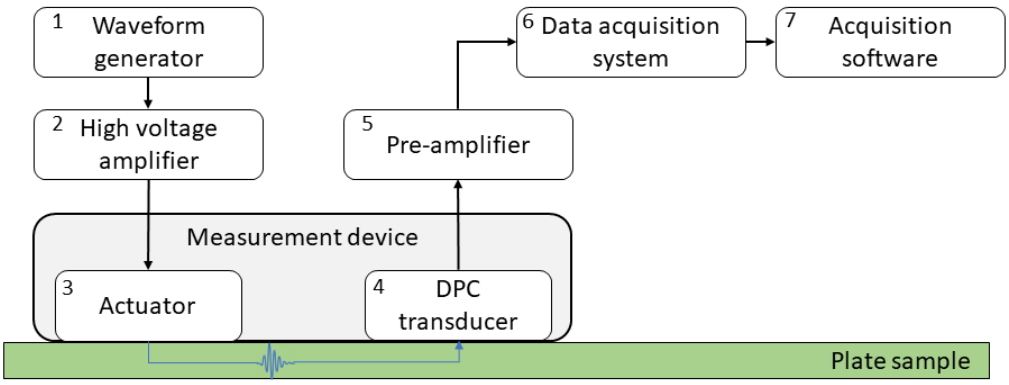

Figure 5.2: Schematic overview of the experimental setup.

5.2.1. The signal transmitting components

The signal transmitting part of the experimental setup generates a diagnostic wave signal using the waveform generator and emits it through the actuator. In between, a high-voltage amplifier is incorporated, which amplifies the voltage of the generated electrical waveform. The waveform generator used is the RS PRO RSDG1032X [78], shown in figure 5.3a. This waveform generator is connected to a WMA-300 high-voltage amplifier developed by Falco systems [79], shown in figure 5.3b. Thereafter, the electrical waveform is converted into a mechanical wave through a piezoelectric transducer, indicated as the actuator in figure 5.2. The type of transducer used is the VS600-Z1, designed by Vallen [80], shown in figure 5.3c.

(a) The RS PRO RSDG1032X waveform generator.

(b) The WMA-300 high voltage amplifier [79].

(c) The VS600-Z1 actuator [80].

Figure 5.3: The signal-transmitting components of the experimental setup.

5.2.2. The signal recording components

After propagation of the signal through the sample plate, it arrives at the DPC transducer. From here, the signal is recorded, amplified, and processed. The recording transducers used are Dry Point Contact (DPC) transducers of type S1803 produced by ACS Group [81], shown in figure 5.4a. The recorded signal is amplified using pre-amplifiers of type AEPH5, designed by Vallen Systeme [82], and shown in figure 5.4b. Subsequently, the amplified signal is loaded into the AMSY-6 data acquisition system (DAS), designed by Vallen Systeme [83] as well. Both the MB6 and the MB19 chassis types are used for the measurements, depending on availability, the MB6 type is shown in figure 5.4c.

(a) The S1803 Dry Point Contact transducer [81].

(b) The WMA-300 high voltage amplifier [79].

(c) The AMSY-6 data acquisition system chassis type MB6 [83].

Figure 5.4: The signal-recording components of the experimental setup.

5.2.3. Measurement device

In the methodology developed, the input data required consist of wave velocities along five propagation directions. To comply with this requirement, a measurement device has been developed that is capable of measuring wave signals in five directions simultaneously. Several pictures of the measuring device are given in figure 5.5. The wave-emitting actuator is located on the bottom left in figure 5.5a and 5.5b, and in the position most left in Fig. 5.5c. The emitted diagnostic signal propagates in all planar directions around the actuator. To derive the wave velocity, the arrival time of the signal at two locations has to be derived. Therefore, ten transducers are located in pairs of two in each direction around the actuator, this is clearly visible in figure 5.5b. Similarly to the feasibility study, the propagation directions used are $0°, 30°, 45°, 60°$ and $90°$. More details about the wave velocity calculations are given in Section 5.3.

The transducers are each located in a holder. To ensure that measurements can be performed on surfaces with minor bumps, these transducer holders are equipped with a spring. In figure 5.6 a close-up of one of the DPC transducer holders is given. The holder consists of a PVC tube in which the transducer can move freely in the upward direction but is confined in the planar directions with respect to the surface. The spring on top of the transducers ensures that the transducers are in contact with the surface. In between the transducer holders, several feet have been placed, as can be clearly seen in figure 5.5c. These feet ensure that approximately the same pressure is applied to each transducer, which contributes to the quality of the measured signal. A similar transducer holder is used for the actuator. A close-up of this holder is given in figure 8.1. In this holder, a replica of the DPC transducer is made of wood; on this replica, the VS600-Z1 actuator is glued.

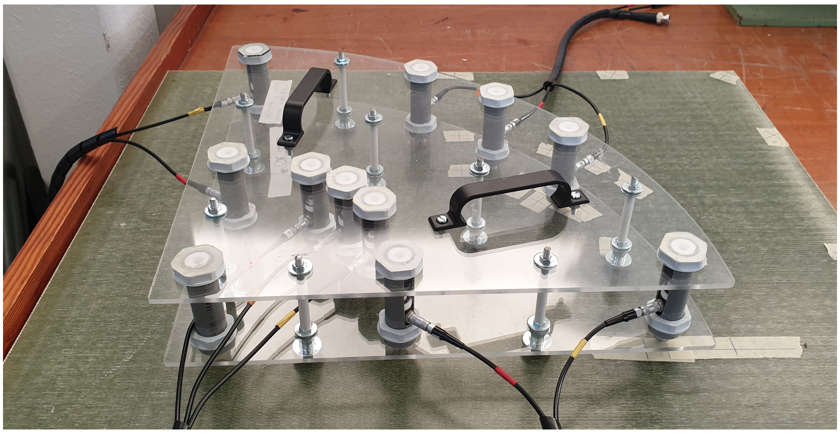

(a) The measurement device including the actuator located at the bottom left and ten DPC transducers aligned in pairs along each direction with respect to the actuator. Two black handles are placed on top of the device.

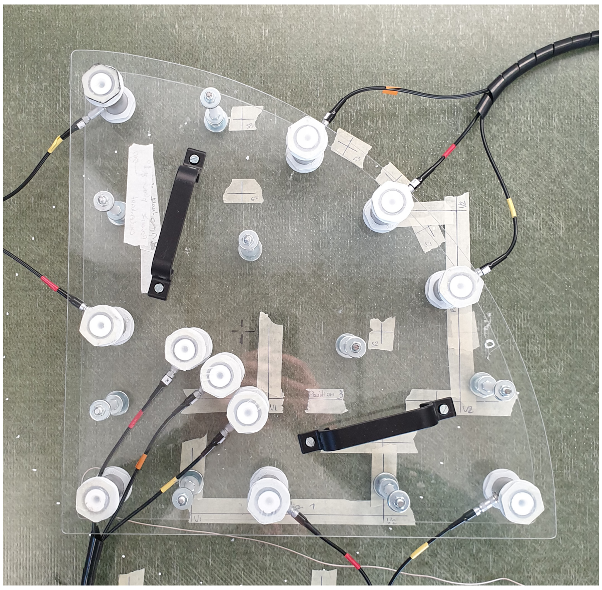

(b) Top view of the measurement device.

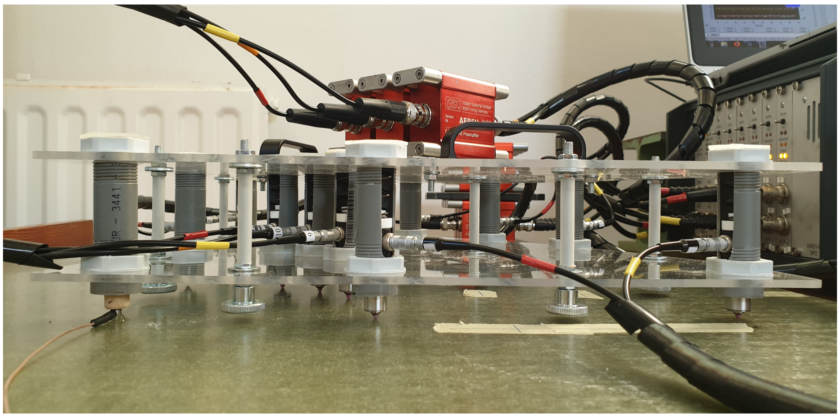

(c) Side view of the measurement device. Note that, due to the springs included in the transducer holders, the actuator and the DPC transducers only make contact with the surface when pressure is applied on top of the device. Pressure can be applied until the steel feet, located between the transducer holders, make contact with the surface.

Figure 5.5: The measurement device

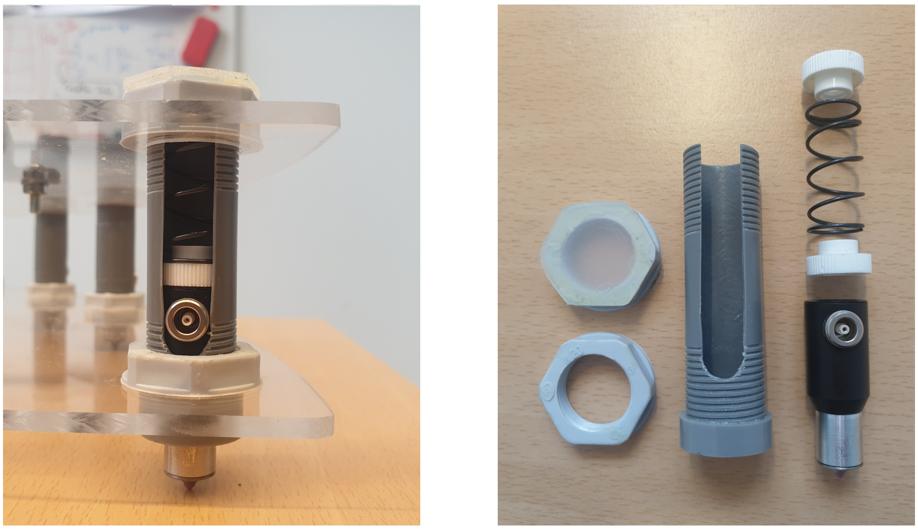

(a) Close up of one of the the DPC transducer holders.

(b) The disassembled transducer holder including the transducer, spring and screws.

Figure 5.6: Detailed view of a DPC transducer holder.

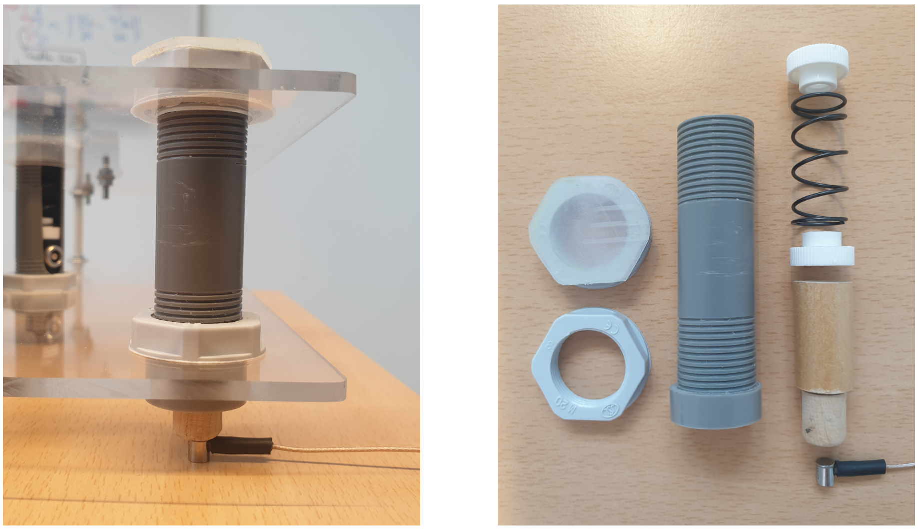

(a) Close up of the actuator holder.

(b) The disassembled actuator holder including the VS600 actuator, replica of the DPC transducer, spring and screws.

Figure 5.7: Detailed view of the actuator holder.

5.2.4. Settings

In this section, the settings used for both the waveform generator and the data acquisition system are briefly discussed.

Waveform generator

The multi-modal and dispersive behavior of UGW comes with certain challenges in the calculation of travel time. For example, reflections from structural discontinuities and edges may overlap with the diagnostic waveform and complicate the computation of travel times. Therefore, separate envelopes containing the diagnostic waveform and its reflections are a desirable feature. This can be achieved by using narrow-band pulse signals. Here, narrow-banded refers to signals that are narrow in the frequency domain. When the different frequencies included in the signal lie within a narrow range, they propagate at nearly equal phase speeds. Therefore, the envelope of the diagnostic waveform does not change with time. Minimizing this dispersion of signals can improve the robustness and accuracy of signal processing for the arrival time picking of diagnostic waves [84]. The diagnostic waveforms used in this study are narrow-banded Hanning-windowed sinusoidal pulses defined by Pahlavan [84].

As concluded in the feasibility study, a total of three wave frequencies is sufficient for the methodology. Therefore, three waveforms are used, all of which have a different center frequency ω_c. Unlike the numerical feasibility study, 50, 60 and 70 kHz are the center frequencies of the diagnostic signals used during the experiments. The center frequency of 70 kHz has been chosen over the 40 kHz signal of the numerical feasibility study because it was experienced that the different wave modes can be better distinguished at higher frequencies. Other details about the diagnostic waveform generated by the waveform generator are listed in table 5.5. The resulting diagnostic burst signals are shown in figure 5.12.

Table 5.5: Settings of the diagnostic waveforms.

Freqyency	Number of pulses	Amplitude	Burst period	Signal period
[kHz]	[-]	[V_{pp}]	[s]	[μs]
50	5	10	1	100.2
60	5	10	1	83.5
70	5	10	1	71.6

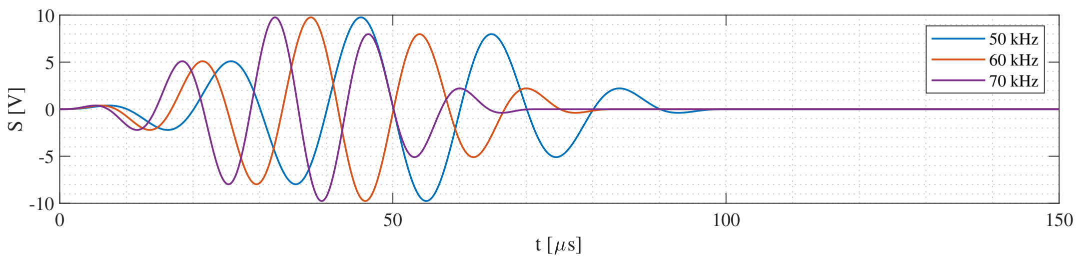

Figure 5.8: The diagnostic burst signals with center frequencies ω_c = 50, 60, and 70 kHz.

Data acquisition system

The settings used for the DAS are provided in table 5.6. The post-duration time is relatively large; this is done to ensure that each signal in the data contains the maximal number of samples of 8192. This simplified several steps in signal processing.

Table 5.6: Settings of the data acquisition system.

General		Hit definition settings			TR-Acquisition parameters	
Sample rate	Samples per set	Threshold	Rearm time	Duration discr. time	Pre-trigger	Post-duration
[MHz]	[$samples$]	[dB]	[μs]	[μs]	[μs]	[μs]
10	8192	30.1	250	250	200	800

5.3. Signal processing and wave velocity calculation

The signals recorded by the DAS consist of several features that are not desired to properly calculate the wave velocity, calculated using the arrival time or the time of flight (TOF). Examples of these features are noise and reflections. Therefore, several signal processing steps are carried out.

During the measurements, a total of approximately 35 signals were recorded. These signals are processed and averaged to obtain a desired smooth wave signal, from which the arrival times can be calculated. This process is explained in this section. For this, a measurement performed on plate 2 is used. The specifications of this plate are given in table 5.3. The diagnostic wave propagates in the 0° direction with a center frequency of ω_c = 60 kHz. First, we discuss the signal processing steps. Thereafter, the method for wave velocity calculation is explained.

5.3.1. Signal processing

The signal processing procedure consists of five steps. All steps are briefly discussed in the following parts. The goal of this process is to filter out bad signals and end up with a smooth averaged signal.

Raw signal

For the example measurement used, the data sets that contain all raw signals recorded by the transducers are shown in figure 5.9. The top and bottom graphs show the signals recorded by the first and second transducer, respectively. The data sets contain a signal for every waveform that crossed the transducer with an amplitude higher than the threshold value given in table 5.6. The number of signals recorded by both transducers for this example measurement is 35.

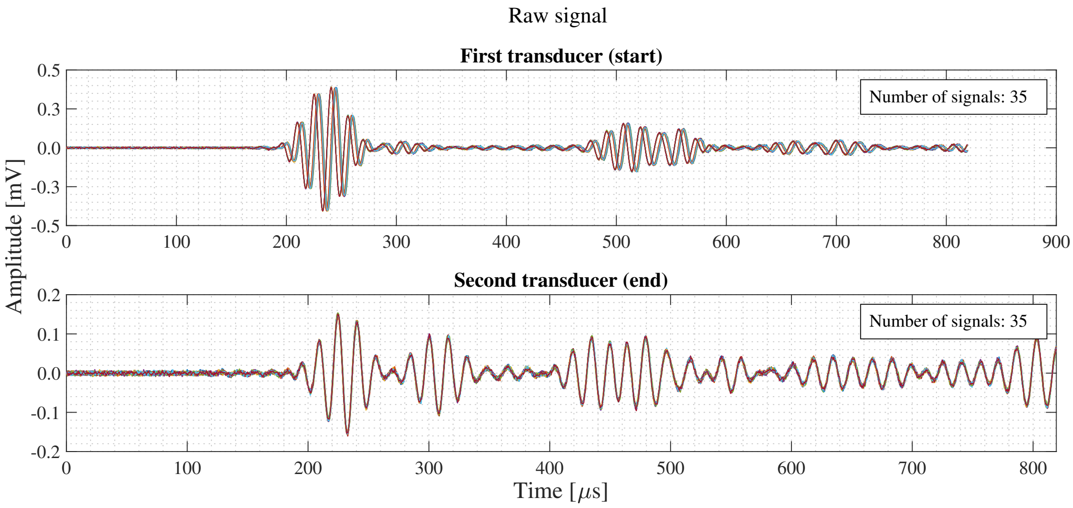

Figure 5.9: The raw signals recorded on plate type 2. The properties of the diagnostic waveform are: $\theta_i = 0°$ and $\omega_j = 60$ kHz. The top graph represents the data set recorded by the first transducer, and the lower graph represents the data set recorded by the second transducer. Both data sets consist of 35 signals.

Filtering based on arrival time

The first step in signal processing is to filter the data set based on the arrival time of the signals. Two filters are applied. First, we make sure that each signal is recorded by both transducers. If, for some reason, a signal is recorded by a single transducer, it is removed from the data set. Next, we make sure that the arrival time of subsequent signals corresponds to the burst period of 1 second, as given in table 5.5. For the example signal, both filters did not yield any signal removal, as can be seen in figure 5.10. Therefore, the raw and filtered signal of another measurement is shown in Appendix C. These data sets contain several signals that were filtered out in this first step.

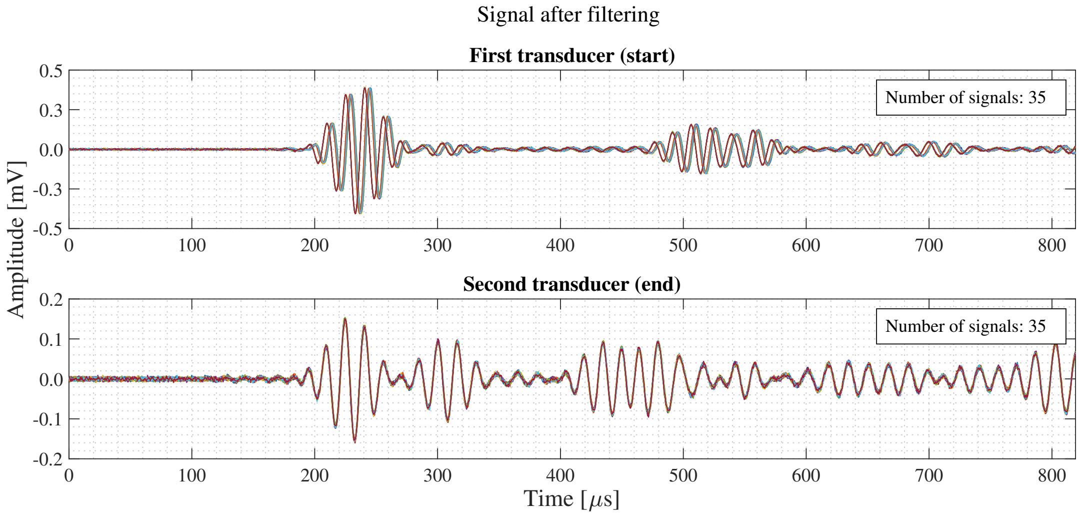

Figure 5.10: The signals after filtering based on the arrival time. The signals correspond to a diagnostic waveform with properties: $\theta_i = 0°$ and $\omega_j = 60$ kHz. The top graph represents the data set recorded by the first transducer, and the lower graph represents the data set recorded by the second transducer. Both data sets still consist of 35 signals.

Time shift

After filtering the data sets, a time shift is applied. This shift is based on the arrival time of the signal at both sensors. The arrival time t_{arr0} in this case is the arrival time of the signal relative to the start of the measurement. The arrival time of the signal recorded at the first transducer $t_{arr0,1}$ is considered the start time. The signal recorded at the second transducer $t_{arr0,2}$ is shifted over a time of Δt defined as in equation 5.11. The time shift is applied in the frequency domain. The resulting signals are shown in figure 5.11.

$$\Delta t = t_{arr0,2} - t_{arr0,1} \tag{5.1}$$

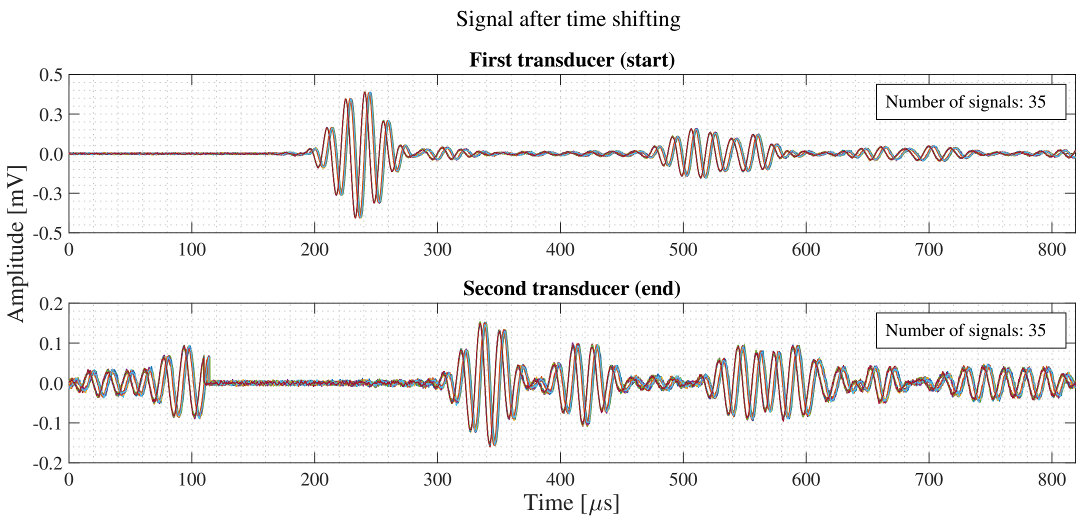

Figure 5.11: The signals after applying a time shift. The signals correspond to a diagnostic waveform with properties: $\theta_i = 0°$ and $\omega_j = 60$ kHz. The top graph represents the data set recorded by the first transducer, and the lower graph represents the data set recorded by the second transducer. Both data sets still consist of 35 signals.

Filtering based on the signal correlation

The next step in signal processing is filtering based on signal correlation. The correlation factor for each signal S_i with respect to the averaged signal S_{avg} is calculated using equation 5.2. In this equation N is the number of samples included in a signal, which is 8192 as provided in table 5.6. The correlation factor $Corr_i$ is divided by the correlation factor of the averaged signal $Corr_{avg}$, calculated using equation

5.3. This resulting correlation ratio is compared to a correlation criterion Criterion_c, see equation 5.4. Signals with a correlation ratio lower than the set criteria are removed from the data set. In total, this procedure is repeated four times with an increasing criterion every step. The criteria used are 0.7, 0.8, 0.9, and 0.95. S_{avg} changes every iteration and is calculated on the remaining signals after each iteration. Note that if the correlation ratio of a signal at a single transducer is lower than the criterion, the signals at both transducers are removed. For the example data set, 16 signals are removed, resulting in a remaining data set of 19 signals.

$$Corr_i = \sum_{n=1}^{N} S_i(n)S_{avg}(n) \tag{5.2}$$

$$Corr_{avg} = \sum_{n=1}^{N} S_{avg}(n)S_{avg}(n) \tag{5.3}$$

$$\frac{Corr_i}{Corr_{avg}} < \text{Criterion}_c \tag{5.4}$$

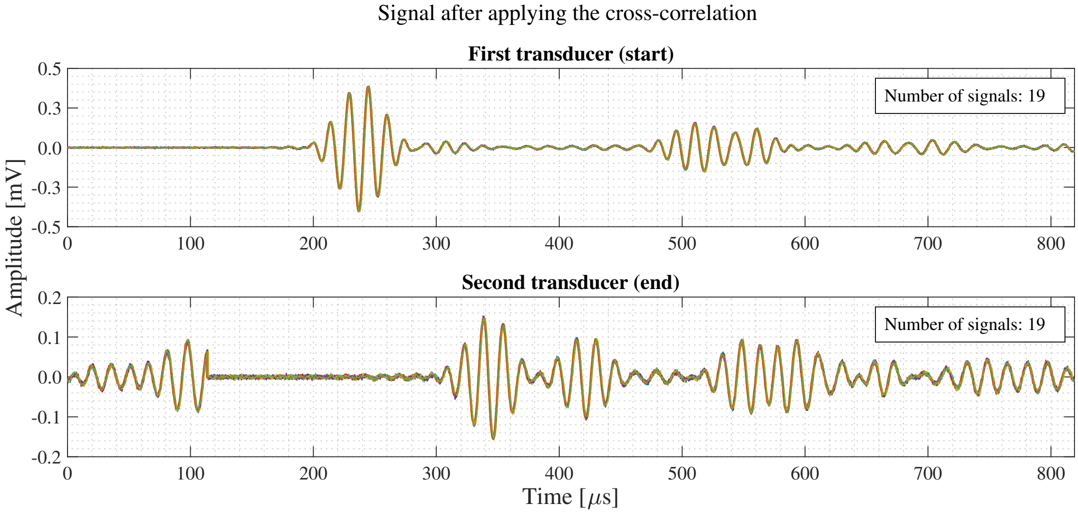

Figure 5.12: The signals after removing signals based on their correlation factor. The signals correspond to a diagnostic waveform with properties: $\theta_i = 0°$ and $\omega_j = 60$ kHz. The top graph represents the data set recorded by the first transducer, and the lower graph represents the data set recorded by the second transducer. In total 16 signals are removed, resulting in a remaining number of 19 signals.

Time window

Next, the reflections are removed from the signal by applying a time window function. A flat top window with cosine flanks of length $\Delta_{t,flanks}$ is applied on the data in the range of $t_{tw,s}$ to $t_{tw,e}$. The frequency-dependent variables for this time window are given in table 5.7. The signal before $t_{tw,s}$ and after $t_{tw,e}$ is zeroed. The signals after applying the time window function are shown in figure 5.13.

Table 5.7: Properties of the applied time window for both transducers.

Transducer [-]	$t_{tw,s}$ [μs]	$t_{tw,e}$ [μs]	$\Delta_{t,flanks}$ [μs]
1	130	330	20
2	130	430	30

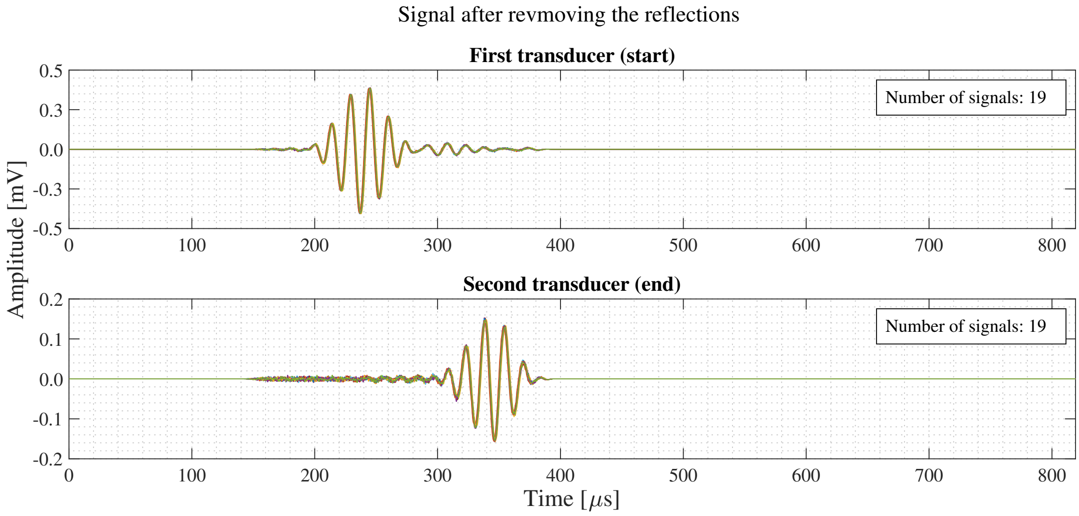

Figure 5.13: The signals after removing the reflections by applying a time window function. The signals correspond to a diagnostic waveform with properties: $\theta_i = 0°$ and $\omega_j = 60$ kHz. The top graph represents the data set recorded by the first transducer, and the lower graph represents the data set recorded by the second transducer. Both data sets consist of 16 signals.

Averaging

The last step in signal processing is to average the remaining signals. The final resulting signals are shown in figure 5.14.

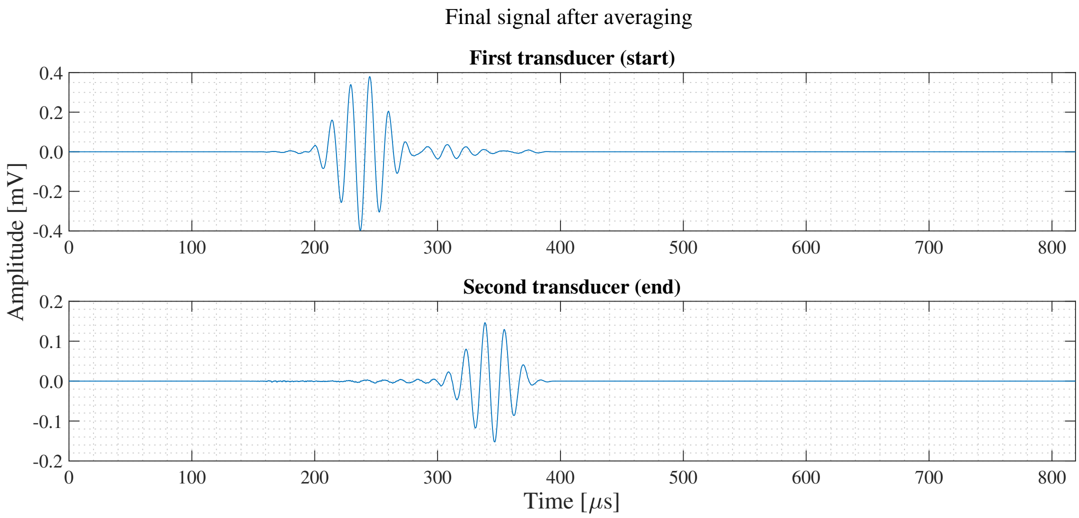

Figure 5.14: The final averaged signals corresponding to a diagnostic waveform with properties: $\theta_i = 0°$ and $\omega_j = 60$ kHz. The top graph represents the data set recorded by the first transducer, and the lower graph represents the data set recorded by the second transducer.

5.3.2. Calculation of the wave velocity

After signal processing, the velocities of the S_0 and A_0 waves are calculated. This calculation is based on the arrival time, that is, the time of flight (TOF), of both waves. In figure 5.14 it can be seen that at both transducers the A_0 wave, which contains the most energy, is most noticeable. Furthermore, the distance at which the first transducer is placed with respect to the actuator is too short to easily observe any dispersion. Therefore, it is difficult to distinguish the S_0 from the A_0 wave at this transducer. The waves have propagated over a longer distance when they arrive at the second transducer, this means that more dispersion has taken place. The S_0 wave propagates at a higher velocity than the A_0 wave; see figure 4.10. In figure 5.14, at the second transducer a small wave pattern can be observed before the arrival of the A_0 wave. This wave pattern corresponds to the S_0 wave.

The velocity of the A_0 wave c_{g,A_0} is calculated using equation 5.5, where d_{12} is the distance between the first and second transducer, see figure 5.15. t_{A_01}, and t_{A_02} are the arrival time of the A_0 wave at the first and second transducer, respectively. Since the arrival time of the S_0 wave at the first transducer cannot be obtained, the wave velocity of the S_0 wave c_{g,S_0} is calculated making use of the A_0 velocity. This is done using equation 5.6. In this equation d_{02} is the distance between the actuator and the second transducer, and t_{S_02} is the arrival time of the S_0 wave at the second transducer.

$$c_{g,A_0} = \frac{d_{12}}{t_{A_02} - t_{A_01}} \tag{5.5}$$

$$c_{g,S_0} = \frac{1}{\frac{1}{c_{g,A_0}} - \frac{t_{S_02} - t_{A_02}}{d_{02}}} \tag{5.6}$$

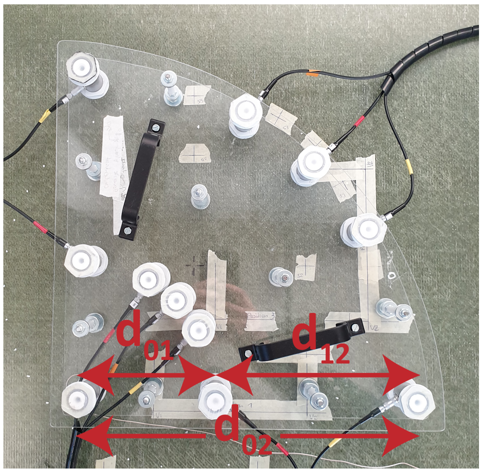

Figure 5.15: Top view of the measurement device with the distances between the actuator and transducers indicated.

Next, the procedure for extraction of arrival time is explained. For this, the time-picking of the waves at the second transducers is used as example. The same procedure can be applied to extract the arrival time at the first sensor.

Before computing both arrival times, a frequency filter is applied to the signal to filter out high-frequency noise waves. Therefore, for both waves, a time window is defined using a first determination of the A_0 wave arrival time without any frequency filtering. This arrival time t_{A0} is determined as the time at which the maximum peak of the wave envelope is reached. Based on this arrival time, the A_0 and S_0 windows are defined. The start twS_{0s} and end twS_{0e} of the S_0 window are defined by equations 5.7 and 5.8, respectively. The start twA_{0s} and end twA_{0e} of the A_0 window are defined by equations 5.8 and 5.9, respectively. In these equations, $T_{diagnostic}$ corresponds to the period of the generated diagnostic wave which is frequency dependent and listed in table 5.5. The start of the S_0 window ΔtS_{0s} is constant and is located at 100 μs. The resulting boundaries of the time windows are visualized in figure 5.16.

After defining the time windows, a frequency filter is applied in the frequency domain. Thereafter, the arrival time of the S_0 and A_0 wave is determined by extracting the time at which the peak amplitude of the A_0 and S_0 windows appear. In figure 5.17 the normalized S_0 and A_0 signals and their corresponding amplitudes are plotted as well as the determined arrival times of both waves t_{S_02} and t_{A_02}

$$twS_{0s} = \Delta tS_{0s} \tag{5.7}$$

$$twS_{0e} = twA_{0s} = t_{A0} - \frac{T_{diagnostic}}{2} \tag{5.8}$$

$$twA_{0e} = t_{A0} + \frac{T_{diagnostic}}{2} \tag{5.9}$$

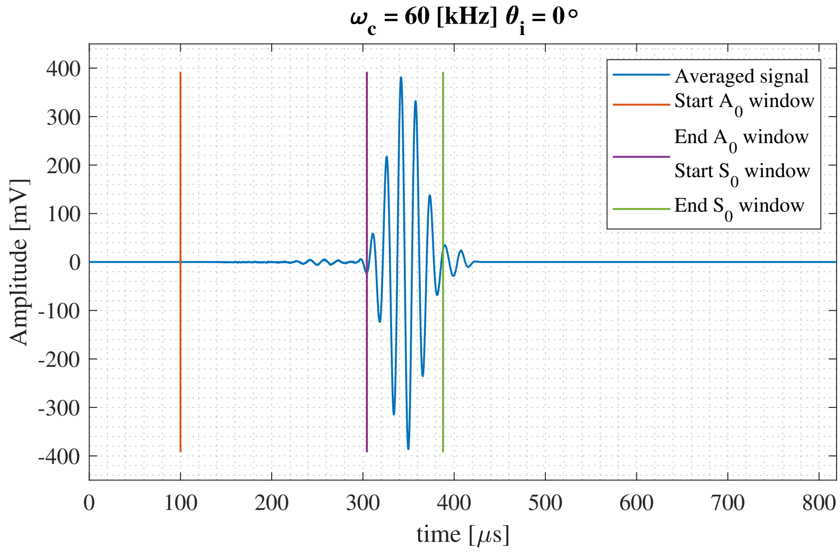

Figure 5.16: The averaged signal including the selected boundaries of the S_0 and A_0 time windows. The signal corresponds to the 60 kHz diagnostic signal propagation in the 0° direction. The signal is recorded at the second transducer.

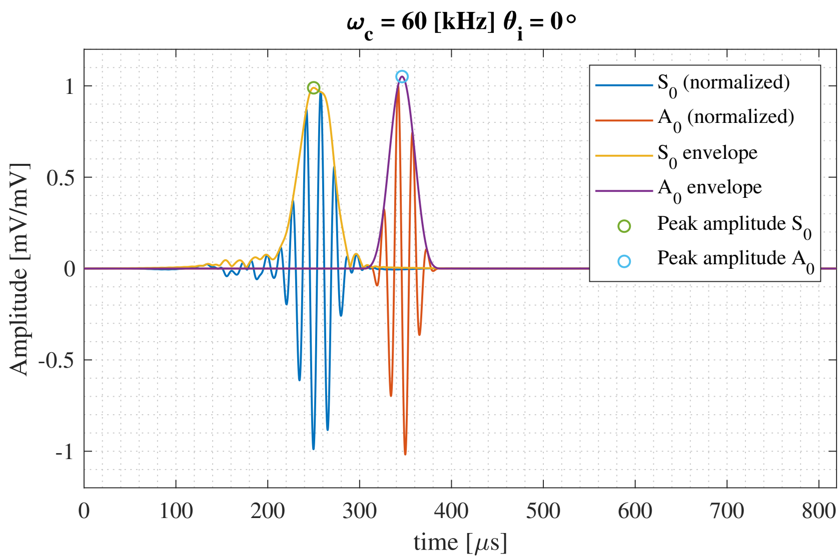

Figure 5.17: The normalized S_0 and A_0 wave signals including their corresponding envelopes and the computed peak amplitudes at $t_{S_0 2}$ and $t_{A_0 2}$. The signal corresponds to the 60 kHz diagnostic signal propagation in the 0° direction. The signal is recorded at the second transducer.

6
Results

In this chapter, the results are presented of the experimental stiffness assessment that is described in the previous chapter. In Section 6.1, a brief description is given of the measurements performed. Next, the extracted group wave velocities, which are used as input for the stiffness derivation, are shown and discussed in Section 6.2. In Section 6.3, a comparison is made between the approximated stiffness components and the stiffness components according to other references. Lastly, several chapter remarks are given in Section 6.4.

6.1. Measurement information

The measurements are performed on the sample plate described in the previous chapter. The properties of this plate can be found in tables 5.1 to 5.4. In order to minimize the presence of reflections in the recorded wave signal, the measurements are performed at the center of the plate, as shown in figure 6.1.

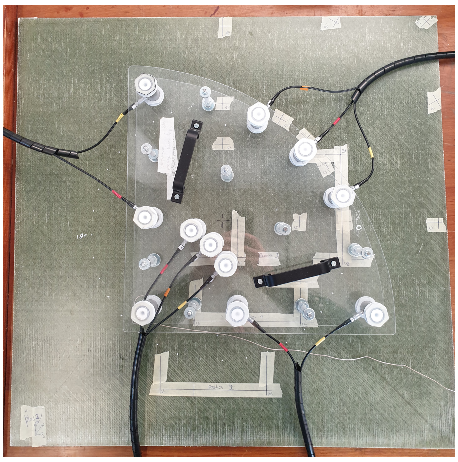

Figure 6.1: Top view of the measured location on the sample plate.

6.1.1. System configuration

The stacking sequence of the produced sample plate is known. The properties of the laminae were provided by manufacturing, but as stated in Section 5.1 it is unknown if these properties are accurate. This situation of known and unknown structural properties corresponds to the situation assumed in scenario **1** of the numerical feasibility study, described in Section 4.2. Therefore, based on the recorded group wave velocities, the ABD-components are approximated using a batch that is constructed similar to the batch of scenario **1**. In the numerical feasibility study, it was concluded that for scenario **1**, equations 4.2 and 4.9 can be used best. Therefore, these equations are used during the experiments.

$$c_1 A_{11} + c_2 A_{12} + \cdots + c_9 A_{66} + c_{19} D_{11} + c_{20} D_{12} + \cdots + c_{27} D_{66} = c_g^2 \quad \text{(Ref 4.2)}$$

$$\boldsymbol{C}\left(\{\boldsymbol{ABD}\} \odot \{1/\boldsymbol{ABD_{max}}\}\right)^{\mathrm{T}} = \{\boldsymbol{c_g^2}\} \quad \text{(Ref 4.9)}$$

The known structural properties of the constructed batch are the stacking sequence, the thickness of the ply, and the density of the material. These properties are given in tables 5.2 and 5.3. The unknown structural properties are the stiffness properties of the laminae. Therefore, in the batch used, these properties of the laminae vary from 80-120% with respect to the reference laminate. The properties of the laminae provided by the manufacturer are used as reference laminate properties, these are given in table 5.4. Thus, it is assumed that the actual properties of the laminae are somewhere in the range of 80-120% with respect to the properties provided in table 5.4. The constructed batch consists of 3500 reference laminates.

6.1.2. Reference properties

The exact ABD-components of the sample plates are unknown. To conclude about the reliability of the stiffness approximation, two references on the structural properties are used. The first reference set of ABD-components is based on the properties of the laminae provided by manufacturing. These are the properties of the laminae used for the plate of interest and are given in table 5.4. Using these properties and CLT, the ABD-components according to this reference are calculated. The second reference is the previous research by Zaal [77] on the determination of the stiffness of the sample plate. In that research, the properties of the laminae were approximated using a genetic algorithm based on the comparison of experimental and simulated wave velocities. The estimated stiffness properties of the laminae obtained in that study are shown in table 6.1. Similarly to the other reference, the ABD-components corresponding to this second reference are calculated using CLT. Note that both references are an estimation of the stiffness properties of the laminae. Therefore, these reference ABD-components serve only as an indication for the results obtained using the developed methodology.

Table 6.1: The stiffness properties of the laminae derived by Zaal [77].

E_1 [GPa]	$E_2 = E_3$ [GPa]	$G_{12} = G_{13}$ [GPa]	G_{23} [GPa]	$\nu_{12} = \nu_{13}$ [-]	ν_{23} [-]
51.1	16.1	5.16	5.58	0.29	0.45

6.2. Group wave velocity measurement

In tables 6.2 and 6.3 the experimental S_0 and A_0 group wave velocities derived on the sample plate are given. Also, the relative deviation of these velocities compared to the simulated velocities is given between the brackets, this is discussed later. The meaning of the values colored red is discussed later as well. Before the stiffness properties are calculated using the measured velocities, the reliability of each extracted velocity is assessed. The reasoning behind this reliability assessment is explained below. In the continuation of this chapter, the group velocity will be referred to as velocity.

Table 6.2: The experimental S_0 group wave velocities. The relative deviations to the simulated group velocities according to manufacturing and Zaal [77] are given between the first and second set of brackets respectively.

	c_{g,A_0}				
	[m/s]	[m/s]	[m/s]	[m/s]	[m/s]
θ_i	0°	30°	45°	60°	90°
50 [kHz]	3688 (-0.16%) (-8.37%)	3863 (3.27%) (-5.08%)	3835 (2.29%) (-6.02)	3639 (-2.71%) (-10.7%)	4023 (7.78%) (-1.19%)
60 [kHz]	3593 (-1.26%) (-9.44%)	3697 (-0.48%) (-8.50%)	3793 (1.72%) (-6.52%)	2841 (-23.6%) (-29.9%)	3821 (3.17%) (-5.52%)
70 [kHz]	3505 (-1.71%) (-9.96%)	3585 (-2.61%) (-10.4%)	3740 (0.99%) (-7.19%)	3165 (-14.1%) (-21.3%)	3901 (6.32%) (-2.75%)

Table 6.3: The experimental A_0 group wave velocities. The relative deviations to the simulated group velocities according to manufacturing and Zaal [77] are given between the first and second sets of brackets, respectively.

	c_{g,S_0}				
	$[m/s]$	$[m/s]$	$[m/s]$	$[m/s]$	$[m/s]$
θ_i	0°	30°	45°	60°	90°
50 $[kHz]$	1696 (2.82%) (-5.12%)	1676 (7.02%) (-1.99%)	1715 (13.5%) (3.34%)	1642 (11.1%) (0.64%)	1664 (12.5%) (1.79%)
60 $[kHz]$	1718 (4.08%) (-4.32%)	1678 (6.65%) (-2.73%)	1694 (11.0%) (0.73%)	1622 (7.94%) (-2.44%)	1667 (11.0%) (0.12%)
70 $[kHz]$	1731 (5.39%) (-3.36%)	1683 (7.07%) (-2.60%)	1690 (10.2%) (-0.21%)	1649 (8.72%) (-1.82%)	1678 (10.9%) (-0.17%)

To gain more sense of the measured wave velocities and assess their reliability, the velocities for each combination of wave mode and frequency are compared in a polar plot, given in figure 6.2. In these plots, the original measured velocities are colored blue and red, this color indication is discussed later. Furthermore, the reference velocities according to manufacturing and the research of Zaal [77] are added as well. These reference velocities are simulated using the SAFE method and the structural properties of both references, provided in tables 5.2, 5.3, 5.4, and 6.1. Relative deviations between the reference wave velocities and the measured wave velocities are given between the brackets in tables 6.2 and 6.3. This deviation is calculated using equation 6.1.

$$deviation = \frac{c_{g,exp} - c_{g,ref}}{c_{g,ref}} \cdot 100\% \tag{6.1}$$

When comparing the measured velocities with the simulated velocities according to manufacturing, significant differences are observed between the A_0 velocities of both methods. The S_0 velocities, on the other hand, are quite similar. Compared to the simulated velocities according to Zaal's research [77], these deviations are the other way around.

Because of the symmetric and balanced lay-up of the sample plate, it is expected that the velocities along symmetric counterpart directions show similar behavior. This means that velocities along the 0° and 90° directions, as well as along the 30° and 60° directions, are expected to show high similarities. Based on this expectation, it can be observed that, for each frequency, the S_0 velocities in the 30° and 60° directions show significant differences. Furthermore, for diagnostic signals of 50 and 70 kHz, the S_0 velocities in the 0° and 90° directions are not similar. These dissimilarities indicate possible faults in the measured velocities.

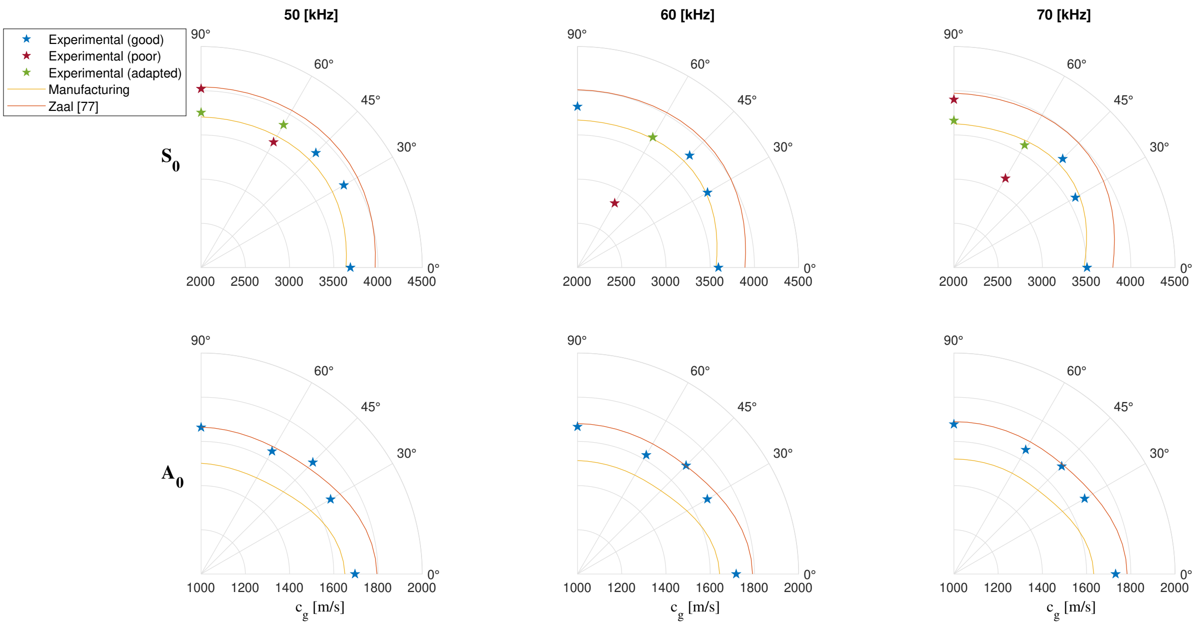

Figure 6.2: A comparison of the measured group wave velocities and the simulated group wave velocities according to the stiffness properties provided by manufacturing and Zaal [77]. The top three graphs correspond to the S_0 group velocities and the bottom three graphs to the A_0 group velocities. The original (good) measured group velocities are colored blue, the original poor measured group velocities are colored red and are replaced by the artificially adapted velocities colored green.

The quality of the measurements is assessed by looking at the windowed and normalized signals, created in the last phase of signal processing. From these figures, the arrival times of both wave modes are determined. In figure 6.3 the windowed and normalized signals of the 60 kHz diagnostic wave, propagating in the 60° direction are shown. This signal is recorded by the second transducer. In figure 6.3b the envelopes of the normalized S_0 and A_0 signals are shown as well, including the maximum peak amplitude of both envelopes. The S_0 wavelet is hardly visible in the windowed signal in figure 6.3a. As a result, the normalized S_0 wavelet and envelope are of poor quality; see figure 6.3b. When comparing this signal with its symmetric counterpart in the 30° direction, given in figure 6.4, one can conclude that the S_0 wavelet is better distinguishable in the 30° direction. This results in a normalized signal (see figure 6.4b) of good quality in which the S_0 and A_0 wavelets can be clearly distinguished.

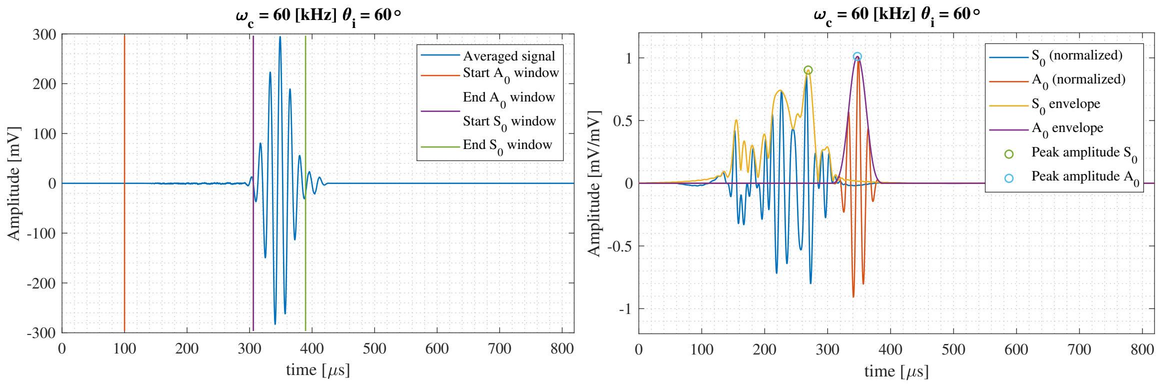

(a) Windowed signal **(b)** Normalized signal including envelope

Figure 6.3: The windowed (a) and normalized (b) signals of the 60 kHz diagnostic wave propagating in the 60° direction. The signals are recorded by the second transducer. In (b) the envelopes and the maximum peak amplitude of the envelopes are included.

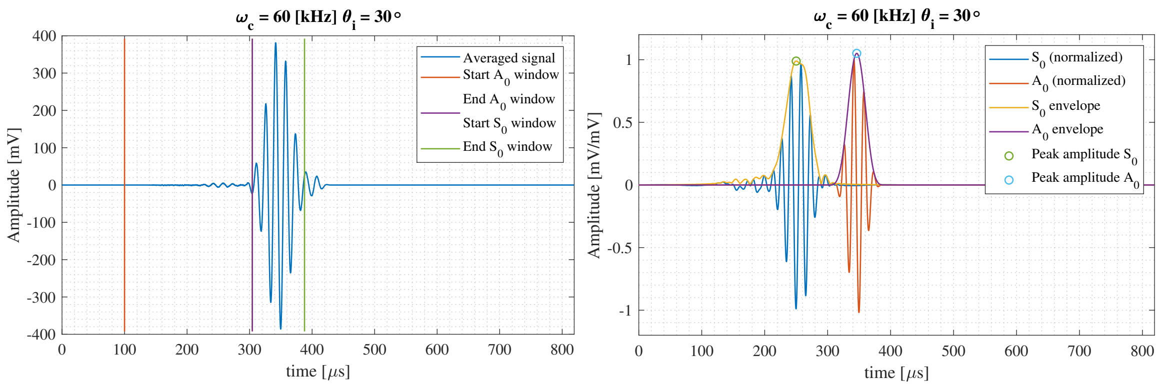

(a) Windowed signal **(b)** Normalized signal including envelope

Figure 6.4: The windowed (a) and normalized (b) signals of the 60 kHz diagnostic wave propagating in the 30° direction. The signals are recorded by the second transducer. In (b) the envelopes and the maximum peak amplitude of the envelopes are included.

Based on these observations, it is concluded that for the 60 kHz diagnostic wave, the extracted arrival time of the S_0 wave is more reliable in the 30° direction than in the 60° direction. Therefore, to provide a reliable set of input velocities to the system, the S_0 velocity in the 60° direction is artificially adapted based on the velocity of its symmetric counterpart in the 30° direction. This adapted velocity is calculated using equation 6.2, in which the simulated velocity in the direction of the poorly measured velocity θ_i is corrected by a factor α. In figure 6.2 it can be observed that there are small differences between the simulated velocities in the symmetric counterpart directions. This is caused by the location of each ply in the z-direction. This difference is taken into account in the artificially adapted velocity by the factor α, defined as equation 6.3. In this equation $c_{g,\theta_{ic},exp}$ and $c_{g,\theta_{ic},sim}$ are the experimental and simulated velocities in the counterpart direction θ_{ic}, respectively.

$$c_{g,\theta_i,adapt} = c_{g,\theta_i,sim} \cdot \alpha \tag{6.2}$$

$$\alpha = \frac{c_{g,\theta_{ic},exp}}{c_{g,\theta_{ic},sim}} \tag{6.3}$$

The just-described quality assessment procedure is applied to each measured signal. For each measurement a clear A_0 wavelet is recorded. Therefore, the quality of the extracted A_0 velocities is concluded to be reliable. Regarding the recorded S_0 wavelets, a total of five measured signals are concluded to be of poor quality. The windowed signals and normalized signals, including the envelopes, of these poor measurements and their symmetric counterpart signals are given in Appendix D. The velocities that were concluded to be of poor quality are colored red in tables 6.2 and 6.3, and in figure 6.2. Overall, the experimental S_0 velocities match better with the simulated manufacturing velocities, therefore, the simulated velocities according to manufacturing are used in equation 6.2 to calculate the adapted velocities. The adapted velocities are colored green in figure 6.2. The final data set of experimental velocities, used as input to determine the stiffness properties, is given in tables 6.4 and 6.5, in which the adapted values are colored green.

Table 6.4: Final experimental S_0 group wave velocities used as input for the stiffness approximation, including the adapted values colored green.

			c_{g,A_0}		
	$[m/s]$	$[m/s]$	$[m/s]$	$[m/s]$	$[m/s]$
θ_i	0°	30°	45°	60°	90°
50 $[kHz]$	3688 (-0.16%) (-8.37%)	3863 (3.27%) (-5.08%)	3835 (2.29%) (-6.02%)	3864 (3.32%) (-5.20%)	3754 (0.58%) (-7.79%)
60 $[kHz]$	3593 (-1.26%) (-9.44%)	3697 (-0.48%) (-8.50%)	3793 (1.72%) (-6.52%)	3703 (-0.37%) (-8.63%)	3821 (3.17%) (-5.52%)
70 $[kHz]$	3505 (-1.71%) (-9.96%)	3585 (-2.61%) (-10.4%)	3740 (0.99%) (-7.19%)	3599 (-2.38%) (-10.5%)	3664 (-0.16%) (-8.68%)

Table 6.5: The final experimental A_0 group wave velocities used as input for the stiffness approximation.

			c_{g,S_0}		
	$[m/s]$	$[m/s]$	$[m/s]$	$[m/s]$	$[m/s]$
θ_i	0°	30°	45°	60°	90°
50 $[kHz]$	1696 (2.82%) (-5.12%)	1676 (7.02%) (-1.99%)	1715 (13.5%) (3.34%)	1642 (11.1%) (0.64%)	1664 (12.5%) (1.79%)
60 $[kHz]$	1718 (4.08%) (-4.32%)	1678 (6.65%) (-2.73%)	1694 (11.0%) (0.73%)	1622 (7.94%) (-2.44%)	1667 (11.0%) (0.12%)
70 $[kHz]$	1731 (5.39%) (-3.36%)	1683 (7.07%) (-2.60%)	1690 (10.2%) (-0.21%)	1649 (8.72%) (-1.82%)	1678 (10.9%) (-0.17%)

6.3. Stiffness assessment

The experimental velocities presented in tables 6.4 and 6.5 are used as input for the methodology to approximate the stiffness components using equation 4.9. The results obtained from this stiffness approximation using the proposed methodology are given in table 6.6. In this table, the relative deviations of the approximated ABD-components compared to the stiffness components according to manufacturing and Zaal [77] are given as well. The deviations are calculated using equation 6.4 in which ABD_{cc} is the stiffness component approximated using the coupling coefficients and ABD_{ref} is the estimated stiffness component according to the reference.

$$Deviation = \frac{ABD_{cc} - ABD_{ref}}{ABD_{ref}} \cdot 100\% \tag{6.4}$$

Table 6.6: Results of the experimental stiffness approximation using the manufacturing batch.

	A_{11} $[MN/m]$	A_{12} $[MN/m]$	A_{22} $[MN/m]$	A_{66} $[MN/m]$	D_{11} $[kNm]$	D_{12} $[kNm]$	D_{16} $[kNm]$	D_{22} $[kNm]$	D_{26} $[kNm]$	D_{66} $[kNm]$
Proposed methodology	269.8	118.1	268.9	75.4	2.09	0.63	-0.09	0.95	-0.09	0.39
Deviation from manufacturing	15.1%	34.9%	15.1%	3.24%	16.2%	41.6%	23.9%	8.05%	23.9%	7.82%
Deviation from Zaal [77]	-10.0%	-6.41%	-10.0%	-12.7%	-4.35%	-3.78%	19.2%	-22.7%	19.2%	-9.36%

If we consider the diagonal ABD-components, it can be observed that the stiffness approximation using the coupling coefficients is higher compared to the estimation by manufacturing and lower compared to Zaal's [77] estimation. This can be explained by looking at the velocity comparison in figure 6.2. In general, the measured S_0 and A_0 wave velocities are higher than the manufacturing velocities and lower than the velocities of Zaal's research [77]. Similar deviations between experiments and references are obtained in the stiffness properties in table 6.6. This can be explained by the proportional relation between wave velocity and structural stiffness, given in Chapter 3. Hence, the differences between the experimental and reference stiffness properties are explicable.

One of the requirements for the methodology to work properly is that the actual stiffness properties of the plate of interest fall within the range of possible stiffness properties included in the batch. This requirement can be validated by checking whether the experimental wave velocities fall within the range of wave velocities included in the batch. This is possible since the range of S_0 and A_0 wave velocities included in the batch is representative for the range of laminae stiffness properties included in the batch. For the sample plate used in this experiment, it is assumed that the actual stiffness properties are within a range of 80-120% with respect to the stiffness properties provided by manufacturing. Based on this assumption and the assumption of a known ply thickness, stacking sequence, and material density, the batch of reference laminates is constructed. To check whether this assumption is valid, the experimental velocities are compared to the range of velocities of the batch in figure 6.5. In this figure, the range of wave velocities included in the batch based on manufacturing is colored yellow. In the continuation of this report, this batch is referred to as the manufacturing batch.

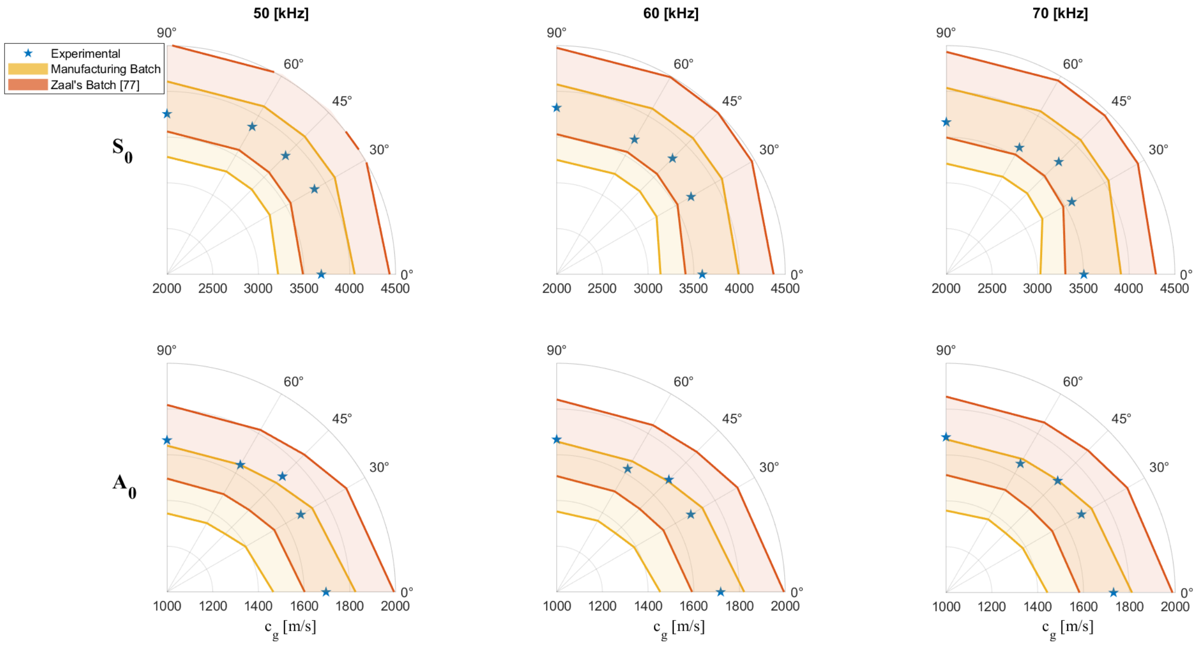

Figure 6.5: A comparison of the measured wave velocities and the simulated wave velocities according to the stiffness properties provided by manufacturing. The top three graphs correspond to the S_0 wave velocities and the bottom three graphs to the A_0 wave velocities.

From figure 6.5 we see that the experimental S_0 wave velocities fall within the range of S_0 velocities included in the manufacturing batch. The experimental A_0 velocities, on the other hand, are not well covered in the batch, since the obtained velocities are located close to or across the upper boundaries of the batch. Thus, from this figure, it can be concluded that the assumption that the actual stiffness properties fall within a 80-120% range compared to the manufacturing properties is not valid. Therefore, the reliability of the stiffness properties obtained, presented in table 6.6, is questionable.

A second batch of reference laminates is constructed. Unlike the manufacturing batch, this second batch assumes that the actual stiffness properties of the sample plate are within a 80-120% range with respect to the stiffness properties estimated by Zaal [77]. These properties were given in table 6.1. The other assumptions of a known thickness, staking sequence and density are still considered valid. This second batch also consists of 3500 reference laminates. The range of S_0 and A_0 velocities included in the batch is colored red in the polar plots of figure 6.5. This second batch is referred to as Zaal's batch in the continuation of this report.

The measured S_0 and A_0 wave velocities are located neatly within the boundaries of Zaal's batch. Therefore, compared to the manufacturing batch, one could conclude that the previously stated requirement for the methodology to work properly is met when using the stiffness properties provided by Zaal [77] as reference properties to construct the batch. Using Zaal's batch and the experimental velocities of tables 6.4 and 6.5 the stiffness components are approximated. The results are given in table 6.7.

Table 6.7: Results of the experimental stiffness approximation using Zaal's batch

	A_{11} $[MN/m]$	A_{12} $[MN/m]$	A_{22} $[MN/m]$	A_{66} $[MN/m]$	D_{11} $[kNm]$	D_{12} $[kNm]$	D_{16} $[kNm]$	D_{22} $[kNm]$	D_{26} $[kNm]$	D_{66} $[kNm]$
Proposed methodology	324.3	183.6	324.3	70.3	2.38	1.00	-0.09	1.26	-0.09	0.37
Deviation from manufacturing	38.8%	109.7%	38.8%	-3.71%	32.3%	125.0%	21.8%	43.2%	21.8%	2.17%
Deviation from Zaal [77]	8.48%	45.5%	8.48%	-18.6%	8.94%	52.9%	17.2%	2.51%	17.2%	-14.1%

The set of ABD-components obtained based on the Zaal batch shows significant differences compared to the estimated stiffness properties by manufacturing. This makes sense since it was previously concluded that the actual stiffness properties are not within 80-120% compared to these manufacturing properties. Compared to the estimation of the stiffness by Zaal [77], reasonable differences are obtained for the diagonal ABD-components. Larger differences are obtained for the off diagonal ABD-components.

However, it is difficult to conclude about the accuracy of the stiffness approximation, as the actual properties of the sample plate are unknown. Therefore, in the next section several remarks on the obtained results are given.

6.4. Chapter remarks

The previous section presented the results of the stiffness approximation on the sample plate. Based on these results, the system configuration used, the extracted group wave velocities, and the reference cases used, the following remarks should be given.

- In the application of the methodology in the experimental setup, a couple of assumptions were made. Scenario **1** of the numerical feasibility study was assumed to be applicable to the sample plate used in the experiments. Therefore, it was assumed that the ply thickness, stacking sequence, and material density were known. On the basis of these assumptions, the batch of reference laminates was constructed and used for the stiffness approximation. Input for this approximation were the measured wave velocities. In the numerical feasibility study, the assumptions of scenario **1** could be easily made since they were applicable to both batch construction and velocity input. When the methodology is being applied in-situ these assumptions are, however, more challenging since they are only incorporated in the batch construction and may not be valid to the sample plate and thus the input wave velocity measured on the plate.

  The risk of the assumptions can be summarized as a possible mismatch between the constructed batch and the actual structural properties. In Section 6.3 we have seen that when the range of possible stiffness of the plate of interest is not covered well, the stiffness approximation obtained is unreliable. In that specific situation, the assumption of the range in which the actual stiffness properties of the laminae were located was not valid. Poor assumptions regarding the ply thickness, the stacking sequence, or the material density can result in a similar mismatch between the constructed batch and actual structural properties. Including some margin with respect to these properties is, therefore, desired.

- In Section 6.2 the extracted wave velocities, used as input for the methodology, are presented. Some difficulties were experienced in extracting the velocity of the S_0 wave mode and a total of five signals were concluded to be unreliable and were adapted. Thus, the velocity vector used as input for the system is not purely characteristic for the sample plate, which may result in small differences between the approximated and actual stiffness properties.

- The actual stiffness properties of the sample plate are unknown which makes it difficult to conclude about the accuracy of the methodology applied in-situ. Two batches were used to assess the stiffness of the sample plate. The usability of the batches was examined by comparing the experimental group wave velocities and the range of group wave velocities included in the batch. It was concluded that the manufacturing batch could not be used. This indicates that in the future the range of stiffness properties included in the batch should be widened to better deal with deviations in material properties. For this, one can consider separate ranges for each material property.

7
Conclusions

In this research, a new methodology is proposed to determine the structural stiffness of Fiber Reinforced Composite materials. The main research question answered in the conclusion of this thesis is:

How can the structural laminate stiffness of Fiber Reinforced Composite materials be analyzed in-situ using ultrasonic guided waves?

Several studies have been conducted on the determination of the stiffness of FRC materials using ultrasonic guided wave. In these studies, a certain amount of structural information is assumed to be known. In addition, their in-situ applicability is limited. Therefore, to make this research of added value, the methodology developed must meet certain accuracy and practical standards. These design requirements are translated into three subquestions that are addressed in this thesis. The answer to each of the subquestions is formulated below.

1. **How can the stiffness matrix of a Fiber Reinforced Composite material be derived using ultrasonic guided waves?**

   The proposed methodology uses a coupling principle between the laminate structural stiffness and the ultrasonic guided wave characteristics. This methodology is based on the proportional relation between structural stiffness and wave velocity. A formulation is assumed which describes the relation between the ABD-components and wave velocity using a set of coupling coefficients. The coupling coefficients are determined based on a plate of interest for which a certain amount of structural information is available. In order to do so, a batch of reference laminates is constructed which describes the stiffness possibility range of the plate of interest based on the available structural information. The wave velocities of these reference laminates are simulated using the Semi-Analytical Finite Element method. The coupling coefficients can be interpreted as the coefficients that best describe the relation between the ABD-components and the wave velocities of the reference laminates included in the batch.

   The potential of the methodology was evaluated using a numerical feasibility study. In this study three scenarios, that differ in available structural information, were considered. It was concluded that the ABD-approximation for each scenario converged to constant results when the number of reference laminates included in the batch is sufficiently large. This required batch size is different for each scenario. Secondly, it was concluded that for every scenario a total of 30 wave characteristics included in the system is sufficient to obtain converged approximations. These characteristics consist of wave velocities of the S_0 and A_0 wave modes measured along five propagation directions at three wave frequencies.

   The accuracy of the converged stiffness approximation was addressed in the second subquestion.

2. **How is the accuracy of the methodology dependent on the amount of prior structural information?**

   The accuracy of the proposed methodology is evaluated in the numerical feasibility study for which the same scenarios are used. In addition, different variants on the methodology have been tested in this study. It was concluded that for a scenario in which the stacking sequence of the plate of interest are known but the properties of the laminae are unknown, the ABD-components can all be approximated within an error of 4% compared to the components calculated using CLT. In the scenario where the properties of the laminae are known but the stacking sequence is unknown, the A-components can be approximated within an error of 2%. Regarding the D-components, D_{11} and D_{22} can be approximated within an error of 10%, and D_{12} and D_{66} within an error of 17%. Stiffness components D_{16} and D_{26} cannot be approximated in this scenario. In the last scenario, where both the stacking sequence and the properties of the laminae are unknown, the diagonal A-components can be approximated within a 3% error and the diagonal D-components within a 16% error. The off-diagonal stiffness components cannot be approximated for this scenario.

3. **How can the methodology be applied in-situ while still providing an accurate stiffness assessment?**

   The methodology has been applied in an experimental setup consisting of a waveform generator, a wave actuator, ten DPC transducers, and a data acquisition system. Measurements were performed on a sample plate for which the ply thickness, stacking sequence, and material density were assumed to be sufficiently known. However, the stiffness properties of the laminae were unknown. The estimated stiffness properties provided by manufacturing and by previous research of Zaal [77] were used as an indication of the results.

   The extracted A_0 wave velocities are measured with reasonable accuracy. Difficulties were experienced in the velocity extraction of the S_0 waves. This may be caused by the presence of noise, higher-order wave modes, higher- or lower-frequency waves, or by insensitivity to the S_0 wave due to poor contact of the transducer or poor quality of the transmitted diagnostic wave. The five poor-quality signals were replaced by adapted velocities based on measured velocities in the symmetric counterpart directions and simulated velocities.

   For both references, a separate batch of reference laminates was constructed. On the basis of a comparison between the experimental wave velocities and the wave velocities included in the batches, it was concluded that the stiffness properties provided by manufacturing were unreliable. The stiffness properties approximated using the batch based on the research of Zaal [77] were within a reasonable range compared to the properties of Zaal [77]. Differences in the range of 2-15% were obtained for the diagonal stiffness components. Differences in the range of 17-53% were obtained for the off-diagonal components.

   The methodology has been successfully applied in-situ by assessing the structural stiffness properties using a compact device and reasonable measurement and analysis time. An accuracy assessment of the in-situ application of the methodology is difficult to obtain since the exact stiffness properties of the material are unknown. Also, in the current in-situ application, several assumptions are made with respect to the structural properties. The validity of these assumptions comes, contrary to the numerical feasibility study, with some uncertainty. Therefore, the inclusion of some margin with respect to these assumptions is desired when the methodology is applied in-situ.

8

Future Research

In this chapter, recommendations for future research are suggested. The recommendations are subdivided into fundamental research, which focuses on expanding the knowledge on the proposed methodology, and applied research, which focuses on the in-situ application of the methodology.

8.1. Fundamental research

In this study, the feasibility of the proposed methodology is assessed using so-called scenarios. These scenarios differ in the amount and type of prior structural information of the composite plate of interest. Three scenarios were considered in which the stiffness properties of the laminae, the stacking sequence, or both were unknown. In each scenario, the ply thickness and material density were assumed to be known.

On the basis of the experiments, it was concluded that these assumptions are difficult to make when the method is applied in-situ. This is caused by the relatively high uncertainties in material properties and structural integrity after production, as described in the literature review. Therefore, in future research, the feasibility of the methodology should be expanded considering a wider range of uncertain / unknown material properties, including properties such as ply thickness and material density. Therefore, new scenarios have to be defined and examined. Regarding the in-situ application of the methodology, the scenarios should be based on situations often faced in practice. For example, as discussed in the literature review, a lay-up error after production may cause a deviation of a couple degrees from the desired lay-up. Therefore, instead of assuming a complete unknown stacking sequence as in scenario **2**, deviations in the orientations of a single or multiple plies should be considered. Again, the feasibility of the methodology for these new scenarios can be examined using numerical simulations.

8.2. Applied research

8.2.1. Quality of the measurement

One of the three factors that determines the accuracy of the proposed methodology is the accuracy of the wave velocities, used as input for the stiffness approximation. The measurements performed in this research consisted of five wave signals from which the S_0 wave velocity could not be extracted due to the poor quality of the recorded signal. In general, the sensitivity of the DPC transducers to the S_0 wave was found to be challenging.

Therefore, in order to increase the reliability of the measured wave velocities, more research is required into the experimental setup. Here, both the wave transmitting components and the wave recording components should be further explored.

8.2.2. Time picking

Similarly to the quality of the measurement, the method used to determine the arrival time of the different wave modes determines the accuracy of the system's input. In current research the arrival time of the S_0 and A_0 waves was determined using the maximum peak of the wave envelopes. This method is considered a rather basic time-picking method. The use of more advanced methods should be considered and further explored. Additionally, the diagnostic waveform should be further explored to find the optimal match with the time-picking method. An example of a more advanced method is time picking using a Short Time Fourier Transform (STFT) which provides insight in the arrival time of each frequency included in a signal.

8.2.3. High quality reference studies

In this research, experiments were performed on a sample plate for which the stacking sequence, the ply thickness, and the material density were assumed to be known. Furthermore, two references on the expected stiffness properties of the laminae were available. These references were used as an indication for the results obtained using the developed methodology. However, the exact stiffness properties of the material are unknown.

To conclude about the accuracy of the methodology when applied in-situ, more reliable estimations of the stiffness properties are required. Currently, mechanical testing methods are reliable methods for characterizing the stiffness properties of materials with uncertain properties. Therefore, a schematic cutting plan is already available to obtain test specimens, see figure 8.1a. These specimens can be used to characterize the material properties from bending and extension tests, see figure 8.1b.

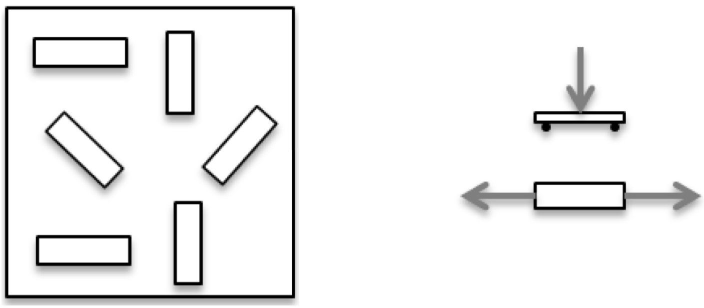

(a) **(b)**

Figure 8.1: (a) The cutting plan to obtain test specimens that can be used for (b) material characterization from bending and tensile tests.

References

[1] A. M. et al. “Review of advanced composite structures for naval ships and submarines”. In: *Composite Structures 53*. 2001, pp. 21–41.

[2] I. M. Daniel and O. Ishai. *Engineering Mechanics of Composite Materials*. second. Oxford University Press, 2006.

[3] U. secretariat. *The Paris Agreement*. Sept. 2020. URL: https://unfccc.int/process-and-meetings/the-paris-agreement/the-paris-agreement.

[4] E. Commission. *A European Green Deal: Striving to be the first climate-neutral continent*. URL: https://ec.europa.eu/info/strategy/priorities-2019-2024/european-green-deal_en.

[5] E. Commission. *Reducing emissions from the shipping sector*. URL: https://ec.europa.eu/clima/policies/transport/shipping_en.

[6] E. Commission. *Proposal For a Regulation of the European Parliament and of the Council*. Tech. rep. European Union, 2019.

[7] D. Chalmers. “The Potential for the Use of Composite Materials in Marine Structures”. In: *Marine Structures 7*. 1994, pp. 441–456.

[8] K. R. et al. “Recent Material Advancement for Marine Application”. In: *Materials Today: Proceedings 18*. Elsevier, 2019, pp. 4854–4859.

[9] A. Ghobadi. “Common Type of Damages in Composites and Their Inspections”. In: *World Journal of Mechanics*. 2017, pp. 24–33.

[10] G. Gardiner. *Removing the barriers to lightweighting ships with composites*. Tech. rep. CompositesWorld, 2019.

[11] T. M. Executive. *Propulsion’s Composite Future*. Mar. 2016. URL: https://www.maritime-executive.com/features/propulsions-composite-future.

[12] Yachtworld. *5 great superyachts at Les Voiles de Saint-Tropez*. Nov. 2014. URL: https://www.yachtworld.co.uk/research/tag/velsheda/.

[13] B. International. *First photos of dolphin-inspired superyacht Yas underway*. July 2015. URL: https://www.boatinternational.com/yachts/news/first-photos-of-dolphin-inspired-superyacht-yas-underway--24625?utm_source=Adestra%5C&utm_medium=email%5C&utm_content=%5C&utm_campaign=Daily+news+-+2015-07-29.

[14] M. H. et al. “Cost and weight of composite ship structures: A parametric study based on Det Norske Veritas rules”. In: *Journal of Engineering for the Maritime Environment*. 2018, pp. 331–350.

[15] S. J. et al. “Recycling of Composite Marine Structures”. In: *Twenty-eighth National Convention of Mechanical Engineers and National Seminar on Emerging Technologies in Product Development for Safe and Sustainable Mobility*. 2012.

[16] D. L. Dokos. “Adoption of marine composites - a global perspective”. In: *Reinforced Plastics 57*. 2013, pp. 30–32.

[17] M. Ibrahim. “Marine Applications of Advanced Fibre-reinforced Composites”. In: Elsivier, 2015. Chap. 7: Nondestructive testing and structural health monitoring of marine composite structures.

[18] A. Martens, M. Kersemans, J. Daemen, E. Verboven, W. V. Paepegem, J. Degrieck, S. Delrue, and K. V. D. Abeele. “Numerical study of the Time-of-Flight Pulsed Ultrasonic Polar Scan for the determination of the full elasticity tensor of orthotropic plates”. In: *Composite Structures* 180 (2017), pp. 29–40.

[19] M. I. et al. “Carbon coated piezoresistive fiber sensors: From process monitoring to structural health monitoring of composites – A review”. In: *Composites Part A 141*. Elsevier, 2021.

[20] A. N. Z.
bibinitperiod V. Giurgiutiu. "Electomechanical Impedance Modeling". In: *Encyclopedia of Structural Health Monitoring*. 2009.

[21] H. D.
bibinitperiod E. T. Thostenson. "Scalable and multifunctional carbon nanotube-based textile as distributed sensors for flow and cure monitoring". In: *Carbon 164*. Elsivier, 2020, pp. 28–41.

[22] R. Bossi and V. Giurgiutiu. "15 - Nondestructive testing of damage in aerospace composites". In: *Polymer Composites in the Aerospace Industry*. Ed. by P. Irving and C. Soutis. Woodhead Publishing, 2015, pp. 413–448.

[23] V. Giurgiutiu. *Structural Health Monitoring With Piezoelectric Wafer Active Sensors*. second. Elsevier, 2014.

[24] S. Gholizadeh. "A review of non-destructive testing methods of composite materials". In: *Procedia Structural Integrity* 1 (2016), pp. 050–057.

[25] D. of Defense - United States of America. *Composite Materials Handbook*. Vol. 1. Polymer Matrix Composites Guidelines for Characterization of Structural Materials. SAE International, 2002.

[26] N. Saba, M. Jawaid, and M. Sultan. "An overview of mechanical and physical testing of composite materials". In: *Mechanical and Physical Testing of Biocomposites, Fibre-Reinforced Composites and Hybrid Composites*. Ed. by M. Jawaid, M. Thariq, and N. Saba. Elsevier Ltd., 2019. Chap. 1, pp. 1–12.

[27] M. Rojek, J. Stabik, and G. Wróbel. "Ultrasonic methods in diagnostics of epoxy–glass composites". In: *Journal of Materials Processing Technology* 162-163 (2005), pp. 121–126.

[28] S. K. Dwivedi, M. Vishwakarma, and P. A. Soni. "Advances and Researches on Non Destructive Testing: A Review". In: *Materials Today: Proceedings* 5 (2018), pp. 3690–3698.

[29] A. Katunin, K. Dragan, and M. Dziendzikowski. "Damage identification in aircraft composite structures: A case study using various non-destructive testing techniques". In: *Composite Structures 127 (2015) 1–9* 127 (2015), pp. 1–9.

[30] M. Castaings and B. Hosten. "Ultrasonic guided waves for health monitoring of high-pressure composite tanks". In: *NDT&E International* 41.8 (2008), pp. 648–655.

[31] P. Cawley. "The rapid non-destructive inspection of large composite structures". In: *Composites* 25.5 (1994), pp. 351–357.

[32] S. Doebling, C. Farrar, and M. Prime. "A summary review of vibration-based damage identification methods". In: *Shock and Vibration Digest* 30.2 (Mar. 1998), pp. 91–105.

[33] K. Balasubramanian, M. T. Sultan, and N. Rajeswari. "Sustainable Composites for Aerospace Applications". In: vol. 364. Woodhead Publishing Series in Composites Science and Engineering, 2018. Chap. 4 - Manufacturing techniques of composites for aerospace applications.

[34] R.Talreja. "Polymer Composites in the Aerospace Industry". In: vol. 520. Woodhead Publishing, 2014. Chap. 5 - Manufacturing defects in composites and their effects on performance.

[35] P. Kulkarni, K. D. Mali, and S. Singh. "An overview of the formation of fibre waviness and its effect on the mechanical performance of fibre reinforced polymer composites". In: *Composites Part A* 137 (2020).

[36] M. Suriani, A.Ali, A. Khalina, S. Sapuan, and S. Abdullah. "Detection of Defects in Kenaf/Epoxy using Infrared Thermal Imaging Technique". In: *Procedia Chemistry* 4 (2012), pp. 172–178.

[37] M. Suriani, H. Z. Rapi, R. Ilyas, M. Petru, and S. Sapuan. "Delamination and Manufacturing Defects in Natural Fiber-Reinforced Hybrid Composite: A Review". In: *Polymers* 13.8 (2021).

[38] D. K. Rajak, D. D. Pagar, P. L. Menezes, and E. Linul. "Fiber-Reinforced Polymer Composites: Manufacturing, Properties, and Applications". In: *Polymers* 11.10 (2019).

[39] K. Potter. "Understanding the origins of defects and variability in composites manufacture". In: *ICCM International Conferences on Composite Materials* 17 (2009).

[40] C. Zhao, J. Xiao, Y. Li, Q. Chu, T. Xu, and B. Wang. "An Experimental Study of the Influence of in-Plane Fiber Waviness on Unidirectional Laminates Tensile Properties". In: *Applied Composite Materials* 24.6 (2017), pp. 1321–1337.

[41] S. N. Nair, A. Dasari, C. Y. Yue, and S. Narasimalu. "Failure behavior of unidirectional composites under compression loading: Effect of fiber waviness". In: *Materials* 10.8 (2017).

[42] B. Khan, K. D. Potter, and M. R. Wisnom. "Simulation of process induced defects in resin transfer moulded woven carbon fibre laminates and their effect on mechanical behaviour". In: *Flow Processes in Composite Materials* 8 (2006).

[43] L. Wang. "Effects of in-plane fiber waviness on the static and fatigue strength of fiberglass". MA thesis. Montana State University-Bozeman, 2001.

[44] H. Huang and R. Talreja. "Effects of void geometry on elastic properties of unidirectional fiber reinforced composites". In: *Composites Science and Technology 65* 65.13 (2005), pp. 1964–1981.

[45] P.-O. Hangstrand, F. Bonjour, and J. .-. Manson. "The influence of void content on the structural flexural performance of unidirectional glass fibre reinforced polypropylene composites". In: *Composites: Part A* 36 (2005), pp. 705–7014.

[46] M. Mehdikhani, L. Gorbatikh, I. Verpoest, and S. V. Lomov. "Voids in fiber-reinforced polymer composites: A review on their formation, characteristics, and effects on mechanical performance". In: *Journal of Composite Material* 53.12 (2019), pp. 1579–1669.

[47] J. E. Little, X. Yuan, and M. I. Jones. "Characterisation of voids in fibre reinforced composite materials". In: *NDT&E International* 46 (2012), pp. 122–127.

[48] L. Wang and F. Yuan. "Group velocity and characteristic wave curves of Lamb waves in composites: Modeling and experiments". In: *Composites Science and Technology* 67.7-8 (2007), pp. 1370–1384.

[49] A. Raghavan. "Guided-wave structural health monitoring". PhD thesis. The University of Michigan, 2007.

[50] R. Guan, Y. Lu, W. Duan, and X. Wang. "Guided waves for damage identification in pipeline structures: A review". In: *Structural Contral Health Monitoring* 24.11 (2017).

[51] Z. Su, L. Ye, and Y. Lu. "Guided Lamb waves for identification of damage in composite structures: A review". In: *Journal of Sound and Vibration* 295.3-5 (2006), pp. 753–780.

[52] J. L. Rose. *Ultrasonic Guided Waves in Solid Media*. first. Cambridge University Press, 2014.

[53] M. Lemistre and D. Balageas. "Structural health monitoring system based on diffracted Lamb wave analysis by multiresolution processing". In: *Smart Materials and Structures* 10 (2001), pp. 504–511.

[54] J. F. Doyle. *Wave Propagation in Structures - Spectral Analysis Using Fast Discrete Fourier Transforms*. second. Vol. 335. Mechanical Engineering Series. Springer, 1997.

[55] FOSCO. *Phase Velocity, Group Velocity, and Dispersion*. URL: `https://www.fiberoptics4sale.com/blogs/wave-optics/phase-velocity-group-velocity-and-dispersion`.

[56] I. Bartoli, A. Marzani, F. L. di Scalea, and E. Viola. "Modeling wave propagation in damped waveguides of arbitrary cross-section". In: *Journal of Sound and Vibration* 295.3-5 (2006), pp. 685–707.

[57] J. L. Rose. "A Baseline and Vision of Ultrasonic Guided Wave Inspection Potential". In: *Journal of Pressure Vessel Technology, Transactions of the ASME* 124.3 (2002), pp. 273–282.

[58] J. Rose, A. Pilarski, and J. Ditri. "An Approach to Guided Wave Mode Selection for Inspection of Laminated Plate". In: *Journal of Reinforced Plastics and Composites* 12.5 (1993), pp. 536–544.

[59] R. Monkhouse, P. Wilcox, M. Lowe, R. Dalton, and P. Cawley. "The rapid monitoring of structures using interdigital Lamb wave transducers". In: *Smart Materials and Structures* 9.3 (2000), pp. 304–309.

[60] M. Markham. "Measurement of the elastic constants of fibre composites by ultrasonics". In: *Composites* 1.3 (1970), pp. 145–149.

[61] K. Balasubramaniam and S. C. Whitney. "Ultrasonic through-transmission characterization of thick fibre-reinforced composites". In: *NDT&E International* 29.4 (1996), pp. 225–236.

[62] C. M. Valencia, J. Pazos-Ospina, E. Franco, J. L. Ealo, D. Collazos-Burbano, and G. C. Garcia. "Ultrasonic determination of the elastic constants of epoxiy-natural fiber composites". In: *Physics Procedia* 70 (2015), pp. 467–470.

[63] C. Yilmaz, S. Topal, H. Ali, I. Tabrizi, A. Al-Nadhari, A. Suleman, and M. Yildiz. "Non-destructive determination of the stiffness matrix of a laminated composite structure with lamb wave". In: *Composite Structures* 237 (2020).

[64] J. H. Tam, Z. C. Ong, Z. Ismail, B. C. Ang, and S. Y. Khoo. "Identification of material properties of composite materials using nondestructive vibration alevaluation approaches: A review". In: *Mechanics of Advanced Materials and Structures* 24.12 (2017), pp. 971–986.

[65] J. Vishnuvardhan, C. Krishnamurthy, and K. Balasubramaniam. "Genetic algorithm based reconstruction of the elastic moduli of orthotropic plates using an ultrasonic guided wave single-transmitter-multiple-receiver SHM array". In: *Smart Materials and Structures* 16.5 (2007), pp. 1639–1650.

[66] M. Castaings, B. Hosten, and T. Kundu. "Inversion of ultrasonic, plane-wave transmission data in composite plates to infer viscoelastic material properties". In: *NDT&E International* 33 (2000), pp. 377–392.

[67] B. Hosten. "Reflection and transmission of acoustic plane waves on an immersed orthotropic and viscoelastic solid layer". In: *The Journal of the Acoustical Society of America* 89.6 (1991), pp. 2745–2752.

[68] A. Kamal and V. Giurgiutiu. "Stiffness Transfer Matrix Method (STMM) for Stable Dispersion Curves Solution in Anisotropic Composites". In: *Health Monitoring of Structural and Biological Systems*. Vol. 9064. 2014.

[69] L. Knopoff. "A matrix method for elastic wave problems". In: *Bulletin of the Seismological Society of America* 54.1 (1964), pp. 431–438.

[70] P. Delsanto, R. Schechter, and R. Mignogna. "Connection machine simulation of ultrasonic wave propagation in materials III: The three-dimensional case". In: *Wave Motion* 26.4 (1997), pp. 239–339.

[71] B. Barazanchy and V. Giurgiutiu. "A comparative convergence and accuracy study of composite guided-ultrasonic wave solution methods: Comparing the unified analytic method, SAFE method and DISPERSE". In: *Proceedings of the Institution of Mechanical Engineers, Part C: Journal of Mechanical Engineering Science* 231.16 (2017), pp. 2961–2973.

[72] N. Baddour. "Leading-Edge Applied Mathematical Modeling Research". In: Nova Science Publisher, 2007. Chap. Chapter 4: Hamilton's Principle for the Derivation of Equations of Motion.

[73] M. Sale, P. Rizzo, and A. Marzani. "Semi-analytical formulation for the guided waves-based reconstruction of elastic moduli". In: *Mechanical Systems and Signal Processing* 25.6 (2011), pp. 2241–2256.

[74] A. Marzani and L. de Marchi. "Characterization of the elastic moduli in composite plates via dispersive guided waves data and genetic algorithms". In: *Journal of Intelligent Material Systems and Structures* 24.17 (2013), pp. 2135–2147.

[75] R. Cui and F. L. di Scalea. "On the identification of the elastic properties of composites by ultrasonic guided waves and optimization algorithm". In: *Composite Structures* 223.110969 (2019).

[76] C. Kassapoglou. "Modeling the stiffness and strength of aerospace structural elements". In: *Polymer Composites in the Aerospace Industry* (2015), pp. 117–154.

[77] A. Zaal. "Feasibility evaluation of a non-destructive estimation of material properties of FRC structures using ultrasonic guided waves". MA thesis. Delf University of Techology, 2021.

[78] R. Pro. *RS PRO SDG1032X Waveform Generator 30MHz RS Calibration*. URL: `https://uk.rs-online.com/web/p/arbitrary-waveform-generators/1882691`.

[79] F. Systems. *WMA-300 High speed high voltage amplifier*. URL: `http://www.falco-systems.com/High_voltage_amplifier_WMA-300.html`.

[80] V. Systeme. *VS600-Z1*. URL: `https://www.vallen.de/sensors/high-frequencs-sensors-400-khz/vs600-z1/`.

[81] A. C. S. .-. A. Group. *S1803 – Longitudinal Wave DPC Transducer 100 kHz*. URL: `https://acs-international.com/instruments/transducers/low-frequency-50-to-300-khz/dry-point-contact/single/s1803/`.

[82] V. Systeme. *AEP5, AEP5H*. URL: `https://www.vallen.de/allgemein/aep5-aep5h/`.

[83] V. Systeme. *Multi-Channel Systems*. URL: https://www.vallen.de/products/multi-channel-systems/.

[84] L. P. Pahlavan. "Wave Propagation in Thin-Walled Composite Structures: Application to Structural Health Monitoring". PhD thesis. Delft University of Technology, 2012.

A
Methodology

The final structure of the matrices $\boldsymbol{C_S}$ and $\boldsymbol{C_A}$ can be found in equations A.1 and A.2 respectively. The detailed structure of equation 3.14 can be found in equation A.3.

$$\begin{bmatrix}
c_{S_0,\theta_1,\omega_1,A_{11}} & c_{S_0,\theta_1,\omega_1,A_{12}} & c_{S_0,\theta_1,\omega_1,A_{16}} & \cdots & c_{S_0,\theta_1,\omega_1,D_{66}} \\
c_{S_0,\theta_1,\omega_2,A_{11}} & c_{S_0,\theta_1,\omega_2,A_{12}} & c_{S_0,\theta_1,\omega_2,A_{16}} & \cdots & c_{S_0,\theta_1,\omega_2,D_{66}} \\
c_{S_0,\theta_1,\omega_j,A_{11}} & c_{S_0,\theta_1,\omega_j,A_{12}} & c_{S_0,\theta_1,\omega_j,A_{16}} & \cdots & c_{S_0,\theta_1,\omega_j,D_{66}} \\
\vdots & \vdots & \vdots & & \vdots \\
c_{S_0,\theta_1,\omega_f,A_{11}} & c_{S_0,\theta_1,\omega_f,A_{12}} & c_{S_0,\theta_1,\omega_f,A_{16}} & \cdots & c_{S_0,\theta_1,\omega_f,D_{66}} \\
c_{S_0,\theta_2,\omega_1,A_{11}} & c_{S_0,\theta_2,\omega_1,A_{12}} & c_{S_0,\theta_2,\omega_1,A_{16}} & \cdots & c_{S_0,\theta_2,\omega_1,D_{66}} \\
c_{S_0,\theta_2,\omega_2,A_{11}} & c_{S_0,\theta_2,\omega_2,A_{12}} & c_{S_0,\theta_2,\omega_2,A_{16}} & \cdots & c_{S_0,\theta_2,\omega_2,D_{66}} \\
c_{S_0,\theta_2,\omega_j,A_{11}} & c_{S_0,\theta_2,\omega_j,A_{12}} & c_{S_0,\theta_2,\omega_j,A_{16}} & \cdots & c_{S_0,\theta_2,\omega_j,D_{66}} \\
\vdots & \vdots & \vdots & & \vdots \\
c_{S_0,\theta_2,\omega_f,A_{11}} & c_{S_0,\theta_2,\omega_f,A_{12}} & c_{S_0,\theta_2,\omega_f,A_{16}} & \cdots & c_{S_0,\theta_2,\omega_f,D_{66}} \\
c_{S_0,\theta_i,\omega_1,A_{11}} & c_{S_0,\theta_i,\omega_1,A_{12}} & c_{S_0,\theta_i,\omega_1,A_{16}} & \cdots & c_{S_0,\theta_i,\omega_1,D_{66}} \\
c_{S_0,\theta_i,\omega_2,A_{11}} & c_{S_0,\theta_i,\omega_2,A_{12}} & c_{S_0,\theta_i,\omega_2,A_{16}} & \cdots & c_{S_0,\theta_i,\omega_2,D_{66}} \\
c_{S_0,\theta_i,\omega_j,A_{11}} & c_{S_0,\theta_i,\omega_j,A_{12}} & c_{S_0,\theta_i,\omega_j,A_{16}} & \cdots & c_{S_0,\theta_i,\omega_j,D_{66}} \\
\vdots & \vdots & \vdots & & \vdots \\
c_{S_0,\theta_i,\omega_f,A_{11}} & c_{S_0,\theta_i,\omega_f,A_{12}} & c_{S_0,\theta_i,\omega_f,A_{16}} & \cdots & c_{S_0,\theta_i,\omega_f,D_{66}} \\
c_{S_0,\theta_d,\omega_1,A_{11}} & c_{S_0,\theta_d,\omega_1,A_{12}} & c_{S_0,\theta_d,\omega_1,A_{16}} & \cdots & c_{S_0,\theta_d,\omega_1,D_{66}} \\
c_{S_0,\theta_d,\omega_2,A_{11}} & c_{S_0,\theta_d,\omega_2,A_{12}} & c_{S_0,\theta_d,\omega_2,A_{16}} & \cdots & c_{S_0,\theta_d,\omega_2,D_{66}} \\
c_{S_0,\theta_d,\omega_j,A_{11}} & c_{S_0,\theta_d,\omega_j,A_{12}} & c_{S_0,\theta_d,\omega_j,A_{16}} & \cdots & c_{S_0,\theta_d,\omega_j,D_{66}} \\
\vdots & \vdots & \vdots & & \vdots \\
c_{S_0,\theta_d,\omega_f,A_{11}} & c_{S_0,\theta_d,\omega_f,A_{12}} & c_{S_0,\theta_d,\omega_f,A_{16}} & \cdots & c_{S_0,\theta_d,\omega_f,D_{66}}
\end{bmatrix} \tag{A.1}$$

$$\begin{bmatrix}
c_{A_0,\theta_1,\omega_1,A_{11}} & c_{A_0,\theta_1,\omega_1,A_{12}} & c_{A_0,\theta_1,\omega_1,A_{16}} & \cdots & c_{A_0,\theta_1,\omega_1,D_{66}} \\
c_{A_0,\theta_1,\omega_2,A_{11}} & c_{A_0,\theta_1,\omega_2,A_{12}} & c_{A_0,\theta_1,\omega_2,A_{16}} & \cdots & c_{A_0,\theta_1,\omega_2,D_{66}} \\
c_{A_0,\theta_1,\omega_j,A_{11}} & c_{A_0,\theta_1,\omega_j,A_{12}} & c_{A_0,\theta_1,\omega_j,A_{16}} & \cdots & c_{A_0,\theta_1,\omega_j,D_{66}} \\
\vdots & \vdots & \vdots & & \vdots \\
c_{A_0,\theta_1,\omega_f,A_{11}} & c_{A_0,\theta_1,\omega_f,A_{12}} & c_{A_0,\theta_1,\omega_f,A_{16}} & \cdots & c_{A_0,\theta_1,\omega_f,D_{66}} \\
c_{A_0,\theta_2,\omega_1,A_{11}} & c_{A_0,\theta_2,\omega_1,A_{12}} & c_{A_0,\theta_2,\omega_1,A_{16}} & \cdots & c_{A_0,\theta_2,\omega_1,D_{66}} \\
c_{A_0,\theta_2,\omega_2,A_{11}} & c_{A_0,\theta_2,\omega_2,A_{12}} & c_{A_0,\theta_2,\omega_2,A_{16}} & \cdots & c_{A_0,\theta_2,\omega_2,D_{66}} \\
c_{A_0,\theta_2,\omega_j,A_{11}} & c_{A_0,\theta_2,\omega_j,A_{12}} & c_{A_0,\theta_2,\omega_j,A_{16}} & \cdots & c_{A_0,\theta_2,\omega_j,D_{66}} \\
\vdots & \vdots & \vdots & & \vdots \\
c_{A_0,\theta_2,\omega_f,A_{11}} & c_{A_0,\theta_2,\omega_f,A_{12}} & c_{A_0,\theta_2,\omega_f,A_{16}} & \cdots & c_{A_0,\theta_2,\omega_f,D_{66}} \\
c_{A_0,\theta_i,\omega_1,A_{11}} & c_{A_0,\theta_i,\omega_1,A_{12}} & c_{A_0,\theta_i,\omega_1,A_{16}} & \cdots & c_{A_0,\theta_i,\omega_1,D_{66}} \\
c_{A_0,\theta_i,\omega_2,A_{11}} & c_{A_0,\theta_i,\omega_2,A_{12}} & c_{A_0,\theta_i,\omega_2,A_{16}} & \cdots & c_{A_0,\theta_i,\omega_2,D_{66}} \\
c_{A_0,\theta_i,\omega_j,A_{11}} & c_{A_0,\theta_i,\omega_j,A_{12}} & c_{A_0,\theta_i,\omega_j,A_{16}} & \cdots & c_{A_0,\theta_i,\omega_j,D_{66}} \\
\vdots & \vdots & \vdots & & \vdots \\
c_{A_0,\theta_i,\omega_f,A_{11}} & c_{A_0,\theta_i,\omega_f,A_{12}} & c_{A_0,\theta_i,\omega_f,A_{16}} & \cdots & c_{A_0,\theta_d,\omega_f,D_{66}} \\
c_{A_0,\theta_d,\omega_1,A_{11}} & c_{A_0,\theta_d,\omega_1,A_{12}} & c_{A_0,\theta_d,\omega_1,A_{16}} & \cdots & c_{A_0,\theta_d,\omega_1,D_{66}} \\
c_{A_0,\theta_d,\omega_2,A_{11}} & c_{A_0,\theta_d,\omega_2,A_{12}} & c_{A_0,\theta_d,\omega_2,A_{16}} & \cdots & c_{A_0,\theta_d,\omega_2,D_{66}} \\
c_{A_0,\theta_d,\omega_j,A_{11}} & c_{A_0,\theta_d,\omega_j,A_{12}} & c_{A_0,\theta_d,\omega_j,A_{16}} & \cdots & c_{A_0,\theta_i,\omega_j,D_{66}} \\
\vdots & \vdots & \vdots & & \vdots \\
c_{A_0,\theta_d,\omega_f,A_{11}} & c_{A_0,\theta_d,\omega_f,A_{12}} & c_{A_0,\theta_d,\omega_f,A_{16}} & \cdots & c_{A_0,\theta_d,\omega_f,D_{66}}
\end{bmatrix} \tag{A.2}$$

$$
\begin{bmatrix}
c_{S_0,\theta_1,\omega_1,A_{11}} & c_{S_0,\theta_1,\omega_1,A_{12}} & c_{S_0,\theta_1,\omega_1,A_{16}} & \cdots & c_{S_0,\theta_1,\omega_1,D_{66}} \\
c_{S_0,\theta_1,\omega_2,A_{11}} & c_{S_0,\theta_1,\omega_2,A_{12}} & c_{S_0,\theta_1,\omega_2,A_{16}} & \cdots & c_{S_0,\theta_1,\omega_2,D_{66}} \\
c_{S_0,\theta_1,\omega_j,A_{11}} & c_{S_0,\theta_1,\omega_j,A_{12}} & c_{S_0,\theta_1,\omega_j,A_{16}} & \cdots & c_{S_0,\theta_1,\omega_j,D_{66}} \\
\vdots & \vdots & \vdots & & \vdots \\
c_{S_0,\theta_1,\omega_f,A_{11}} & c_{S_0,\theta_1,\omega_f,A_{12}} & c_{S_0,\theta_1,\omega_f,A_{16}} & \cdots & c_{S_0,\theta_1,\omega_f,D_{66}} \\
c_{S_0,\theta_2,\omega_1,A_{11}} & c_{S_0,\theta_2,\omega_1,A_{12}} & c_{S_0,\theta_2,\omega_1,A_{16}} & \cdots & c_{S_0,\theta_2,\omega_1,D_{66}} \\
c_{S_0,\theta_2,\omega_2,A_{11}} & c_{S_0,\theta_2,\omega_2,A_{12}} & c_{S_0,\theta_2,\omega_2,A_{16}} & \cdots & c_{S_0,\theta_2,\omega_2,D_{66}} \\
c_{S_0,\theta_2,\omega_j,A_{11}} & c_{S_0,\theta_2,\omega_j,A_{12}} & c_{S_0,\theta_2,\omega_j,A_{16}} & \cdots & c_{S_0,\theta_2,\omega_j,D_{66}} \\
\vdots & \vdots & \vdots & & \vdots \\
c_{S_0,\theta_2,\omega_f,A_{11}} & c_{S_0,\theta_2,\omega_f,A_{12}} & c_{S_0,\theta_2,\omega_f,A_{16}} & \cdots & c_{S_0,\theta_2,\omega_f,D_{66}} \\
c_{S_0,\theta_i,\omega_1,A_{11}} & c_{S_0,\theta_i,\omega_1,A_{12}} & c_{S_0,\theta_i,\omega_1,A_{16}} & \cdots & c_{S_0,\theta_i,\omega_1,D_{66}} \\
c_{S_0,\theta_i,\omega_2,A_{11}} & c_{S_0,\theta_i,\omega_2,A_{12}} & c_{S_0,\theta_i,\omega_2,A_{16}} & \cdots & c_{S_0,\theta_i,\omega_2,D_{66}} \\
c_{S_0,\theta_i,\omega_j,A_{11}} & c_{S_0,\theta_i,\omega_j,A_{12}} & c_{S_0,\theta_i,\omega_j,A_{16}} & \cdots & c_{S_0,\theta_i,\omega_j,D_{66}} \\
\vdots & \vdots & \vdots & & \vdots \\
c_{S_0,\theta_i,\omega_f,A_{11}} & c_{S_0,\theta_i,\omega_f,A_{12}} & c_{S_0,\theta_i,\omega_f,A_{16}} & \cdots & c_{S_0,\theta_i,\omega_f,D_{66}} \\
c_{S_0,\theta_d,\omega_1,A_{11}} & c_{S_0,\theta_d,\omega_1,A_{12}} & c_{S_0,\theta_d,\omega_1,A_{16}} & \cdots & c_{S_0,\theta_d,\omega_1,D_{66}} \\
c_{S_0,\theta_d,\omega_2,A_{11}} & c_{S_0,\theta_d,\omega_2,A_{12}} & c_{S_0,\theta_d,\omega_2,A_{16}} & \cdots & c_{S_0,\theta_d,\omega_2,D_{66}} \\
c_{S_0,\theta_d,\omega_j,A_{11}} & c_{S_0,\theta_d,\omega_j,A_{12}} & c_{S_0,\theta_d,\omega_j,A_{16}} & \cdots & c_{S_0,\theta_d,\omega_j,D_{66}} \\
\vdots & \vdots & \vdots & & \vdots \\
c_{S_0,\theta_d,\omega_f,A_{11}} & c_{S_0,\theta_d,\omega_f,A_{12}} & c_{S_0,\theta_d,\omega_f,A_{16}} & \cdots & c_{S_0,\theta_d,\omega_f,D_{66}} \\
c_{A_0,\theta_1,\omega_1,A_{11}} & c_{A_0,\theta_1,\omega_1,A_{12}} & c_{A_0,\theta_1,\omega_1,A_{16}} & \cdots & c_{A_0,\theta_1,\omega_1,D_{66}} \\
c_{A_0,\theta_1,\omega_2,A_{11}} & c_{A_0,\theta_1,\omega_2,A_{12}} & c_{A_0,\theta_1,\omega_2,A_{16}} & \cdots & c_{A_0,\theta_1,\omega_2,D_{66}} \\
c_{A_0,\theta_1,\omega_j,A_{11}} & c_{A_0,\theta_1,\omega_j,A_{12}} & c_{A_0,\theta_1,\omega_j,A_{16}} & \cdots & c_{A_0,\theta_1,\omega_j,D_{66}} \\
\vdots & \vdots & \vdots & & \vdots \\
c_{A_0,\theta_1,\omega_f,A_{11}} & c_{A_0,\theta_1,\omega_f,A_{12}} & c_{A_0,\theta_1,\omega_f,A_{16}} & \cdots & c_{A_0,\theta_1,\omega_f,D_{66}} \\
c_{A_0,\theta_2,\omega_1,A_{11}} & c_{A_0,\theta_2,\omega_1,A_{12}} & c_{A_0,\theta_2,\omega_1,A_{16}} & \cdots & c_{A_0,\theta_2,\omega_1,D_{66}} \\
c_{A_0,\theta_2,\omega_2,A_{11}} & c_{A_0,\theta_2,\omega_2,A_{12}} & c_{A_0,\theta_2,\omega_2,A_{16}} & \cdots & c_{A_0,\theta_2,\omega_2,D_{66}} \\
c_{A_0,\theta_2,\omega_j,A_{11}} & c_{A_0,\theta_2,\omega_j,A_{12}} & c_{A_0,\theta_2,\omega_j,A_{16}} & \cdots & c_{A_0,\theta_2,\omega_j,D_{66}} \\
\vdots & \vdots & \vdots & & \vdots \\
c_{A_0,\theta_2,\omega_f,A_{11}} & c_{A_0,\theta_2,\omega_f,A_{12}} & c_{A_0,\theta_2,\omega_f,A_{16}} & \cdots & c_{A_0,\theta_2,\omega_f,D_{66}} \\
c_{A_0,\theta_i,\omega_1,A_{11}} & c_{A_0,\theta_i,\omega_1,A_{12}} & c_{A_0,\theta_i,\omega_1,A_{16}} & \cdots & c_{A_0,\theta_i,\omega_1,D_{66}} \\
c_{A_0,\theta_i,\omega_2,A_{11}} & c_{A_0,\theta_i,\omega_2,A_{12}} & c_{A_0,\theta_i,\omega_2,A_{16}} & \cdots & c_{A_0,\theta_i,\omega_2,D_{66}} \\
c_{A_0,\theta_i,\omega_j,A_{11}} & c_{A_0,\theta_i,\omega_j,A_{12}} & c_{A_0,\theta_i,\omega_j,A_{16}} & \cdots & c_{A_0,\theta_i,\omega_j,D_{66}} \\
\vdots & \vdots & \vdots & & \vdots \\
c_{A_0,\theta_i,\omega_f,A_{11}} & c_{A_0,\theta_i,\omega_f,A_{12}} & c_{A_0,\theta_i,\omega_f,A_{16}} & \cdots & c_{A_0,\theta_i,\omega_f,D_{66}} \\
c_{A_0,\theta_d,\omega_1,A_{11}} & c_{A_0,\theta_d,\omega_1,A_{12}} & c_{A_0,\theta_d,\omega_1,A_{16}} & \cdots & c_{A_0,\theta_d,\omega_1,D_{66}} \\
c_{A_0,\theta_d,\omega_2,A_{11}} & c_{A_0,\theta_d,\omega_2,A_{12}} & c_{A_0,\theta_d,\omega_2,A_{16}} & \cdots & c_{A_0,\theta_d,\omega_2,D_{66}} \\
c_{A_0,\theta_d,\omega_j,A_{11}} & c_{A_0,\theta_d,\omega_j,A_{12}} & c_{A_0,\theta_d,\omega_j,A_{16}} & \cdots & c_{A_0,\theta_d,\omega_j,D_{66}} \\
\vdots & \vdots & \vdots & & \vdots \\
c_{A_0,\theta_d,\omega_f,A_{11}} & c_{A_0,\theta_d,\omega_f,A_{12}} & c_{A_0,\theta_d,\omega_f,A_{16}} & \cdots & c_{A_0,\theta_d,\omega_f,D_{66}}
\end{bmatrix}
\begin{bmatrix}
A_{11} \\ A_{12} \\ A_{16} \\ \vdots \\ \vdots \\ \vdots \\ D_{66}
\end{bmatrix}
=
\begin{bmatrix}
c^2_{gS_0,\theta_1\omega_1} \\ c^2_{gS_0,\theta_1\omega_2} \\ c^2_{gS_0,\theta_1\omega_j} \\ \vdots \\ c^2_{gS_0,\theta_1\omega_f} \\
c^2_{gS_0,\theta_2\omega_1} \\ c^2_{gS_0,\theta_2\omega_2} \\ c^2_{gS_0,\theta_2\omega_j} \\ \vdots \\ c^2_{gS_0,\theta_2\omega_f} \\
c^2_{gS_0,\theta_i\omega_1} \\ c^2_{gS_0,\theta_i\omega_2} \\ c^2_{gS_0,\theta_i\omega_j} \\ \vdots \\ c^2_{gS_0,\theta_i\omega_f} \\
c^2_{gS_0,\theta_d\omega_1} \\ c^2_{gS_0,\theta_d\omega_2} \\ c^2_{gS_0,\theta_d\omega_j} \\ \vdots \\ c^2_{gS_0,\theta_d\omega_f} \\
c^2_{gA_0,\theta_1\omega_1} \\ c^2_{gA_0,\theta_1\omega_2} \\ c^2_{gA_0,\theta_1\omega_j} \\ \vdots \\ c^2_{gA_0,\theta_1\omega_f} \\
c^2_{gA_0,\theta_2\omega_1} \\ c^2_{gA_0,\theta_2\omega_2} \\ c^2_{gA_0,\theta_2\omega_j} \\ \vdots \\ c^2_{gA_0,\theta_2\omega_f} \\
c^2_{gA_0,\theta_i\omega_1} \\ c^2_{gA_0,\theta_i\omega_2} \\ c^2_{gA_0,\theta_i\omega_j} \\ \vdots \\ c^2_{gA_0,\theta_i\omega_f} \\
c^2_{gA_0,\theta_d\omega_1} \\ c^2_{gA_0,\theta_d\omega_2} \\ c^2_{gA_0,\theta_d\omega_j} \\ \vdots \\ c^2_{gA_0,\theta_d\omega_f}
\end{bmatrix}
\tag{A.3}
$$

B

SAFE method

.

The SAFE method uses a finite element discretization of the cross-section to describe the mode shapes of the wave propagation in the x-direction. A schematic of the SAFE method is given in figure 2.9. The displacement along the wave propagation direction is described in an analytical manner as harmonic exponential functions. An undamped system described using three-node elements is assumed in this description. At each node the harmonic displacement, stress, and strain are formulated by the equations in B.1. The strain-displacement relation can be written as equation B.2, where all directional contributions are taken into account by the matrices in B.3.

$$\boldsymbol{u} = [u_x u_y u_z]^{\mathrm{T}}, \quad \boldsymbol{\sigma} = [\sigma_x \sigma_y \sigma_z \sigma_{yz} \sigma_{xz} \sigma_{xy}]^{\mathrm{T}}, \quad \boldsymbol{\varepsilon} = [\varepsilon_x \varepsilon_y \varepsilon_z \gamma_{yz} \gamma_{xz} \gamma_{xy}]^{\mathrm{T}} \tag{B.1}$$

$$\boldsymbol{\varepsilon} = \left[\boldsymbol{L}_x \frac{\partial}{\partial x} + \boldsymbol{L}_y \frac{\partial}{\partial y} + \boldsymbol{L}_z \frac{\partial}{\partial z} \right] \boldsymbol{u} \tag{B.2}$$

$$\boldsymbol{L}_x = \begin{bmatrix} 1 & 0 & 0 \\ 0 & 0 & 0 \\ 0 & 0 & 0 \\ 0 & 0 & 0 \\ 0 & 0 & 1 \\ 0 & 1 & 0 \end{bmatrix}, \quad \boldsymbol{L}_y = \begin{bmatrix} 0 & 0 & 0 \\ 0 & 1 & 0 \\ 0 & 0 & 0 \\ 0 & 0 & 1 \\ 0 & 0 & 0 \\ 1 & 0 & 0 \end{bmatrix}, \quad \boldsymbol{L}_z = \begin{bmatrix} 0 & 0 & 0 \\ 0 & 0 & 0 \\ 0 & 0 & 1 \\ 0 & 1 & 0 \\ 1 & 0 & 0 \\ 0 & 0 & 0 \end{bmatrix} \tag{B.3}$$

The equation of motion in the cross-section is expressed by Hamilton's equation [72], expressed as equation B.4 where the strain energy Φ and kinetic energy K are given by equations B.5 and B.6, respectively. In these equations ρ, $\dot{\mathbf{u}}$, $\boldsymbol{C}$, and V are the density, displacement time derivative, stiffness matrix, and volume respectively.

$$\delta H = \int_{t_1}^{t_2} \delta(\Phi - K)\mathrm{d}t = 0 \tag{B.4}$$

$$\Phi = \frac{1}{2} \int_V \boldsymbol{\varepsilon}^{\mathrm{T}} \boldsymbol{C} \boldsymbol{\varepsilon} \mathrm{d}V \tag{B.5}$$

$$K = \frac{1}{2} \int_V \dot{\boldsymbol{u}}^{\mathrm{T}} \rho \dot{\boldsymbol{u}} \mathrm{d}V \tag{B.6}$$

By substituting equations B.5 and B.6 into equation B.4 and integrating by parts, the Hamilton's can be written as equation B.7. The SAFE method assumes the displacement to be harmonic along the propagation direction, hence $\boldsymbol{u}$ can be written as equation B.8, where ξ and ω are the wavenumber and frequency respectively.

$$\int_{t_1}^{t_2}\left[\int_V \delta\left(\boldsymbol{\varepsilon}^{\mathrm{T}}\right)\mathbf{C}\boldsymbol{\varepsilon}\mathrm{d}V+\int_V \delta\left(\boldsymbol{u}^{\mathrm{T}}\right)\rho\ddot{\boldsymbol{u}}\mathrm{d}V\right]\mathrm{d}t=0 \tag{B.7}$$

$$\boldsymbol{u}(x,y,z,t)=\begin{bmatrix} u_x(x,y,z,t)\\ u_y(x,y,z,t)\\ u_z(x,y,z,t)\end{bmatrix}=\begin{bmatrix} U_x(y,z)\\ U_y(y,z)\\ U_z(y,z)\end{bmatrix}\mathrm{e}^{\mathrm{i}(\xi x-\omega t)} \tag{B.8}$$

Using the finite element discretization of the cross-section Ω the waveguide's cross-sectional domain is represented by a system of finite elements with domain Ω_e, where e denotes the element number. The displacement vector in equation B.8 can be rewritten in its discretized form as function of the shape function $N_k(y,z)$ and unknown nodal displacements U_{ij} resulting in equation B.9 where the matrix $\boldsymbol{N}(y,y)$ contains the shape functions (equation B.10) and vector $\boldsymbol{q}^{(e)}$ contains the element's nodal displacements (equation B.11). In these equations n denotes the number of nodes per element.

$$\boldsymbol{u}^{(e)}(x,y,z,t)=\begin{bmatrix} \sum_{k=1}^{n} N_k(y,z)U_{xk}\\ \sum_{k=1}^{n} N_k(y,z)U_{yk}\\ \sum_{k=1}^{n} N_k(y,z)U_{zk}\end{bmatrix}^{(e)}\mathrm{e}^{\mathrm{i}(\xi x-\omega t)}=\boldsymbol{N}(y,z)\boldsymbol{q}^{(e)}\mathrm{e}^{\mathrm{i}(\xi x-\omega t)} \tag{B.9}$$

$$\boldsymbol{N}(y,z)=\begin{bmatrix} N_1 & & & N_2 & & & \ddots & & & N_n & & \\ & N_1 & & & N_2 & & & \ddots & & & N_n & \\ & & N_1 & & & N_2 & & & \ddots & & & N_n \end{bmatrix} \tag{B.10}$$

$$\boldsymbol{q}^{(e)}=\begin{bmatrix} U_{x1} & U_{y1} & U_{z1} & U_{x2} & U_{y2} & U_{z2} & \cdots & \cdots & \cdots & U_{xn} & U_{yn} & U_{zn}\end{bmatrix}^{\mathrm{T}} \tag{B.11}$$

Similarly, the strain-displacement relation in an element can be written as function of the nodal displacement as equation B.12, where $\boldsymbol{B}_1=\boldsymbol{L}_y\boldsymbol{N}_{,y}+\boldsymbol{L}_z\boldsymbol{N}_{,z}$, $\boldsymbol{B}_2=\boldsymbol{L}_x N$, and $\boldsymbol{N}_{,y}$ and $\boldsymbol{N}_{,z}$ are derivatives of the shape function matrix B.10 with respect to y and z, respectively. $\boldsymbol{B}_1$ is related to the planar deformations, $\boldsymbol{B}_2$ is related to the out-of-plane deformations.

$$\boldsymbol{\varepsilon}^{(e)}=\left[\boldsymbol{L}_x\frac{\partial}{\partial x}+\boldsymbol{L}_y\frac{\partial}{\partial y}+\boldsymbol{L}_z\frac{\partial}{\partial z}\right]\boldsymbol{N}(y,z)\boldsymbol{q}^{(e)}\mathrm{e}^{\mathrm{i}(\xi x-\omega t)}=\left(\boldsymbol{B}_1+\mathrm{i}\xi\boldsymbol{B}_2\right)\boldsymbol{q}^{(e)}\mathrm{e}^{\mathrm{i}(\xi x-\omega t)} \tag{B.12}$$

The discrete form of the Hamilton's equation of B.7 can be written as equation B.13, where n_{el} is the total number of elements, $\boldsymbol{C}_e$ and ρ_e are the element's stiffness matrix and density respectively. By substituting equation B.12 into the strain- and kinetic energy terms of equation B.13 and additionally by several algebraic manipulations, the resulting equation for both energy contributions are B.14 and B.15. In these equations the integration takes place over the element's cross-sectional domain Ω_e

$$\int_{t_1}^{t_2}\left\{\bigcup_{e=1}^{n_{\mathrm{el}}}\left[\int_{V_e}\delta\left(\boldsymbol{\varepsilon}^{(e)^{\mathrm{T}}}\right)\boldsymbol{C}_e\boldsymbol{\varepsilon}^{(e)}\mathrm{d}V_e+\int_{V_e}\delta\left(\boldsymbol{u}^{(e)^{\mathrm{T}}}\right)\rho_e\ddot{\boldsymbol{u}}^{(e)}\mathrm{d}V_e\right]\right\}\mathrm{d}t=0 \tag{B.13}$$

$$\int_{V_e}\delta\left(\boldsymbol{\varepsilon}^{(e)^{\mathrm{T}}}\right)\boldsymbol{C}_e\boldsymbol{\varepsilon}^{(e)}\mathrm{d}V_e=\delta\boldsymbol{q}^{(e)^{\mathrm{T}}}\int_{\Omega_e}\left[\boldsymbol{B}_1^{\mathrm{T}}\boldsymbol{C}_e\boldsymbol{B}_1-\mathrm{i}\xi\boldsymbol{B}_2^{\mathrm{T}}\boldsymbol{C}_e\boldsymbol{B}_1+\mathrm{i}\xi\boldsymbol{B}_1^{\mathrm{T}}\boldsymbol{C}_e\boldsymbol{B}_2+\xi^2\boldsymbol{B}_2^{\mathrm{T}}\boldsymbol{C}_e\boldsymbol{B}_2\right]\mathrm{d}\Omega_e\boldsymbol{q}^{(e)} \tag{B.14}$$

$$\int_{V_e}\delta\left(\boldsymbol{u}^{(e)^{\mathrm{T}}}\right)\rho_e\ddot{\boldsymbol{u}}^{(e)}\mathrm{d}V_e=-\omega^2\delta\boldsymbol{q}^{(e)^{\mathrm{T}}}\int_{\Omega_e}\boldsymbol{N}^{\mathrm{T}}\rho_e\boldsymbol{N}\mathrm{d}\Omega_e\boldsymbol{q}^{(e)} \tag{B.15}$$

Substituting equations B.14 and B.15 into equation B.13 yields equation B.16 where the element's stiffness $\boldsymbol{k}_i^{(e)}$ and mass $\boldsymbol{m}^{(e)}$ contributions are given by the equations in B.17.

$$\int_{t_1}^{t_2}\left\{\bigcup_{e=1}^{n_{\mathrm{cl}}}\delta\boldsymbol{q}^{(e)\mathrm{T}}\left[\boldsymbol{k}_1^{(e)}+\mathrm{i}\xi\boldsymbol{k}_2^{(e)}+\xi^2\boldsymbol{k}_3^{(e)}-\omega^2\boldsymbol{m}^{(e)}\right]\boldsymbol{q}^{(e)}\right\}\mathrm{d}t=0 \tag{B.16}$$

$$\begin{aligned}\boldsymbol{k}_1^{(e)}&=\int_{\Omega_e}\left[\boldsymbol{B}_1^{\mathrm{T}}\boldsymbol{C}_e\boldsymbol{B}_1\right]\mathrm{d}\Omega_e,\quad \boldsymbol{k}_2^{(e)}=\int_{\Omega_e}\left[\boldsymbol{B}_1^{\mathrm{T}}\boldsymbol{C}_e\boldsymbol{B}_2-\boldsymbol{B}_2^{\mathrm{T}}\widetilde{\mathbf{C}}_e\boldsymbol{B}_1\right]\mathrm{d}\Omega_e,\\ \boldsymbol{k}_3^{(e)}&=\int_{\Omega_e}\left[\boldsymbol{B}_2^{\mathrm{T}}\boldsymbol{C}_e\boldsymbol{B}_2\right]\mathrm{d}\Omega_e,\quad \boldsymbol{m}^{(e)}=\int_{\Omega_e}\boldsymbol{N}^{\mathrm{T}}\rho_e\boldsymbol{N}\mathrm{d}\Omega_e\end{aligned} \tag{B.17}$$

Applying the FEM assembling procedure to equation B.16 yields equation B.18 where $\boldsymbol{U}$ contains the unknown nodal displacement, the summed elemental stiffness and mass contribution are given by the equations in B.19.

$$\int_{t_1}^{t_2}\left\{\delta\boldsymbol{U}^{\mathrm{T}}\left[\boldsymbol{K}_1+\mathrm{i}\xi\boldsymbol{K}_2+\xi^2\boldsymbol{K}_3-\omega^2\boldsymbol{M}\right]\boldsymbol{U}\right\}\mathrm{d}t=0 \tag{B.18}$$

$$\boldsymbol{K}_1=\bigcup_{e=1}^{n_{\mathrm{cl}}}\boldsymbol{k}_1^{(e)},\quad \boldsymbol{K}_2=\bigcup_{e=1}^{n_{\mathrm{cl}}}\boldsymbol{k}_2^{(e)},\quad \boldsymbol{K}_3=\bigcup_{e=1}^{n_{\mathrm{cl}}}\boldsymbol{k}_3^{(e)},\quad \boldsymbol{M}=\bigcup_{e=1}^{n_{\mathrm{cl}}}\boldsymbol{m}^{(e)} \tag{B.19}$$

Here, $\boldsymbol{K}_1$ is dependent on $\boldsymbol{B}_1$ and is thus related to generalized plane strain behaviour or cross-sectional warpage, $\boldsymbol{K}_3$ is related to $\boldsymbol{B}_2$ and models the out-of-plane deformations, and $\boldsymbol{K}_2$ couples the cross-sectional warpage to the out-of-plane deformations. To obtain the non-trivial solution, equation B.18 must hold regardless the value of $\delta\boldsymbol{U}$. Equation B.16 therefore can be reduced to the homogeneous general wave equation given in equation B.20, where subscript M indicates the number of total degrees of freedom of the system.

$$\left[\boldsymbol{K}_1+\mathrm{i}\xi\boldsymbol{K}_2+\xi^2\boldsymbol{K}_3-\omega^2\boldsymbol{M}\right]_M\boldsymbol{U}=0 \tag{B.20}$$

Equation B.20 can be rewritten as a first-order eigensystem by doubling its algebraic size to $2M$, giving equation B.21. For a given frequency ω_i the dispersive properties (wavenumbers ξ and nodal displacements $\boldsymbol{U}$) of the waveguide can then be obtained as eigenvalues ξ^m $(m=1,2,3,\cdots,2M)$ and the corresponding right $\boldsymbol{U}_R^m$ and left $\boldsymbol{U}_L^m$ eigenvectors, corresponding to the forward and backforward modes respectively. Here, real, complex and purely imaginary eigenvalues exist, representing propagative, evanescent, and standing modes respectively [73].

$$\left(\begin{bmatrix}\mathbf{0} & \boldsymbol{K}_3-\omega^2\boldsymbol{M}\\ \boldsymbol{K}_3-\omega^2\boldsymbol{M} & i\boldsymbol{K}_2\end{bmatrix}-\xi\begin{bmatrix}\boldsymbol{K}_3-\omega^2\boldsymbol{M} & \mathbf{0}\\ \mathbf{0} & -\boldsymbol{K}_1\end{bmatrix}\right)_{2M}\begin{bmatrix}\boldsymbol{U}\\ \xi\boldsymbol{U}\end{bmatrix}=\begin{bmatrix}\mathbf{0}\\ \mathbf{0}\end{bmatrix} \tag{B.21}$$

Furthermore, for each frequency ω_i the group velocity of the right propagating waves ($\xi^m>0$) can be obtained from equation B.20. Therefore, first the derivative of B.20 with respect to the wavenumber has to be calculated by equation B.22 where $\boldsymbol{K}(\xi)=\boldsymbol{K}_1+i\xi\boldsymbol{K}_2+\xi^2\boldsymbol{K}_3$. Pre-multiplying equation B.22 by the transpose of the left eigenvector gives equation B.23 and since the group velocity can be found as the partial derivative between the wave frequency and wavenumber, this can be obtained using equation B.24. From this relation, the group velocities can be calculated for each individual solution (ω,ξ) of the dispersion relation.

$$\frac{\partial}{\partial\xi}\left(\left[\boldsymbol{K}(\xi)-\omega^2\boldsymbol{M}\right]\boldsymbol{U}_R\right)=0 \tag{B.22}$$

$$\boldsymbol{U}_L^{\mathrm{T}}\left[\frac{\partial}{\partial\xi}\boldsymbol{K}(\xi)-2\omega\frac{\partial\omega}{\partial\xi}\boldsymbol{M}\right]\boldsymbol{U}_R=0 \tag{B.23}$$

$$c_g=\frac{\partial\omega}{\partial\xi}=\frac{\boldsymbol{U}_L^{\mathrm{T}}\left(i\boldsymbol{K}_2+2\xi\boldsymbol{K}_3\right)\boldsymbol{U}_R}{2\omega\boldsymbol{U}_L^{\mathrm{T}}\boldsymbol{M}\boldsymbol{U}_R} \tag{B.24}$$

C
Signal processing

In figure C.1 the raw signal recorded corresponding to a measurement performed on plate 1.2 is shown. The signal after applying the filters based on the arrival time is shown in figure C.2.

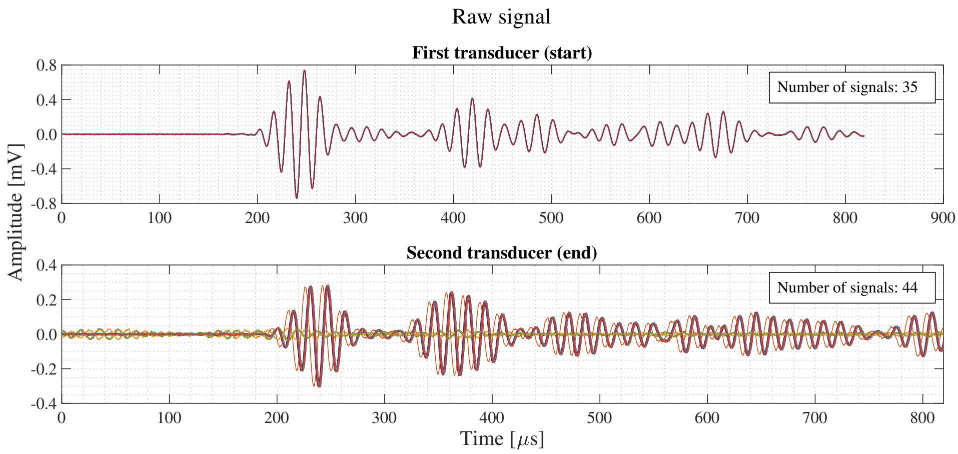

Figure C.1: The raw signal corresponding to a diagnostic waveform with properties $\theta_i = 0°$ and $\omega_j = 60$ kHz. The top graph represents the signal measured by the first transducer, and the lower graph represents the signal measured by the second transducer.

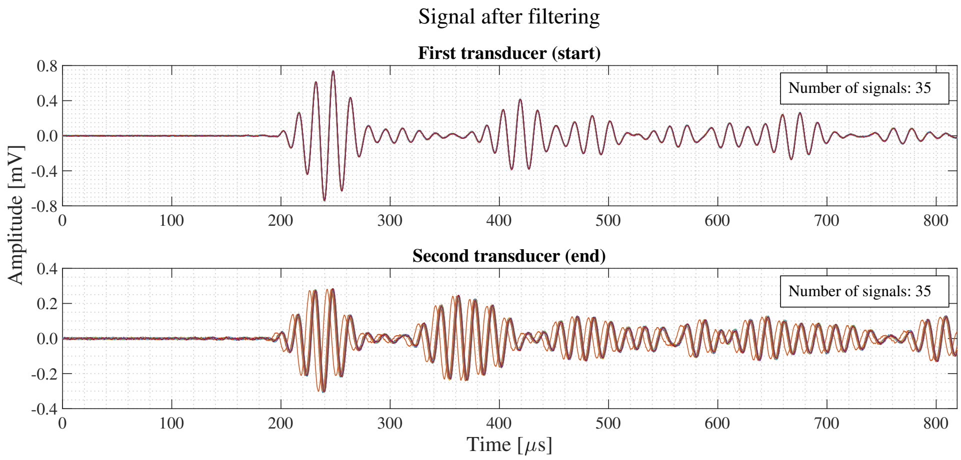

Figure C.2: The signals after filtering based on the arrival time. The signal corresponds to a diagnostic waveform with properties $\theta_i = 0°$ and $\omega_j = 60$ kHz. The top graph represents the signal measured by the first transducer, and the lower graph represents the signal measured by the second transducer.

D

Experimental velocities

In this Appendix, the signals of four replaced S_0 wave velocities are given. The procedure applied for the reliability assessment on the signals is described in Section 6.2. Windowed and normalized signals, including wave envelopes, are presented for the unreliable wave signals. In addition, the signal of their symmetric counterparts, which are used to calculate the corrected wave velocities, is presented.

Unreliable wave signal: ω_c = 50 kHz $\theta_i = 60°$

The poor wave signal is given in figure D.1. The signal of its symmetric counterpart, which is used to calculate the corrected wave velocity, is given in figure D.2.

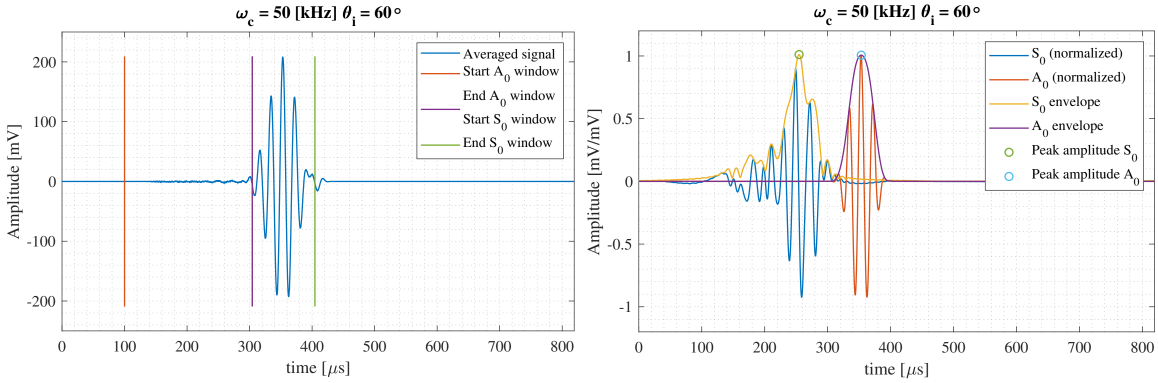

(a) Windowed signal

(b) Normalized signal including envelope

Figure D.1: The windowed (a) and normalized (b) signals of the 50 [kHz] diagnostic wave propagating in the 60° direction. The signals are recorded by the second transducer. In (b) the envelope and the maximum peak amplitude of the envelope are included.

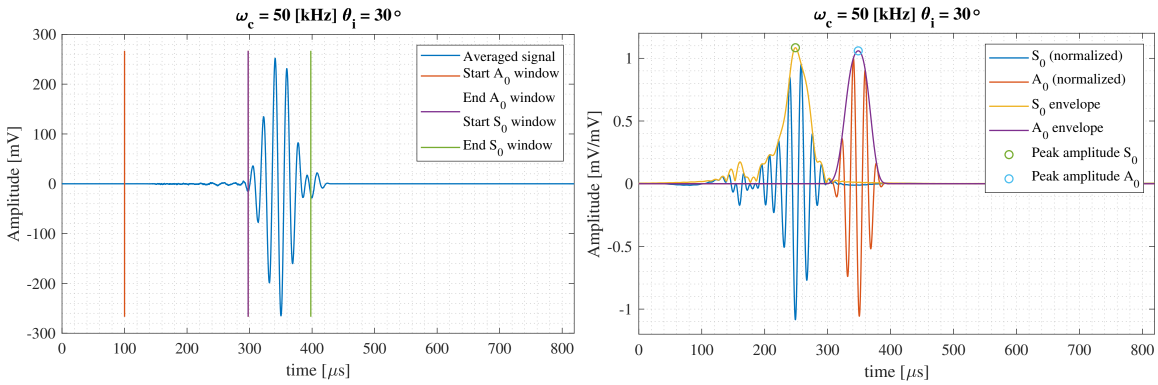

(a) Windowed signal

(b) Normalized signal including envelope

Figure D.2: The windowed (a) and normalized (b) signals of the 50 [kHz] diagnostic wave propagating in the 30° direction. The signals are recorded by the second transducer. In (b) the envelope and the maximum peak amplitude of the envelope are included.

Unreliable wave signal: $\omega_c = 50$ kHz $\theta_i = 90°$

The poor wave signal is given in figure D.3. The signal of its symmetric counterpart, which is used to calculate the corrected wave velocity, is given in figure D.4.

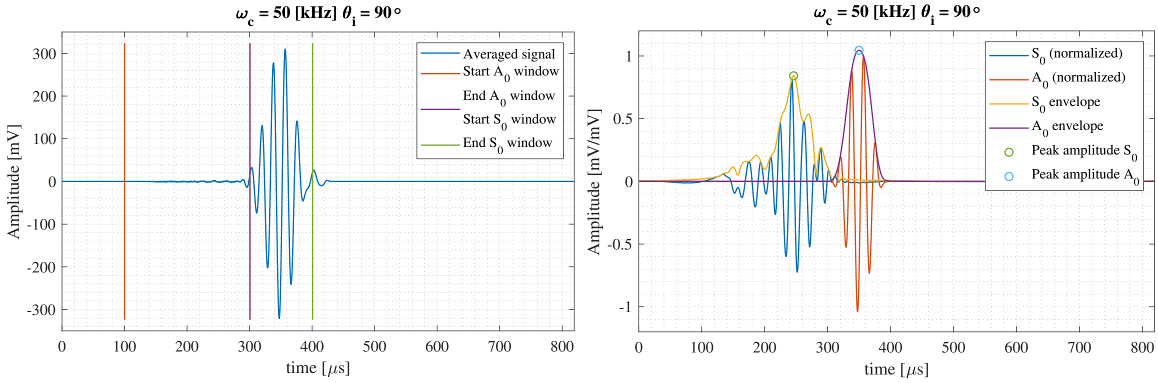

(a) Windowed signal **(b)** Normalized signal including envelope

Figure D.3: The windowed (a) and normalized (b) signals of the 50 [kHz] diagnostic wave propagating in the 90° direction. The signals are recorded by the second transducer. In (b) the envelope and the maximum peak amplitude of the envelope are included.

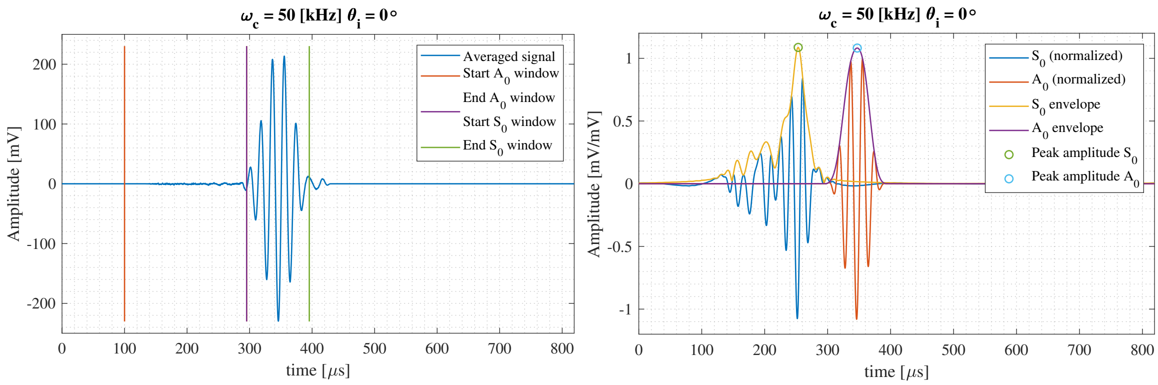

(a) Windowed signal **(b)** Normalized signal including envelope

Figure D.4: The windowed (a) and normalized (b) signals of the 50 [kHz] diagnostic wave propagating in the 0° direction. The signals are recorded by the second transducer. In (b) the envelope and the maximum peak amplitude of the envelope are included.

Unreliable wave signal: ω_c = 70 kHz $\theta_i = 60°$

The poor wave signal is given in figure D.5. The signal of its symmetric counterpart, which is used to calculate the corrected wave velocity, is given in figure D.6.

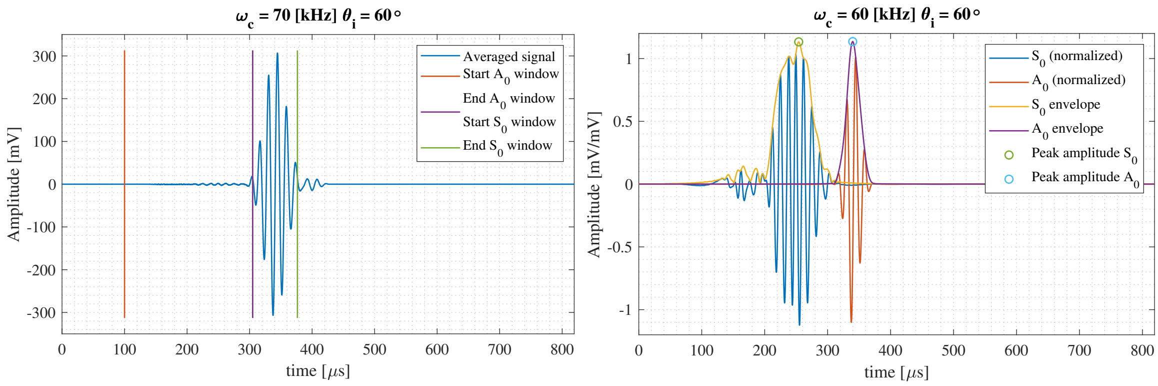

(a) Windowed signal

(b) Normalized signal including envelope

Figure D.5: The windowed (a) and normalized (b) signals of the 70 [kHz] diagnostic wave propagating in the 60° direction. The signals are recorded by the second transducer. In (b) the envelope and the maximum peak amplitude of the envelope are included.

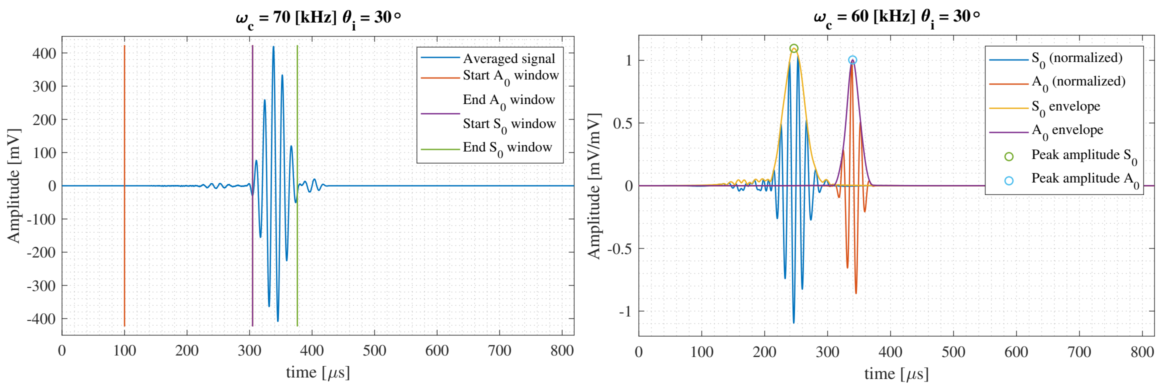

(a) Windowed signal

(b) Normalized signal including envelope

Figure D.6: The windowed (a) and normalized (b) signals of the 70 [kHz] diagnostic wave propagating in the 30° direction. The signals are recorded by the second transducer. In (b) the envelope and the maximum peak amplitude of the envelope are included.

Unreliable wave: ω_c = 70 kHz $\theta_i = 90°$

The poor wave signal is given in figure D.7. The signal of its symmetric counterpart, which is used to calculate the corrected wave velocity, is given in figure D.8.

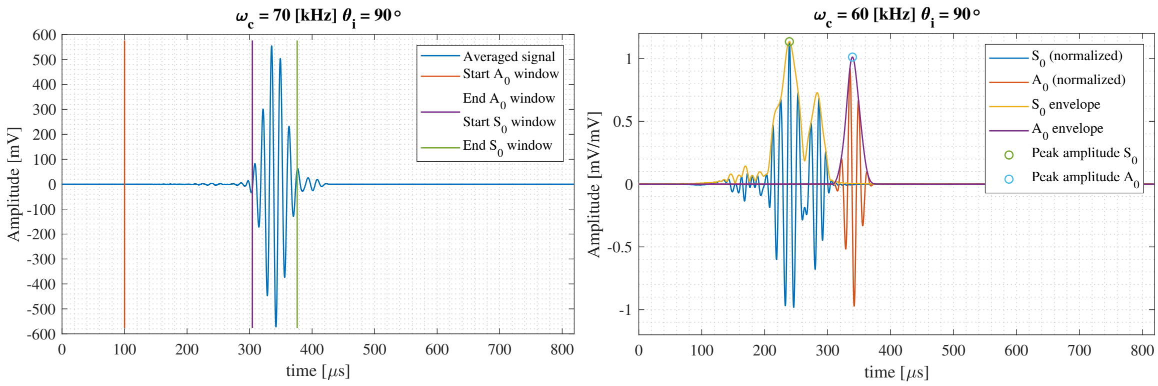

(a) Windowed signal **(b)** Normalized signal including envelope

Figure D.7: The windowed (a) and normalized (b) signals of the 70 [kHz] diagnostic wave propagating in the 90° direction. The signals are recorded by the second transducer. In (b) the envelope and the maximum peak amplitude of the envelope are included.

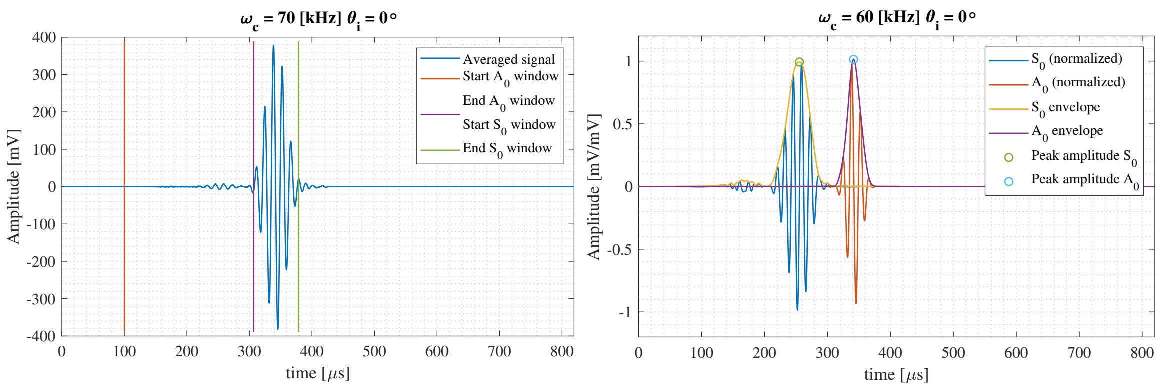

(a) Windowed signal **(b)** Normalized signal including envelope

Figure D.8: The windowed (a) and normalized (b) signals of the 70 [kHz] diagnostic wave propagating in the 0° direction. The signals are recorded by the second transducer. In (b) the envelope and the maximum peak amplitude of the envelope are included.